HELIUM, NEON, AND ARGON DIFFRACTION AND SCATTERING FROM A (3 x 5) R-35° W(110) CARBIDE SURFACE CHARACTERIZED BY LEED AND AUGER

By

PHILIP STEVEN BUSH

Bachelor of Science

The College of Emporia

Emporia, Kansas

1970

Submitted to the Faculty of the Graduate College
of the Oklahoma State University
in partial fulfillment of the requirements
for the Degree of
DOCTOR OF PHILOSOPHY
December, 1977

HELIUM, NEON, AND ARGON DIFFRACTION AND SCATTERING FROM A (3 x 5) R-35° W(110) CARBIDE SURFACE CHARACTERIZED BY LEED AND AUGER

Thesis Approved:

Leonel M. Raff
Thesis Adviser

J Paul Dewbre

Larry E. Halliburton

Neil Purdie

Norman N Durham
Dean of the Graduate College

ACKNOWLEDGMENTS

I am deeply indebted to Dr. Lionel M. Raff whose advice, patience, and support were essential throughout this work.

Heinz Hall and his staff in the Physics and Chemistry Machine Shop merit thanks for the uniformly excellent fabrications they supplied and for the design assistance they provided.

I thank Ben Simpson and the Dowell Division of Dow Chemical Company for donating their time and expertise in providing the scanning electron micrographs of the tungsten surfaces.

Very special thanks are due Tony Moldovan and the Chemistry Department at the University of Pittsburgh for the low energy electron diffraction and the Auger studies of the sample used in this work. Much of the value of these atomic scattering results is a direct result of knowing the surface conditions from which they occurred. I thank Tony for this major contribution to the work.

I thank those people who provided the background upon which this effort is based, particularly Dr. Max Pickerill, who developed my interest in chemistry, and my parents, who provided the basics.

This study was made possible by financial support from Oklahoma State University through National Science Foundation grant CHE75-18967. Appreciation is also expressed to the Oklahoma State University Chemistry Department for financial support in the form of an assistantship.

Finally, I wish to thank my wife, Jeanette, for her many contributions to this work. Her patience and support when the problems of the work overflowed into the home is certainly appreciated. Without her encouragement, the effort necessary would have been much greater and the experience far less satisfying.

TABLE OF CONTENTS

LIST OF TABLES

LIST OF FIGURES

CHAPTER I

INTRODUCTION

Atomic and molecular processes occurring at gas-solid interfaces are of prime importance in a variety of scientific and technical fields. For example, discussions of such processes are generally included in introductions to subjects such as adsorption and condensation, catalysis and oxidation, sputtering and radiation damage, rarefied gas dynamics, electron and ion emission, friction and wear, vacuum technology, and space simulation. Each of these macroscopicly observed processes is a direct consequence of individual gas-surface collisions. The science of gas-solid interactions is, however, far less advanced than that pertaining to the bulk gas and solid phases. This is to be expected since even for the most nearly ideal case the interpretation and/or prediction of interface phenomena requires a high level of understanding of the fundamental interactions in the individual phases, the modification of these bulk interactions in the top few layers of atoms that form the solid surface, and the gas-surface attractive and repulsive forces.

The initial interaction process between a gas and a solid surface involves a collision, the consequences being that the incident particle either sticks to the surface or bounces back into the gas phase, with or without loss or transformation of energy, and with or without having participated in a chemical reaction. The determination of sticking is a matter of the time resolution of the experiment.

The controlling parameters for any scattering experiment are: the approach trajectories, the particle-particle interaction potential, and the internal energy distribution of the collision partners. For the gas-solid collision the initial approach trajectory reduces to the gas trajectory, but the geometrical surface structure and surface contamination as well as the internal energy distribution of the solid can be complex and lead to a complex interaction. Long-range lattice periodicity offers the only simplifying feature, and deviations from lattice perfection in an actual experiment make interpretations more difficult.

The earliest studies of gas-surface interactions followed the development of the kinetic theory of gases. Kundt and Warburg[1] examined the effect of gas viscosity on the damping of a vibrating disk, thereby verifying Maxwell's[2] prediction that the viscosity is independent of gas density. Kennard[3] noted that this general conclusion follows from the conditions that the mean free path is small compared to the dimensions of the apparatus but not so small as to be comparable with molecular dimensions. Maxwell[4] explained this phenomenon by assuming partial accommodation at the surface. He suggested that a slip would result if gas particles striking the surface give to it a fraction of their tangential momentum. Thus, on the basis of kinetic theory, there is predicted to be a discontinuity in the viscous force at or near the surface. It was a further triumph for the kinecti jump when Smoluchowski,[5] in 1898, verified the existence of a temperature jump near the surface by determining the heat transfer between a glass surface and hydrogen gas. He also showed that, as kinetic theory would

lead one to expect, the jump distance is inversely proportional to the pressure and so directly proportional to the mean free path.

In developing a theory of the phenomenon, Smoluchowski[6] introduced a constant to represent the extent to which interchange of energy takes place when a molecule of gas strikes a surface. Knudsen[7] defined a slightly different constant which he named the accommodation coefficient (hereafter abbreviated as AC in text and α in equations). For any particular gas-solid interaction system, several different AC's may be defined, and each of these refers to a particular property of the incident and reemitted gas beams. The usual definition of AC is as follows: let $\overline{Q}_g$ and $\overline{Q}_r$ be respectively the average values per gas atom of the some scalar property, Q, of the gas in the incident and reemitted gas beams; let $\overline{Q}_s$ be the value $\overline{Q}_r$ would have if the gas were reemitted as a thermal (Maxwellian) beam at the temperature of the solid surface. The relevant AC, denoted by α_q, is defined by

$$\alpha_q = \frac{\overline{Q}_r - \overline{Q}_g}{\overline{Q}_s - \overline{Q}_g} \quad . \tag{1}$$

An important special case of equation (1) was first introduced by Blodgett and Langmuir.[8] If Q is the kinetic energy, E, of the gas, for monatomic gases the resulting AC,

$$\alpha_e = \frac{E_r - E_g}{E_s - E_g} \tag{2}$$

is called the "thermal AC". For those systems where the distribution of particle velocities is Maxwellian, the mean translational energy

per particle is

$$E = 2kT \tag{3}$$

where k is Boltzmann's constant. By combining equations (2) and (3) in accordance with the pertinent energies, the AC may be written as:

$$\alpha_e = \frac{T_r - T_g}{T_s - T_g} \quad . \tag{4}$$

It should be noted that the AC as defined by equations (1), (2), or (4) is not a well-behaved function, that is, the AC expression becomes indeterminate at Q_s equal to Q_g. Raff[9] and coworkers removed this undesirable feature by redefining the energy accommodation coefficient (EAC) as:

$$\alpha_E = \frac{E_g - E_r}{E_g} \tag{5}$$

Alternatively it may be more convenient to use the modified form of Jackson[10]

$$\alpha = \lim_{\Delta T \to 0} \frac{T_r - T_g}{\Delta T} \tag{6}$$

where $\Delta T = T_s - T_g$.

In general, the experimental techniques for determining AC's are classified as either conductivity cell measurements or molecular beam techniques. The conductivity apparatus typically consists of a small diameter wire suspended along the axis of a pyrex tube which has a diameter much larger than that of the wire. In studies on clean

surfaces, the wire is some engineering metal with a high melting point, such as tungsten, so that it may be flashed clean at very high temperature. The pyrex cylinder is immersed in a constant-temperature bath and the tube filled with the gas of interest. The filament is kept at an elevated temperature by a precisely measured current. A net transfer of heat from the filament to the wall is established as a result of molecular collisions and radiation. The inside walls of the cylinder are usually covered with an effective getter such as mischmetal which traps contaminant gases assuring a relatively clean surface for the duration of the experiment. The current required to maintain the filament at temperature, T_s, and the voltage drop across the filament determine the power input, W_f, to the filament. This power is dissipated by gas conduction to the wall, end loss to the filament supports, and radiative losses. The extent to which these latter two contribute to W_f may be found from a duplicate experiment in a good vacuum. This power is denoted W_v. Thus, the steady state heat conduction per second per unit area of the filament, W_g, is merely the difference divided by the apparent area of the filament:

$$W_g = \frac{W_f - W_v}{2\pi r l} \quad . \tag{7}$$

The limiting expectation value for the power conducted away by the gas, W_{KT}, is calculated from kinetic theory and the AC defined as the ratio of W_g to W_{KT}.

In the low pressure method the gas during a run is maintained below approximately 0.06 mm Hg to assure free molecular flow. Under this condition the assumption that the gas incident temperature, T_g, is

equivalent to the cell wall temperature and consequently the bath temperature is an excellent one. Even if the accommodation coefficient between the gas and the pyrex wall is very low, the gas particles are fully accommodated to the wall temperature between successive collisions with the wire. The low pressure method is without serious objection if applied under free molecular conditions[11,12] and has been primarily the method used to obtain reliable values of the AC of gases on clean surfaces.[13,14] In contrast the methods applicable to transition and temperature jump conditions are subject to certain reservations.[12,15-19] An experimental comparison of the low pressure method and the Smoluchowski-Kennard[20] temperature jump method was reported by Thomas and Golike.[15] Measurements of the AC of several gases on a platinum surface were made under as nearly identical conditions as were consistent with experimental procedures. The two methods yielded AC values in very good agreement considering the difficulty in realizing "nearly identical conditions" for a contaminated platinum surface. Wachman[12] later analyzed the same data using his mean free path approach and showed that the resulting values of the AC were in equally good agreement with the low pressure values.

More recently Lees and Liu[16] and others have reexamined and advanced the kinetic theory of heat conduction to cover the range from free molecular to continuum behavior. Springer and co-workers[21,22] have made extensive heat conduction measurements over the transition and temperature jump range under conditions where the goal was "to attempt to maintain constant surface conditions throughout the experiment". The measured AC of helium on tungsten was 0.2831 as compared to a clean tungsten value of about 0.17,[14,23,24] so it may be definitely stated

that the filament was not clean. Both this study and the Thomas-Golike[15] study are open to the same criticism; if the surface condition varies during the experiment, invalid conclusions may be reached regarding the degree of agreement between the various formulations. To eliminate this criticism, Roach and Thomas[24] measured the AC of helium and neon on clean tungsten for a range of pressures from about 0.01 to 100 torr. The data from appropriate pressure and ΔT ranges were then analyzed by the Smoluchowski-Kennard temperature jump method,[20] the Langmuir-Washman mean free path method,[12] and the moment method of Lees and Liu[16] as modified by Hurlburt.[11] In general the values are in such good agreement that they conclude that any of these formulations may be utilized to determine the AC for He or Ne on clean tungsten. The cleanliness of the filament was checked by the low pressure method at the beginning and end of each run. Roach and Thomas[24] caution, however, that their preliminary measurements using the heavier inert gases indicate more prominent differences between the methods under certain experimental conditions.

Some general trends in the Ac's as determined by conductivity cell measurements on clean surfaces are:

1) The AC's decrease as the ratio M_g/M_s decreases, where M_g and M_s are the masses of the gaseous and surface particles respectively.[25]

2) The AC's are larger for larger heats of adsorption if the mass ratio is approximately constant.[26]

3) The AC's approach unity at low T_g, go through a minimum, and increase at large T_g.[26]

4) The AC for ^{4}He is greater than for ^{3}He, but the values approach each other as T_g decreases.[25]

5) The AC's increase appreciably when adsorbed particles are present on the surface.[13,27,28]

6) The ΔT dependence of the AC increases as the mass ratio increases and as the temperature decreases.[14]

The AC's as measured by conductivity cell techniques have made a significant contribution to our understanding of gas-surface interaction. Following the first measurements of Roberts[29] on a relatively clean surface, a number of theoretical studies[10,30-33] were undertaken. The study by Devonshire[32] employing a quantum model with a Morse potential is the most general. Adjustment of the Morse potential parameters gave results that seem to agree with experiment, but Goodman[34] noted that the simplifying assumptions of single phonon transitions and independent linear oscillators are not realistic. Also Devonshire's numerical results are not in good agreement with the more recent AC values of Thomas and co-workers.

Classical theories of energy accommodation based on one-dimensional lattice models have been considered by Caberera,[35] Zwanzig,[36] Goodman,[37] Leonas,[38] and McCarroll and Ehrlich.[39] To obtain a more realistic model of the solid, Goodman proceeded to a three-dimensional lattice. Similar models have been employed by Trilling[40] and by Chambers and Kinzer.[41] By a trial-and-error procedure Goodman[34] determined the values of the Morse parameters, a and D, which cause his theoretical predictions of AC to agree with experimental results. Although excellent quantitative agreement with the data of Thomas[23] was obtained for reasonable values of a and D, this result may be

misleading since the theory is based on several questionable assumptions. The limitations of the theory in connection with the good results suggests that the AC by itself does not test the detailed features of the model.

The AC's as measured by any of the conductivity cell methods have some inherent shortcomings as a test for theoretical models. Experiments are restricted to gas temperatures less than the filament temperature while theories usually assume surface temperatures less than gas temperatures and often, for simplicity, assume surface temperatures equal to absolute zero. In order to make accurate measurements on a clean surface, a getter must be employed and this limits the studies to gases which do not interact strongly with either the getter or the surface. Probably the largest single limitation is that the AC is a bulk property, an average over all possible trajectories and velocities; thus, it cannot yield detailed knowledge of individual encounters.

These objections are, for the most part, removed in a molecular beam experiment. The majority of molecular beam studies of gas-surface interactions have been concerned with determining flux distributions of scattered particles. A few have surmounted the experimental difficulties involved in determining the energy difference between incident and scattered beams.

The spatial distribution of the gaseous particles relative to the surface are usually defined by the relationships depicted in Figure 1. The particles at temperature T_g strike the surface at temperature T_s at spherical polar angles of θ_i and ϕ_i, where the z-axis is chosen to coincide with the surface normal. The in-plane angle of

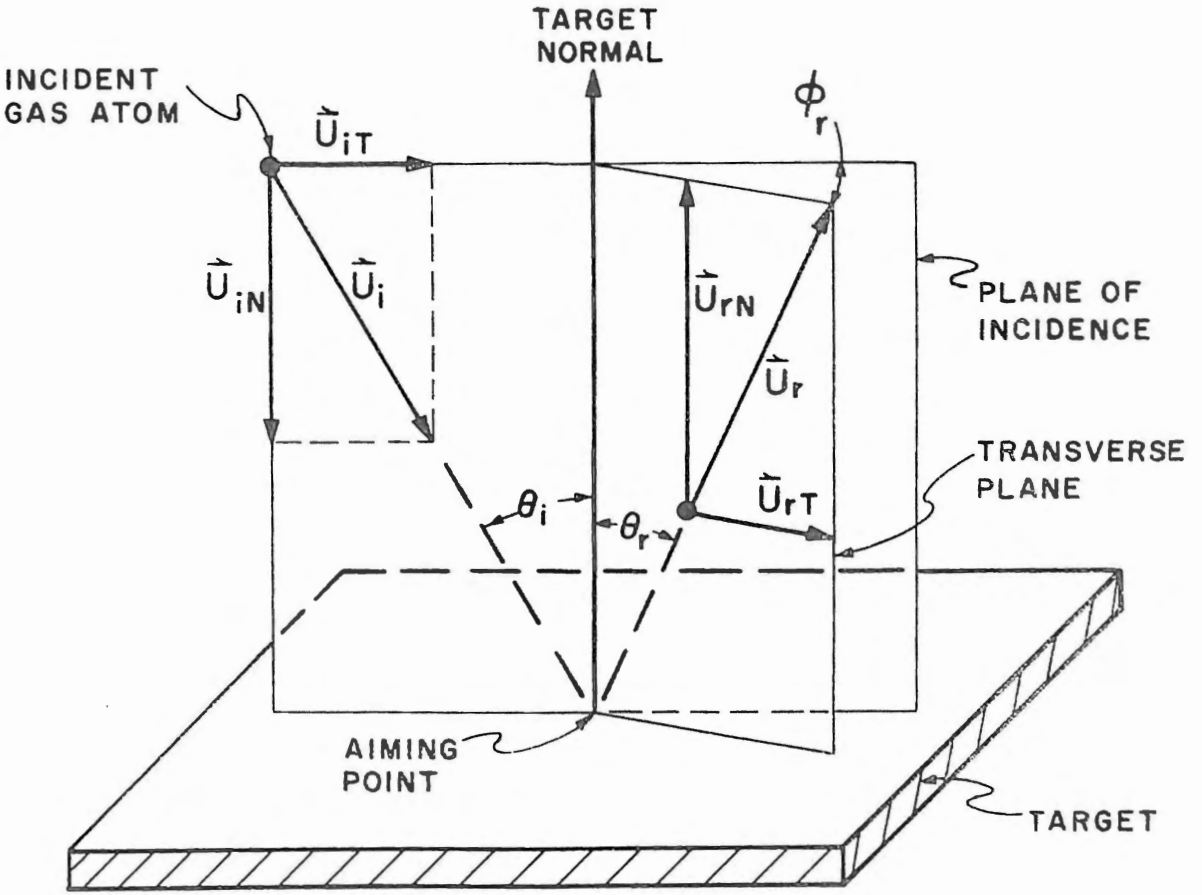

Figure 1. Three-Dimensional Gas-Solid Interaction Model

incidence θ_i and the surface normal define a plane into which the majority of the beam flux is scattered with in-plane angle of reflection θ_r. A small flux is found out-of-plane with an angle of reflection ϕ_r. Often θ_r is not the same as the specular angle θ_s and in some cases the maximum flux may be coincident with the target normal (cosine scattering).

The earliest molecular beam experiments using light particles and surfaces with strongly periodic potentials provided verification of the De Broglie wave-particle hypothesis for particles as heavy as small atoms or molecules. The reflection experiments of Knauer and Stern[42] employing helium and molecular hydrogen incident on sodium and potassium chloride crystals, as well as the experiments of Ellett, Olson and Zahl[43] using cadmium atoms reflected from sodium chloride, indicate the presence of a surface diffraction phenomenon. Estermann and Stern[44] found that the reflection of helium and molecular hydrogen from crystals of lithium fluoride conclusively show the cross-grating nature of the diffraction. Further experiments by Stern et al.[45] used the diffraction of a thermal helium beam from a lithium fluoride crystal to obtain a velocity-selected helium beam which was then scattered from a second lithium fluoride crystal. Good agreement was obtained with results using mechanical velocity selection and, in this manner, the De Broglie formula was confirmed to within one percent.

Recent experimental results for the helium plus lithium fluoride system have been obtained by Crews,[46] Fisher et al.[47] Williams,[48] and O'Keefe et al.[49] Bayh and Pflung[50] studied the adsorption of water on lithium fluoride by means of polarized light reflection (ellipsometry). These authors found that at least four monolayers of water are present

on a lithium fluoride surface obtained from a single crystal freshly cleaved in vacuum. The last water monolayer can be removed only by heating the crystal to temperatures exceeding 700°C. Thus, the experimental results obtained so far have been from surfaces contaminated by adsorbed water. Beder,[51] using the first order diffraction peak spacing measured by Estermann, and Stern, calculates a value of 2.85 A° for the period of the lithium fluoride surface. Such excellent agreement with the value of 2.84 A°, the like ion spacing of lithium fluoride, indicates that the first few monolayers of water are adsorbed in an ordered manner which retains the underlying crystal spacing and periodicity. The heavier rare gases scattered from lithium fluoride give the rainbow scattering predicted by the classical dynamical theories[52,53] with a hint of diffraction only for neon. Scattering from weakly periodic structures like the low index faces of metals shows neither diffraction[54,55,56] of helium nor rainbow scattering for any of the heavier rare gases.

It was not until recently that diffraction from any surface other than alkali halides was reported. Weinberg and Merrill[57,58] demonstrated that helium and deuterium give diffractive scattering from a tungsten carbide (3 x 5) overlayer on a tungsten (110) surface. Tendulkar and Stickney[59] reported diffraction from a tungsten (112) surface when the helium incident beam is oriented perpendicular to the atomic rows giving the strongest periodicity, but no diffraction in the principal scattering plane when the incident beam is parallel to these rows. The (112) surface consists of ridges of tungsten atoms extending in the $(11\bar{1})$ direction, spaced 4.47 A° apart, and projecting 2.37 A° above the intervening valleys.[60]

The problems of surface preparation have received considerable attention. Roberts[61] reviews several methods of generating clean surfaces in ultrahigh vacuum. Saltsburg et al.[55,62-71] have had success with the technique of continuously depositing a fresh target surface on a cleaned mica substrate during the scattering measurement. Target material is evaporated from a crucible located away from the gas beam path and condensed at a rate roughly ten times at which background contaminants would be expected to arrive at the target. Moreover, careful control of substrate temperature can insure epitaxial growth of a single crystal face. Belous and Wayman (72) studied the effect of continuous vapor deposition on the temperature of a thin film at the deposition surface and it appears that the actual temperature of the surface may have been two to four hundred degrees higher than Saltsburg et al. reported. The restriction to particular substrate temperatures, in order to insure epitaxial growth, severely limits the applicability of this technique.

The effect of surface condition is easily seen in the work of Smith and Saltsburg.[62] Scattering distributions for a 300 K helium beam incident at 50° upon a gold target at 560 K were measured with and without the continuous deposition of target material. The distribution is narrow and specularly directed during the time the surface is kept clean with the continuous deposition of gold. After deposition is stopped for about 30 minutes, a steady-state condition is reached in which the distribution is broad and less specularly directed.

In this same study, Smith and Saltsburg demonstrate the difference between spatial scattering from a polycrystalline target and from an

epitaxial single-crystal film. A single crystal, (111) face, results from deposition onto a substrate at 560 K, while a polycrystalline surface results from maintaining the substrate at 300 K during deposition. The single crystal yields a distribution which is narrow and specularly directed, while the polycrystalline film shows an almost cosine scattering distribution.

Sau and Merrill[73] recently compared scattering of the rare gases from a Ag (111) face prepared from a bulk single crystal and from two epitaxially grown Ag (111) surface. They found that single-crystal scattering is narrower than the scattering from either epitaxial surface. The broader spatial distributions and the large backscattered diffuse components lead them to conclude that the epitaxial surfaces are significantly rougher than the single-crystal surface (one possibility being fairly large grain boundaries). In the case of helium scattering, comparisons are made among all three surfaces. It is worth noting that the differences between the scattering from the two epitaxial surfaces are greater than the differences between the single crystal and one of the epitaxial surfaces. It is unfortunate that the comparisons between epitaxial and single-crystal surfaces using neon, argon, and xenon were made only with the epitaxial surface which showed the larger discrepancies in the helium distributions.

In general, the features of scattering distributions from clean surfaces are similar. The distribution is lobate, with the maximum varying from above the specular angle to below the specular angle, depending upon whether the gas temperature, T_g, is less than or greater than the surface temperature, T_s. This effect becomes more prominent as θ_i increases. The out-of-plane scattering is symmetric

about the principal plane and the out-of-plane distribution is much narrower than the in-plane distribution. Both in-plane and out-of-plane scattering distributions broaden as the ratio of gas atom mass to surface atom mass increases. As this ratio increases, the angular position of maximum spatial scattering is a much more sensitive function of the relative gas and surface temperatures.

Spatial scattering lobe full-width at half maximum (FWHM) increases with the ratio T_s/T_g and with decreasing θ_i. These observations are consistent with the prediction that gas-solid interactions are greatest for direct impact between colliding particles and that the majority of the momentum transfer occurs along the surface normal and relatively little along the tangent. Transfer of the normal component of momentum also accounts for the trends seen in the deviation of spatial scattering lobes from the specular angle.

In-plane spatial scattering intensity (ϕ_r = o) decreases towards a minimum as θ_i increases, while out-of-plane scattering intensity approaches a minimum as θ_i increases. For those cases where the average speed of the scattered particles has been determined, the maximum speeds are at the peak of the spatial distribution for low T_s/T_g and at the surface normal at high T_s/T_g.[74,75]

The scattering of the rare gases from clean metallic single-crystal surfaces can be described qualitatively in terms of the increased energy transfer per collision due to a combination of mass effects and an increasing attractive potential as the atom mass increases. As one proceeds through the series helium to xenon on a given metal the scattered trajectory distribution becomes broader and has its maximum intensity displaced from the specular angle towards the

normal, but complete cosine scattering is not usually observed. Weinberg and Merrill[56,58] have indicated, on phenomenological grounds, that thermal energy scattering may be separated into three regimes, denoted by the terms quasielastic, inelastic, and trapping-dominated.

In general terms, the quasielastic regime is characterized by scattering distributions which are symmetric about the specular angle and whose general behavior is dominated by the thermal roughening of the surface (Debye-Waller effect). In the inelastic regime significant energy transfer occurs which increases as the interaction time increases relative to the characteristic vibrational frequency of the solid, with the latter quantity being characterized by the Debye temperature. Debye-Waller effects may also be observed in this regime, although evidence indicates that dynamic attenuation, due to structural effects, may be more important.[73] Trapping-dominated scattering occurs when a significant percentage of the incident particles are absorbed for a relatively long period of time prior to reemission. In this trapping-dominated regime, the nature of the scattering process for the untrapped portion of the beam may be largely obscured by the contribution to the scattering distribution due to the desorption of trapped particles. Thus, as the surface temperature is increased, a decrease in scattering intensity due to thermal roughening is usually more than offset by an increase due to less trapping. Empirically, Weinberg and Merrill have determined a correlation between these three scattering regimes and the ratio of the effective potential energy well depth, D, to the gas atom kinetic energy, kT_g. Values of D/kT_g less than approximately 0.3 characterize

quasielastic scattering and trapping dominates at values greater than about 3.0.[56,73]

Velocity information in addition to the spatial scattering distribution is required for the assessment of energy and momentum exchange during gas-surface collisions. Momentum accommodation normal to a surface is typically determined with a sensitive torsion balance apparatus. A target mounted on one arm of the balance interrupts a beam of test gas inside a vacuum chamber. The other arm of the balance is operated as a null force device where the nulling force required to keep the target stationary in the beam is directly related to the transfer of momentum at the surface. The difficulties of cleaning the target surface while it is mounted on a fragile balance arm have usually limited these studies to contaminated surfaces.[76-78]

Prior to the late 1950's, molecular beam measurements of energy transfer were fairly limited. The lack of an efficient and universal detector of neutral atoms and molecules prompted the development of many ingenious but limited ones. Ramsey[79] provides a very complete review of this early work so only a few of the more characteristic studies will be mentioned here. Ellett, Olson and Zahl[43] studied the scattering of a Maxwellian beam of Cd atoms from a NaCl crystal. Using a slotted-disk velocity selector (SDVS), they determined that Cd atoms scattered at the specular angle were nearly monoenergetic with a velocity 60% to 100% greater than the mean velocity of the incident beam, and that the velocity at the specular angle increased as the angle of incidence increased. Qualitatively similar results were obtained for Zn.[80] Using the Stern-Gerlach effect, Ellett and Cohen[81] examined the velocity distribution of K scattered by MgO. They

observed cosine scattering with a Maxwellian velocity distribution characteristic of the surface temperature (±5%) in the scattered beam, indicating nearly complete accommodation. Marcus and McFee,[83] using an SDVS, investigated K scattered from Cu, W, MgO, and LiF. Maxwellian distributions characteristic of the surface temperature were observed in scattered beams from all except LiF. For K on LiF a considerable deviation from a Maxwellian distribution was observed and attributed to incomplete accommodation at the surface. Unfortunately, these measurements did not include the determination of the spatial scattering.

These early studies were limited by the available detectors to strongly interacting systems. The first detector was a cold surface upon which the beam material condensed. This technique requires beam material which is easily condensable and is then stable long enough to determine the quantity condensed. The surface ionization detector which was developed by Taylor[83] from the observations of Langmuir[84] had the very distinct advantage of being able to discriminate between beam material and residual gas. Those gases which may be detected by either of the two aforementioned techniques usually exhibit strong interactions with target materials. Thus, the spatial distributions are characteristic of fully accommodated particles and consequently insensitive to parameters of the interaction potential.

The hot cathode ionization tube is the most universal detector currently in use, but two characteristics have limited its applicability until recently. The ionization efficiency is very low and consequently the signal is small. Secondly, it is a universal detector, so the contribution of background gases to the observed

signal is large. A miniature mass spectrometer is often used in conjunction with ionizing tubes to distinguish between the test gas and background gases.

Modern signal-processing techniques have greatly increased the sensitivity of molecular beam experiments. The minimum useful signal, or sensitivity, is a function of the signal-to-noise ratio and is greatly increased by modulating the desired beam of particles and then employing a lock-in amplifier or a multichannel analyzer to reduce the background noise.

In a modulated molecular beam experiment, the output from an ionization type detector will be of the form

$$S(t) = y(t) + z(t) , \tag{8}$$

where $y(t)$ is the repetitive signal to be measured and $z(t)$ represents the random noise, whose average is zero, always present in the electron current. Noise is produced because at low pressures the number of molecules passing through the ionizer is statistically variable and because the number of ions produced from a given density of molecules in the ionizer is variable. Under normal experimental conditions, $y(t) \ll z(t)$, and therefore averaging operations must be applied.

A second advantage to modulating the molecular beam is the possibility of measuring the time required for each packet to travel the distance between chopper and detector. A light beam interrupted at the same time as the molecular beam provides a reference signal. The phase shift between reference and detector signal is then related to the average speed of the particles across the experimental chamber. Accurate phase shift measurements are possible using this technique if

the signal-to-noise ratio is large. The more usual case for reflected beams is to have noise equal to or greater than the signal. This requires long time constants for signal averaging and determination of the phase angle becomes difficult and tedious, with a precision in the order of a few degrees (~5°). When this uncertainty is propagated through to the final calculation of an AC, the result is an uncertainty of ±200% for helium on a platinum surface at 970 K.[85] While this is a "worst case" example, it does illustrate limitations of the technique.

The application of the lock-in amplifier to molecular beam research began with the work of Fite and Brackman.[86] Yamamoto and Stickney[87] derived expressions for the amplitude and phase angle of lock-in signals as functions of the parameters of the experimental system. Smith et al.[88-90] used this technique in determining the spatial distributions of hydrogen and argon scattered from a polycrystalline nickel surface. Using the phase shift circuitry of the lock-in amplifier, Smith found that the accommodation coefficient is a function of the scattering angle. He estimated an accommodation coefficient of 0.8 near the normal and 0.3 near the specular angle when scattering room temperature argon, incident at 60° from nickel at 450°C.

The preferred instrument for making time-of-flight (TOF) measurements has in recent years been the multichannel analyzer (MCA). Accurate MCA molecular beam experiments began with the work of Moran in 1967. With this instrument the period of the beam signal is divided into several segments. The input voltage during each time segment is then applied sequentially to separate integrating circuits (channels) by successively triggered gates. This process is repeated in a cyclic fashion for a number of periods where the number is controlled by the

time constant. In this way the random noise is reduced relative to the coherent signal to a degree which is proportional to the square root of the time constant.

The resolution of MCA-TOF measurements is sufficient for the calculation of low order moments of the velocity distribution which then give the number density, average momentum, and average energy of the particles.[91] In comparing this technique to the previously discussed conductivity cell measurements, it is seen that two of the three criticisms have been reduced. By employing a supersonic nozzle source, the distribution of incident angle (θ_i) is substantially reduced and the width of the incident velocity distribution is reduced by an amount dependent upon the Mach number achieved. The third criticism, however, that the resulting measured value is a bulk property and consequently not a very sensitive probe of the interaction, has not been reduced. This objection can only be overcome by an instrument with sufficient resolution to investigate the detailed differences between the incident and reflected velocity distributions.

It has been the intention of this study to investigate the tungsten(110) singly-crystal surface via a molecular beam apparatus which employs a slotted-disk velocity selector and a lock-in amplifier. This combination (SDVS plus lock-in) should provide the required resolution of both the incident and reflected velocity distributions. This information, in conjunction with spatial distribution measurements, was to provide a sensitive test for the results from theoretical calculations.

In addition, the carbon-contaminated W(110) surface has been examined using helium, neon, and argon beams with very narrow

half-widths as the probes. It has been suggested that bimodal rainbow scattering should not be observed from the (3 x 5) R-35° W(110) carbide superstructure. The highly periodic nature of this surface should, however, be sufficient. Questions have been raised concerning the validity of the diffraction observations of Weinberg and Merrill.[58] An attempt has therefore been made to further elucidate the degree of periodicity required to produce rainbow phenomena.

CHAPTER II

THE EXPERIMENTAL APPARATUS

Introduction

The experimental difficulties associated with measurements of atomic and/or molecular scattering from solid surfaces have been fairly well established. Chiefly, they are: (a) the generation of a collimated beam of particles with a well-defined energy; (b) the use of a vacuum system with sufficient pumping speed that there is no long-term deterioration of surface conditions as the experiment proceeds; (c) the detection of a signal from the gas beam where the useful signal power is in a range equal to, or several orders of magnitude less than, the signal arising from the residual gas in the scattering chamber; and (d) the production of a well-defined surface so that meaningful interpretation of the results can be made. This chapter describes the apparatus used to remove or reduce these obstacles.

The experimental apparatus described herein allows the study of the energy transfer across the interface between a large number of possible gas-solid combinations. A supersonic nozzle source generates the beam of gas. Although proper functioning of the nozzle does not require it, the gases studied in this work were restricted to the inert gases helium, neon, and argon. This facilitates the data interpretation since these gases lack rotational and vibrational degrees of freedom and are relatively easy to detect.

The gas stream is chopped prior to impinging on the surface. The spatial and velocity dispersion on the particles are determined with a slotted disk velocity selector (SDVS) and an ordinary ionization gauge detector. The beam signal passes through shielded cable to a preamplifier located outside the vacuum chamber and a lock-in amplifier effects the final signal processing prior to the recording of the experiment. The target may be rotated about the two axes that are mutually perpendicular to the gas beam at its intersection with the target face or lifted completely out of the beam path so that the same detection system can be used to characterize the incident beam. The SDVS and detector revolve about the aiming point on the target surface.

The final assembly, shown in simplified horizontal section in Figure 2, consists of the following major components: (1) the main scattering chamber maintained at a very low pressure; (2) the buffer chamber containing the beam chopper and shutter; (3) the beam source chamber containing the quartz nozzle and the first skimmer; (4) the target holder supporting the surface; (5) the speed selector and detector mounted together on a large turntable. Figure 3 is a photograph of the apparatus.

The Vacuum System

The Main Scattering Chamber

The main chamber is fabricated from cold-rolled stainless steel secured with a continuous bead tungsten-inert gas (TIB) weld throughout. The internal dimensions of the main chamber are: diameter 66.0 cm.,

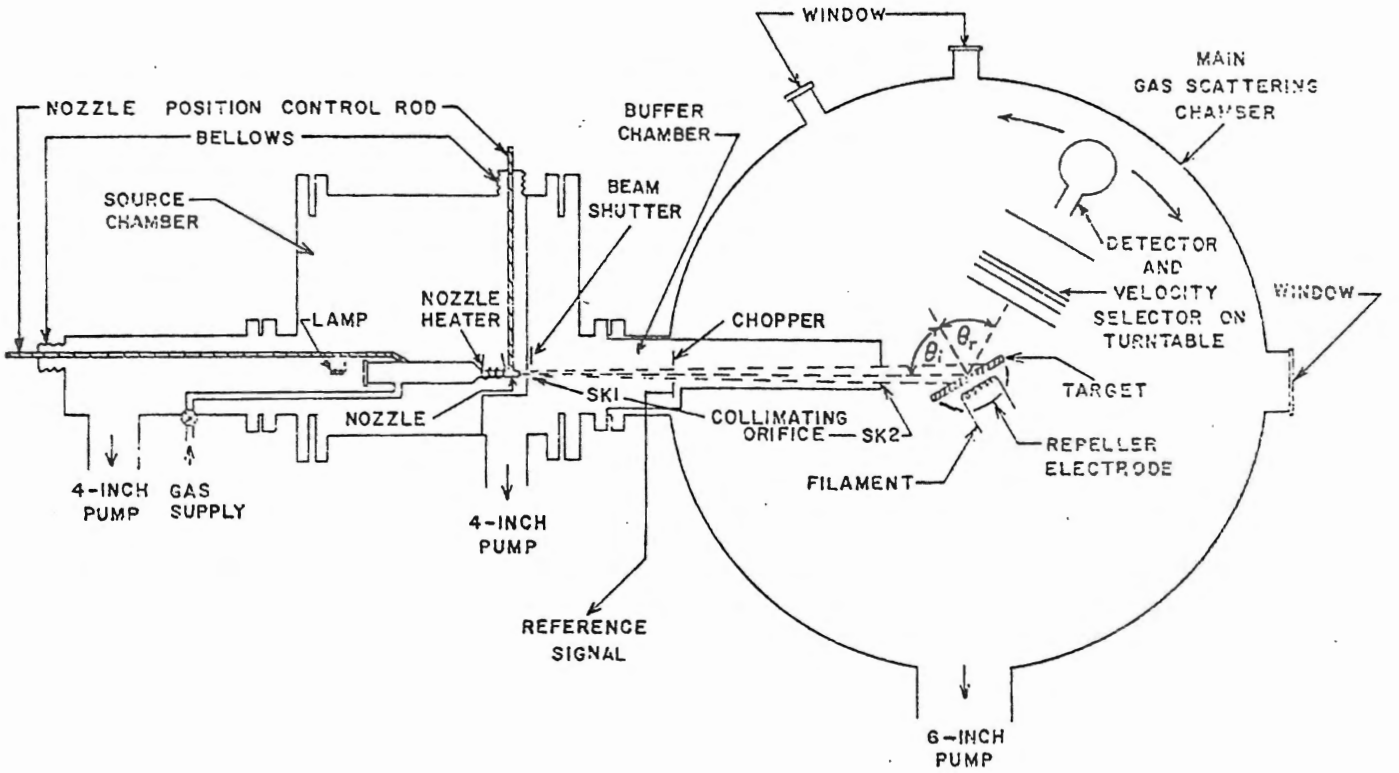

Figure 2. Experimental Apparatus Schematic

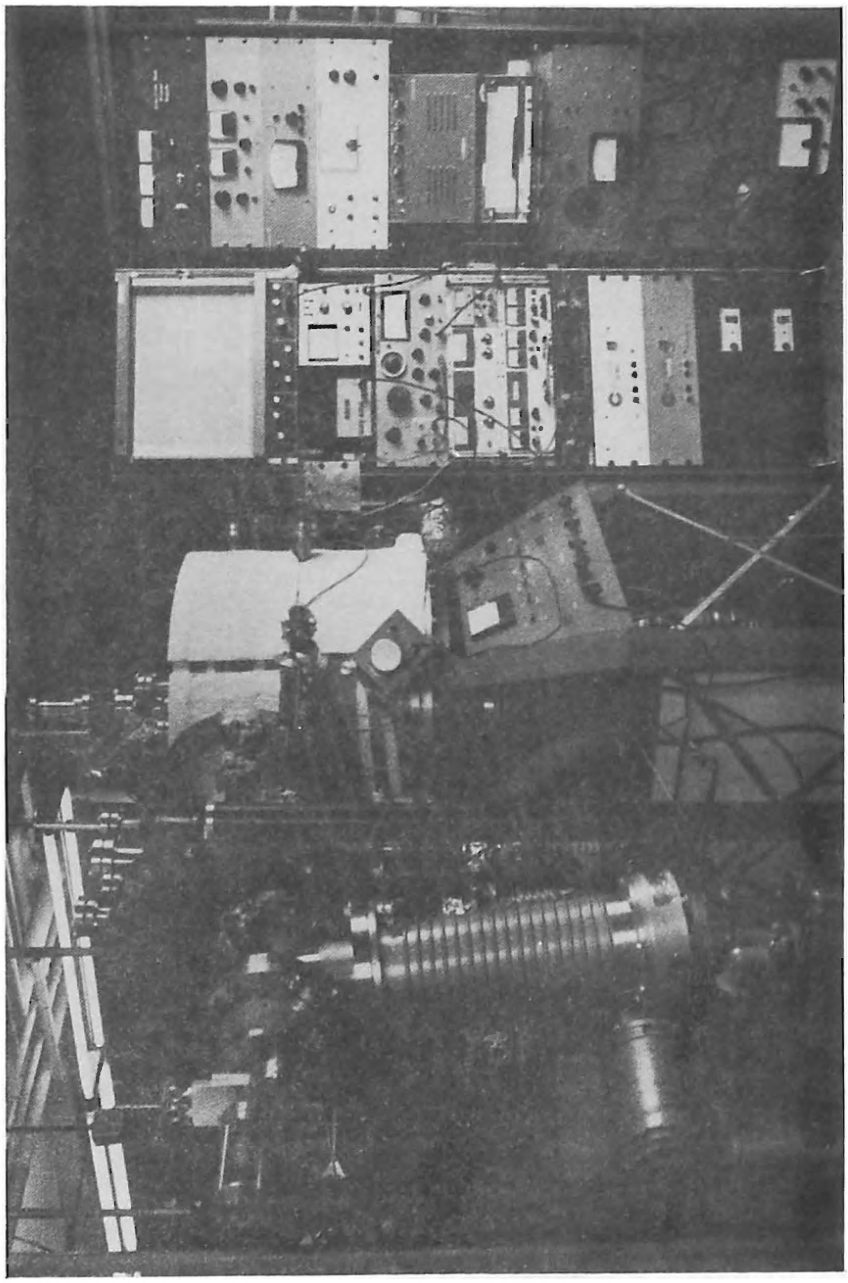

Figure 3. Photograph of the Apparatus

height 49.2 cm., total volume about 175 liters. The wall of the envelope is 0.953 cm. thick, and the lid has a thickness of 1.91 cm. The chamber bolts to a baseplate that is 2.10 cm. thick, and an aluminum gasket 3.81×10^{-3} cm. thick seals the 77 cm. flange. The gasket and flange design is from the basic work of Batzer and Ryan.[93] A more complete description of the flange details and their construction techniques are given by Coryell.[94] The main chamber has eighteen small ports at strategic locations. There are two large side flanges. One contains a six-inch pyrex window and directly across the chamber the eight-inch flange mounts the buffer and nozzle chambers. Several electrical feedthroughs were required to penetrate the vacuum wall. Bolt circles with the Batzer flange detail were welded to excellent 7-pin feedthrough blanks purchased from the General Electric Company. Two rotary-motion feedthroughs were purchased from Cooke Vacuum Products, Inc. and they worked well for light loads. The one used to rotate the relatively heavy detector table was found to have a bothersome amount of backlash. These feedthroughs were of the radially bent bellows design containing no o-ring seals. This design is preferable for ultrahigh vacuum systems that are baked out. The buffer and nozzle chambers were constructed similarly with all-metal vacuum seals, although the less stringent vacuum requirements did not require it.

The detector assembly is mounted on a heavy turntable 0.953 cm. thick and 62.9 cm. in diameter. Underneath the turntable is a ring of stainless steel into which is machined a deep groove. On the base plate of the main scattering chamber is an identical groove. Loose ball bearings, 1.27 cm. in diameter, fit into the mated grooves and

constitute a simple thrust bearing on which the table pivots. To reduce friction the balls are dusted with niobium diselenide, a dry lubricant that is an electrical conductor.

Position of the detector turntable is controlled from outside the main scattering chamber with a bellows type rotary motion feedthrough. A gear track runs around the periphery of the turntable and meshes with a pinion gear turned by the feedthrough. There is a $16\frac{2}{3}$ to 1 gear reduction in the rack and pinion. The detector can be located with a precision of $\pm 0.1^{o}$ of arc.

The Pumping System

The main scattering chamber is evacuated with one six-inch-diameter oil diffusion pump which pumps successively through an ambient water-cooled baffle and a liquid nitrogen baffle. The total pumping speed of the stack is approximately 900 liters per second. Three automatic liquid nitrogen controls were purchased from Cooke Vacuum Products Inc. but since the best reliability that could be achieved was approximately eighty percent, the trap was filled manually three times per day.

The buffer and nozzle chamber are each differentially pumped by one four-inch oil diffusion pump. This provided sufficient pumping speed for the buffer chamber but much less than desirable for the nozzle chamber. An eight- or ten-inch pump is suggested for future experiments. Each of the diffusion pumps utilize polyphenol ether oil as their working fluid.

Foreline connections are Dresser Vacuum TF-100 Twinflange Unions attached with four-inch nominal diameter pipe. In each

foreline there is a flexible bellows coupling to dampen mechanical vibrations.

Two moderately large mechanical pumps working in series provide the forepumping. The pump closer to the diffusion pumps is a Roots-type blower with a top pumping speed of 85 cubic feet per minute at a pressure of 100 microns. This pump is backed with a compound dual-vane mechanical pump which has a pumping speed of 20 cubic feet per minute. Together the two pumps give a very high throughput over a wide pressure range. Pumpdown for the entire system from atmospheric pressure to 5×10^{-4} mm. Hg is less than 15 minutes.

The vacuum system itself is bakeable to 400°C, but the presence of electronic devices within the main chamber placed an upper limit of 150°C on the temperature to which the system could be subjected. Bakeout is achieved by wrapping electrical heating tapes and ceramic felt insulation around the exterior of the apparatus. After bakeout, a pressure of 3×10^{-10} mm. Hg is typically achieved within the main scattering chamber.

Pressure within the vacuum envelope is measured with a General Electrid "nude" ionization gauge. Thermocouple gauges monitor the foreline vacuum.

The Beam Source

Research-grade gases from high-pressure cylinders pass from the supply cylinder via a manifold to a Purox high-purity cylinder regulator. This manifold is bakeable and may be evacuated to 10^{-5} mm. Hg between uses to minimize cross contamination between the various gases. The gas then goes in turn through an in-line filter with a pore

size of 7 microns, a Varian variable leak valve, and into the beam source chamber (nozzle chamber). A mechanical manometer with a range of 0 to 1500 mm. Hg and a compensation scale to correct for differences between ambient pressure and 760 mm. Hg monitors the gas pressure delivered to the nozzle.

The nozzle source design, shown at 40 X magnification in Figure 4, follows that of Moran[91] with some modifications. The beam source is a Laval-type nozzle with both a converging and a diverging section. Each nozzle was made by cutting a 3 mm. o.d. quartz tube with a 1 mm. thick wall to the desired length, then fire polishing one end until a channel of the desired diameter was achieved. Final diameters were measured with a machinist's microscope which had a double micrometer stage precise to one ten-thousandth of an inch. For the present study, a nozzle with a somewhat oval channel and an average diameter of 0.188 mm. was chosen.

The nozzle is held with a Cajon Ultra-torr tube fitting. The nozzle holder, shown in Figure 5, slides in a track of kinematic design that insures only one degree of freedom. The lateral position of the nozzle (the direction parallel to the beam) is then precisely controlled from outside the nozzle chamber through a linear feedthrough in the vacuum wall. One turn of the feedthrough handle displaces the nozzle by 0.127 cm. Two mutually perpendicular sidewise motions of the nozzle tip are provided by linear feedthroughs which rock the nozzle a small amount in its O-ring seat. These two degrees of freedom are sufficient to scan the nozzle tip back and forth across the first collimating skimmer. Any attempt to move the tip excessively in either of these latter two directions will, of course, snap the nozzle

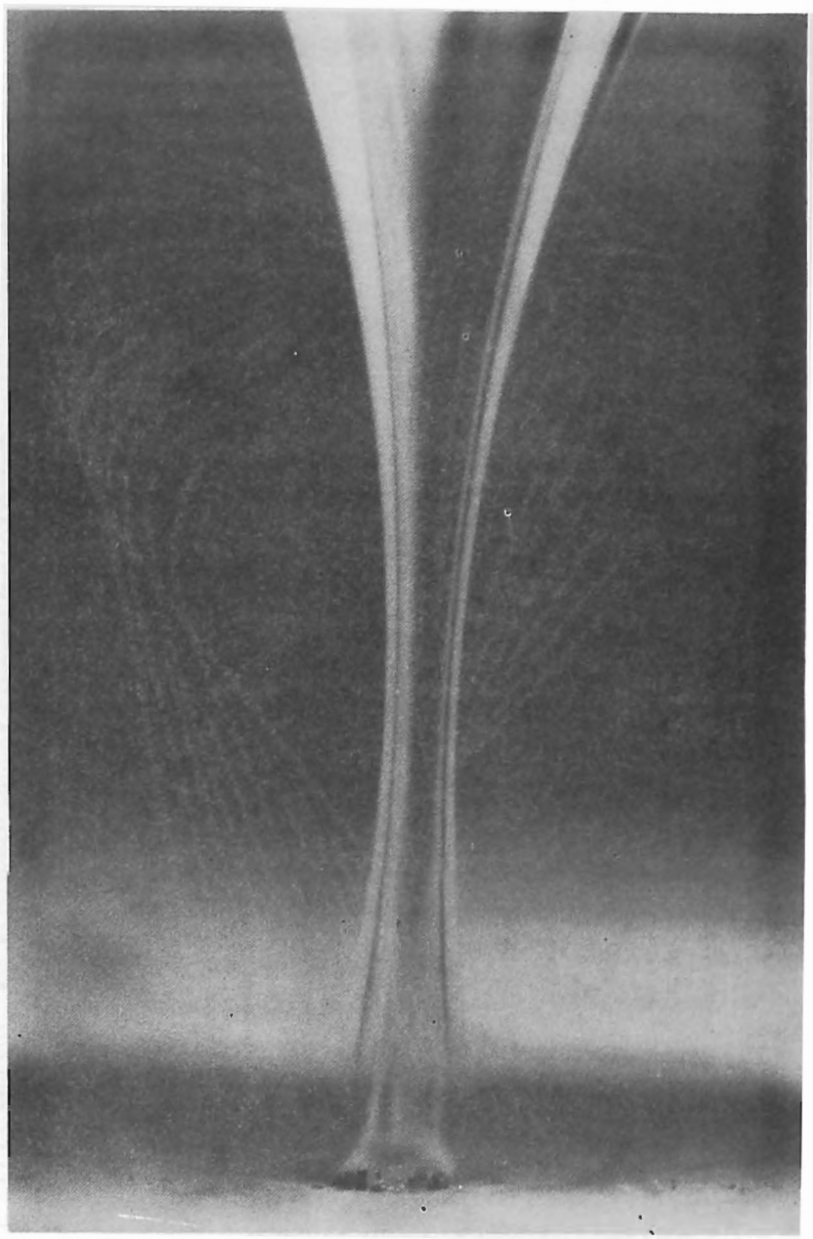

Figure 4. Laval Type Nozzle Channel Used in This Work at a Magnification of 40 X

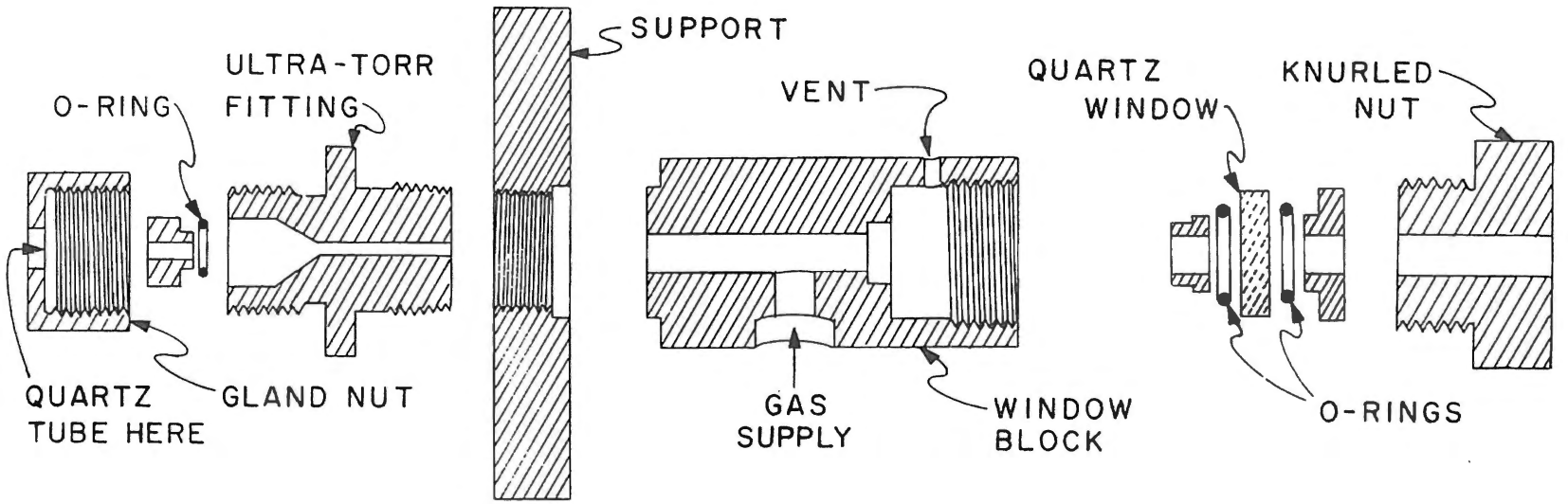

Figure 5. Nozzle Holder

stem. Wrapped about the nozzle tip is a coil of nichrome wire which has two major functions. First, an electric current may be passed through the resistance wire thereby heating the nozzle between ambient temperature and a maximum temperature of 900°C thus increasing the average energy of the beam particles. Enclosing the nichrome coil is a ceramic sleeve which is rigidly attached with epoxy cement to two small-diameter aluminum rods. The rods are in turn fastened to the two-linear motion feedthroughs providing the two independent sidewise motions that scan the nozzle tip past the collimating orifice. The wire coil provides a sliding contact transmitting the two motions from the ceramic sleeve to the nozzle tip without play while leaving the nozzle free to slide axially through the coil and increase or decrease the distance between the nozzle tip and the beam-collimating orifice.

The beam source chamber and buffer chamber have a single open area in common: the first collimating orifice (SK1). The diameter of this circular orifice is 0.343 mm. The orifice was drilled in a circular coupon 0.30 mm. thick and bolted to the bulkhead separating the two chambers. The diameter of SK1 is chosen such that for a given nozzle diameter, nozzle-to-SK1 distance, and maximum gas supply pressure, the pressure within the buffer chamber is low enough to insure a minimum attenuation of the beam through collisions with background gases. This requires that the vacuum within the buffer chamber be maintained at or below the 10^{-6} torr range.

Good vacuum technique dictates that the beam chopper be located in its own differentially pumped buffer chamber. This procedure assures that a minimum of background gas from the source chamber will pass through the chopper and enter the main scattering chamber. Such

a gas "leak" would have a number of undesirable effects on the experiment: 1) it would tend to impart a coherent fluctuation of the background gas pressure within the large chamber; 2) particles present in the leak could pass through the skimmer at a highly divergent angle, go through the chopper, and enter the detector acceptance port obliquely without ever approaching the surface; 3) gases such as carbon monoxide, hydrogen, water, and others resulting from the operation of the source chamber diffusion pump would be present within the beam. These impurity gases would be converted to signal by the universal detector and interpreted by the experiment as resulting from an inert gas atom collision with the target surface. The worst effect of the presence of impurity atoms within the beam is that they would constitute a major contaminating source presented to the surface. The relatively high accommodation coefficients of such gases would allow the formation of multiple atomic layers within the time span of a single experiment. In order to minimize such effects the chopper is located approximately half way between the entrance skimmer (SK1) and the exit skimmer (SK2) of the buffer chamber. This positioning of the chopper also insures that those particles deflected from the beam path are pumped by the buffer chamber's diffusion pump and do not contribute to the background pressure within the main scattering chamber. This reduces the pumping speed requirements of the main chamber by 25 or 30 percent. An electronic solenoid within the buffer chamber and immediately adjacent to SK1 on the downstream side places a metal flag over SK1 when activated. This shuts off the beam completely and allows the base line signal to be quickly established during an experimental run.

Coherence in the background gas in an experiment incorporating a nozzle source is not the problem that it is for experiments employing an effusive source. There is a large difference in flux between these two basic types of source. Nozzle sources of the design employed herein will typically have a flux of approximately 4×10^{17} particles per steradian per second.[95] Effusive sources within a similar orifice diameter have a flux of up to 1×10^{16} particles per steradian per second.

The beam is chopped at a frequency of 25 cycles per second (Hz) using a two-vane mechanical chopper supplied by American Time Products (Bulova). This chopper is analogous to that employed in an "Accutron" wristwatch. Two rectangular vanes roughly 8 mm. by 15 mm. are attached to the end of the tines of a tuning fork. Between the tines is a relatively large electromagnet which has two windings, a drive coil and a pick-up coil. The slightest vibration of the apparatus starts the tines oscillating at their fundamental frequency. This creates a signal in the pick-up coil which is amplified and returned to the drive coil in proper phase to make the tines vibrate with the desired amplitude. The amplifier is a simple solid-state device located outside the vacuum system. The pick-up signal is available at the amplifier for use as a reference to the lock-in. Obviously, the greater the number of beam particles present per chopped packet (i.e., the longer the time the chopper vane is out of the beam path relative to the time it interupts the beam) the larger will be the signal at the detector output. This is true only as long as the beam "off" time is longer than the decay time constant of the detector and its electronics. A somewhat arbitrary choice of having one vane

interrupting the beam on the basis of two-thirds "on" time to one-third "off" time per cycle was made. No attempt to optimize this particular parameter of the apparatus was made during these experiments.

The chopper used in this work is significantly different from the ones used in time-of-flight (TOF) determinations. For the TOF experiment it is essential to employ a chopper which has a sharp and well defined shutter function with a rise time very short relative to the mean speed of the particles being chopped. Velocity dispersion will cause each chopped packet of gas particles to lose some of its coherence during the flight from the chopper to the detector. Typically, the chopper will have a triangular shutter function with a total open time (base) of 125 microseconds. The time between the shutter function maximum and detected pulse maximum is a measure of the mean speed of the packet. The degree to which the detected pulse has spread relative to the shutter function is used to estimate the velocity dispersion within the packet. These requirements preclude the use of a tuning fork type chopper with its sinusoidal motion and trapezoidal shutter function for TOF measurements. Such stringent wave form requirements are not encountered when a slotted-disk velocity selector is used for velocity determinations.

The tuning fork modulator suffers one fault. When it is subjected to appreciable changes in temperature, the physical properties and consequently the fundamental frequency of the fork change sufficiently that the amplifier/drive will no longer maintain oscillations with an amplitude adequate to interrupt the beam. At that point the beam is no longer modulated, and the lock-in amplifier loses its reference. The two sources of large temperature

gradients commonly found in the vicinity of molecular beam choppers are the target surface and the first beam-defining orifice. Normal-sized targets at a surface temperature of 2500 K will radiate approximately 150 watts of power. Under ultrahigh-vacuum conditions, very little of that power need be absorbed by the tuning fork to appreciably increase its temperature. A heat sink is provided if SK1 and the bulkhead about SK1 are cryogenically cooled. Liquid nitrogen and/or liquid helium may be used as cryogenic fluids to increase the pumping speed within the nozzle chamber. Locating the chopper at the center of a buffer chamber sufficiently isolates it from these temperature gradients. An alternative solution would be to power the tuning fork with a variable frequency oscillator and adjust the lock-in amplifier filter accordingly. In this way, modulator performance could be optimized in the likely event that the fundamental frequency drifts.

The second beam-defining orifice (SK2) is shown in Figure 6 with dimensions. SK2 limits the beam width to the desired value as the beam enters the main scattering chamber. Table I summarizes the distances between the major experimental components.

The Crystal, Its Support and Manipulator

Seven slices of one tungsten single-crystal rod were purchased from Aremco Products Inc. The rod was manufactured via a triple zone-refining technique which produced single crystals specified as 99.9996% pure. After orienting the rod to within 1° of the (110) crystallographic plane, each specimen was sliced from the rod by a spark erosion process and one side mechanically polished. The

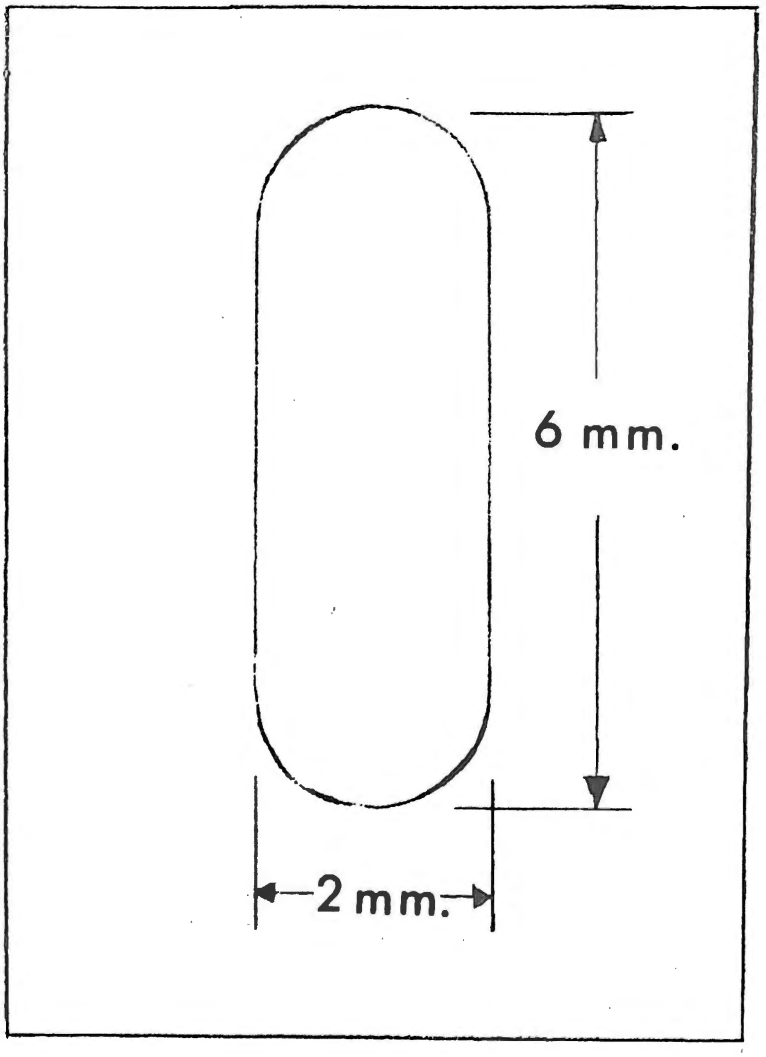

Figure 6. Dimensions of SK2

TABLE I

DISTANCES BETWEEN MAJOR EXPERIMENTAL COMPONENTS

Nozzle to SK1 7.6 mm. (adjustable)
SK1 to chopper = 25.4 cm.
SK1 to SK2 = 43.8 cm.
SK2 to target = 12.7 cm.
Target to first disk of SDVS = 10.8 cm.
Target to flux detector entrance = 21.6 cm.

crystallographic orientation was checked in this laboratory by Laue back-reflection x-ray diffraction and found to be 0.1° off the (110) plane. Each sample consisted of a circular disk with a diameter of 8 mm. and 3 mm. thick. Targets were treated according to the method of Germer and May[98] as modified by Yamamoto and Stickney.[75] Targets were annealed at ~1300 K and a residual gas pressure of 2×10^{-8} torr, with periodic flashes to 2100 K, to remove any surface strain caused by the mechanical polishing.

The crystal manipulator and holder are pictured in Figures 7 and 8. The sample is held under a slight clamping pressure by three 1.59 mm. diameter tungsten pins positioned at 120 degree increments about the crystal side. The actual contacting tip of each pin is tapered to about half its original diameter to minimize heat conduction from the sample to the holder. Each pin rests within a cylindrical cavity drilled into a high-purity tantalum screw. The

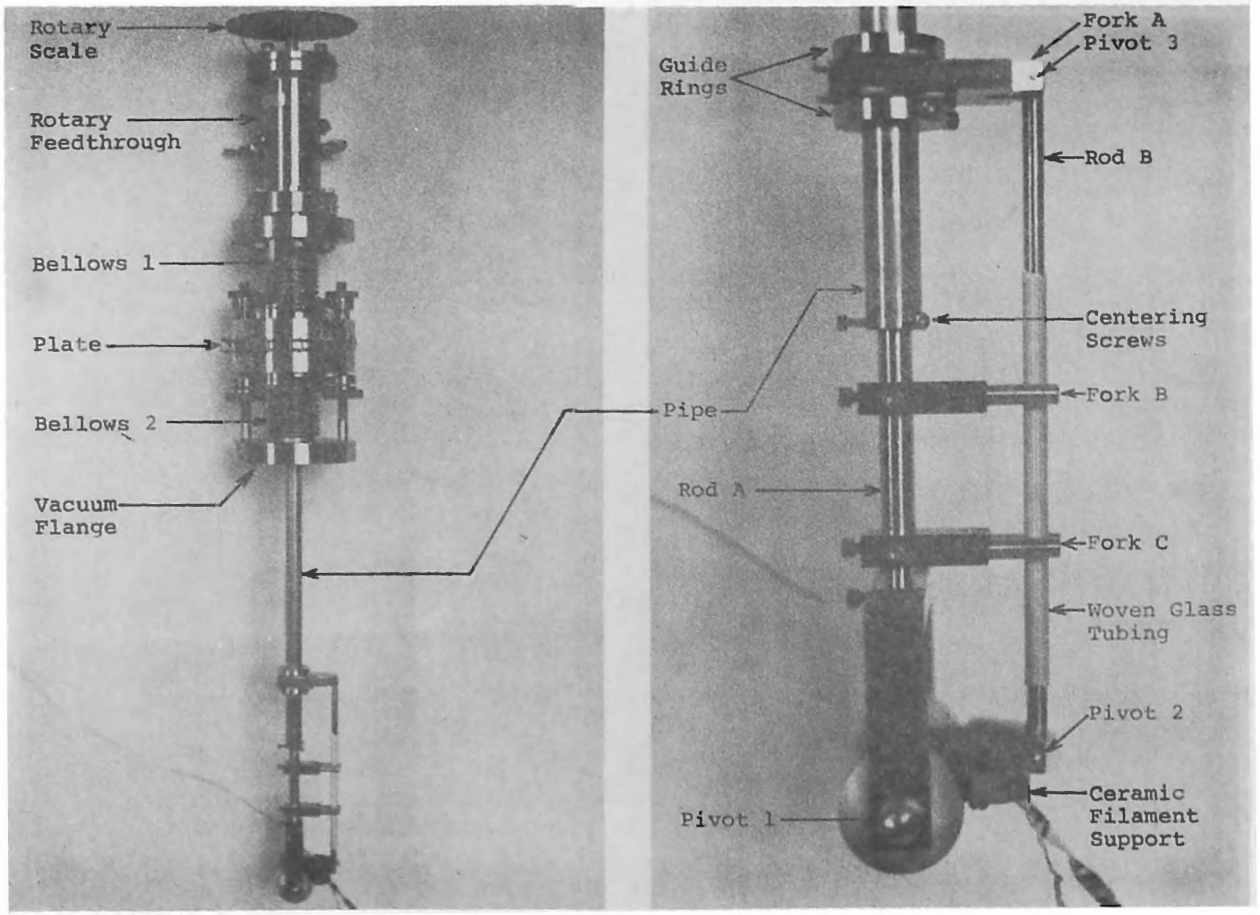

Figure 7. Crystal Manipulator

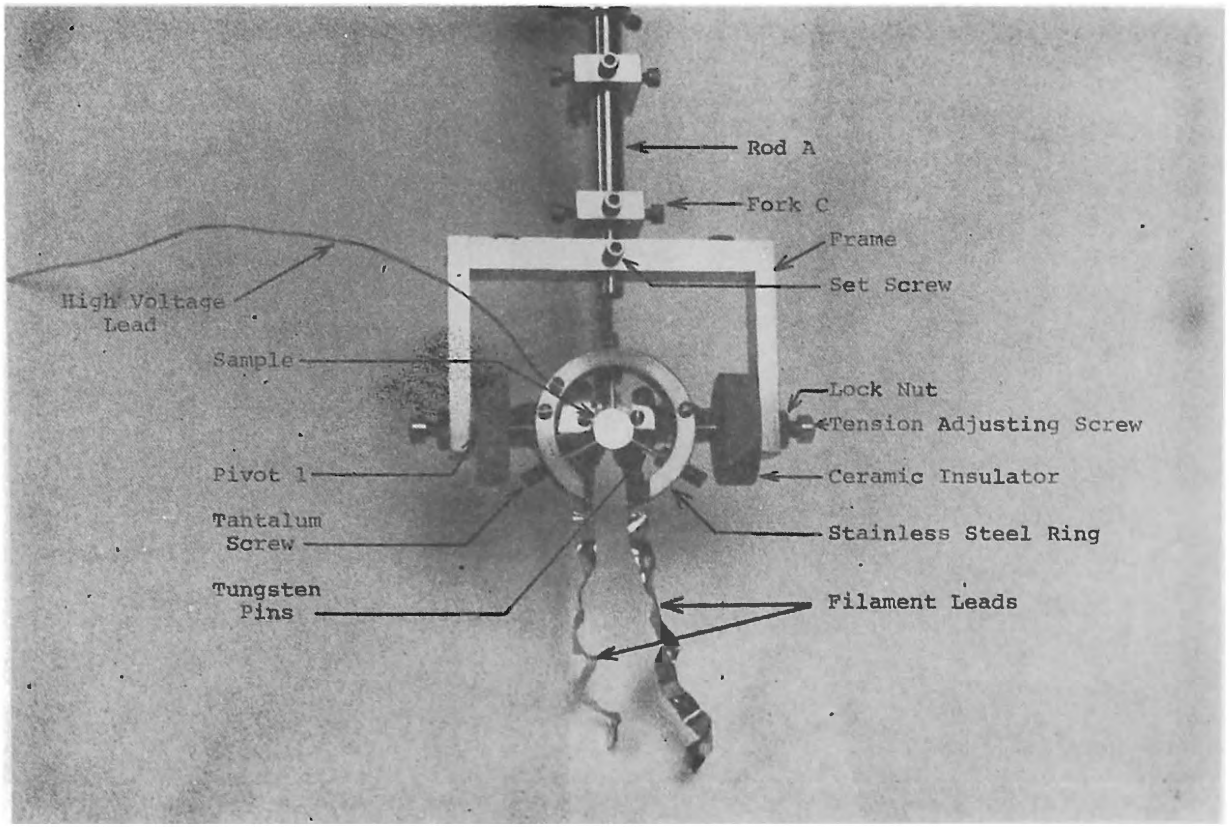

Figure 8. Sample and Sample Holder

tantalum screws are threaded through a 3.18 cm. inside diameter stainless steel ring. A small section of the ring was cut away to allow it to flex during thermal cycling of the target. A positive 1-kV accelerating potential is applied to the metal sample through the stainless ring. Two electrical insulators machined from MACOR™ machinable glass-ceramic purchased from Corning Glass Works isolate the ring gimbal from the main frame of the manipulator. The target surface is positioned 14.0 cm. from SK2, the final beam-defining orifice.

The crystal manipulator is comprised of one rotary-motion feed-through bolted to two bellows which are connected in series. This arrangement transmits one independent rotary, one independent linear, and one dependent linear motion through the vacuum envelope. Expansion of the bottom bellows, bellows number 2 of Figure 7, lifts the crystal and its support from the beam path. The incident beam may then be characterized using the same detector system used to measure the scattered particles. Without this ability no meaningful correlation can be made of data taken from day to day or even from one experiment to the next. There can certainly be no intensity comparisons of scattered distributions between different laboratories.

The target support ring and main frame form a simple gimbal with one axis of rotation which lies on a line between the two tension-adjusting screws. The axis of rotation for this gimbal passes through the aiming point on the target and lies in the horizontal plane described by the nozzle, surface, and detector. Rotation of the target about this axis established the out-of-plane angle of incidence, Φ_i, and the out-of-plane angle of reflection, Φ_r, for the gas beam.

This rotation is accomplished from outside the chamber by a compression or expansion of bellows number 1. A compression of bellows 1 moves rod A down with respect to the pipe since they are fastened to opposite ends of bellows 1. Fork A and rod B are held immovable with respect to the pipe (as far as this linear motion is concerned) by the two guide rings. An upward pull is therefore applied to the ceramic filament mount by rod B. The ceramic filament mount is bolted solidly to the crystal support ring and acts as a lever forcing the gimbal to rotate about its axis. This rotation is useful for two reasons. It allows the crystal to be carefully aligned in-plane while the apparatus is under vacuum. Secondly, for experiments where diffraction phenomena are observed, a complete interpretation requires that an entire hemisphere about the surface be examined by the detector. No out-of-plane measurements are reported here.

The target support main frame is hung by vertical rod A from the ceiling of the main scattering chamber. This rod lies along the central axis of the scattering chamber and may be turned from outside the chamber with the rotary feedthrough. Rotation of the rod established the in-plane angle of incidence, θ_i, for the gas beam. The angular resolution for the in-plane angle of incidence is 0.1°. The setting of θ_i may be monitored through two small view ports in the main scattering chamber wall. Forks B and C are clamped solidly to rod A by three set screws. As rod A rotates, these two forks constrain rod B and therefore fork A to also rotate about the pipe without applying torque to pivots 2 and 3. Woven glass braid tubing purchased from W. M. Hicks Inc. encased rod B thus allowing rod B to slide smoothly through the tines of forks B and C when the gimbal alignment

was changed. A similar technique was used for the sliding contacts between the guide rings and fork A. Woven glass tubing was slipped over a copper wire and then bent into the form of a five-pointed star. The pipe passing through the central open area of the star holds it in position. Metal-to-metal sliding parts bind when the tolerances are held close to minimize play; binding is especially bad at vacuum levels of 10^{-9} torr and below. The glass braid packing alleviates this problem for very slow sliding motions and it outgasses very little.

The targets are heated by electron bombardment on the back side. The details of the electron gun and its power supply are discussed later in this chapter. An electron beam current of 100 ma and an accelerating potential of 1 kV heats the target to 2275 K. During an experiment the surface temperature of the target is measured through a pyrex window with a Leeds and Northrup optical pyrometer certified by the National Bureau of Standards. The precision of this method is ±4 K.

Corrections were applied using a combined form of Wien's law for the radiant energy difference between two bodies when one is a black body radiator.[96] The relation between the brightness temperature, T_B, and the true temperature, T, is:

$$\frac{1}{T} - \frac{1}{T_B} = \frac{\lambda \ln E_\lambda}{C_2} \qquad (9)$$

if λ is expressed in centimeters, $C_2 = 1.438$ cm. K, temperature is in Kelvin and E_λ is the emittance or emissivity of the non-black body at temperature T. λ for the disappearing filament pyrometer used in this study is 0.665×10^{-4} cm. A constant value of $E_\lambda = 0.45$ was chosen by interpolation from the data of DeVos.[97] Neglect of the

change in E_λ with T, over the range 1100 K to 2500 K, introduces errors of +10 K at the low end and -10 K at the top. The transmission of the one-eighth inch pyrex window was measured as 91 percent at a wavelength of 0.665×10^{-4} cm. using a Cary Model 14 spectrometer. The absolute temperature measurement is, therefore, well within a limit of ±15 K over the entire range of these experiments.

It is currently not possible in this apparatus to make surface temperature measurements below the lower limit of the pyrometer, 1100 K. A tungsten-rhenium thermocouple should be incorporated to monitor the room temperature to 1100 K range. The total equipment requirements would be: an uncalibrated thermocouple (it could be calibrated against the optical pyrometer), two high-voltage feedthroughs, and a digital thermocouple readout capable of floating at the accelerating potential of the electron gun. A floating readout must either be battery powered or have an isolation transformer incorporated in the power line.

The Velocity Selector and Its Power Supply

The slotted-disk velocity selector (SDVS) is from the basic design of Hostettler and Bernstein[99] (HB) with a few modifications. For this work particles which pass through the SDVS have their direction of travel specified by the orientation of the admittance orifices of the SDVS shroud and of the detector both in-plane (θ_r) and out-of-plane (Φ_r). Thus, the SDVS is a "speed" selector rather than a "velocity" selector. However, to conform to common usage and avoid confusion, the terms velocity selector and velocity distribution will be used. Five aluminum disks 1.59 mm. thick and 16.0 cm. diameter are clamped on the shaft of a hysteresis synchronous motor. The disks have

rectangular slots 0.795 mm. wide with a radial length of 7.95 mm. Each disk is clamped in a strategic location on the rotor shaft such that is removes the undesired higher-order speed side bands from the gas beam. The disks have 280 teeth instead of the 278 used by HB.

A SDVS such as this is normally used in one of two ways in molecular beam experiments. It is used either to measure the incident velocity distribution or it is used to filter the particles and form a beam with a very narrow velocity distribution even though the source may be an effusive one and produce a Maxwellian distribution. In either case it is mounted close to the source, usually near one of the skimmers, and the alignment of the rotor axis is permanently fixed relative to the beam axis. The conversion factor which relates the angular velocity of the SDVS to the linear velocity of particles which pass the slots is very critically dependent upon this alignment. If a source producing a known distribution (such as an effusive source) is used, the alignment of the rotor axis relative to the beam axis plus the transmission of the rotor may be checked by comparing the measured distribution with the known incident velocity distribution. This is the procedure employed by HB in their original publication and they determined that their cited example was misaligned by about 8 minutes of arc.

An SDVS employed, as in this study, to measure the velocity distributions of particles scattered from a surface, has additional requirements applied to its design. Scattered particles are not traveling in a small nicely defined beam as are incident particles. It is therefore necessary to provide a cover over the disks with

baffles and passage holes to insure that any particles which enter the detector have passed through all disks of the selector.

It is useful to be able to lower the SDVS from in front of the detector so that the same detector may make both the scattered flux measurements and the velocity distribution measurements. This is accomplished by the SDVS frame shown in exploded view in Figure 9. The two ends of the frame are extended to one side where they are supported on pivots. The opposite side is supported by a simple jack screw (not shown) clamped half way along the side. The jack screw is operated from outside the vacuum wall by a combination linear and rotary feedthrough. The detector table is rotated to position the jack screw under the feedthrough drive shaft. The linear portion lowers the drive shaft to make the connection, and the rotary portion operates the screw. After raising the drive shaft, the table is rotated to the desired position to make the measurement.

The SDVS rotor described herein follows the design of HB with one major modification necessary for the present studies. Disk number 5 (in the notation of HB) has been removed. The removal of disk 5 opens a second channel (hereafter referred to as the low-resolution channel or small-angle path) through the rotor in the opposite angular direction from the original channel. The original channel is subsequently referred to as the high-resolution channel or the large-angle path. The resulting rotor is either a low-speed, high-resolution SDVS or a high-speed, low-resolution SDVS depending upon its direction of rotation. A high-order side band is unfortunately allowed to pass in either mode when disk 5 is removed and complicates the measured signal interpretation. A detailed discussion of the transmission of

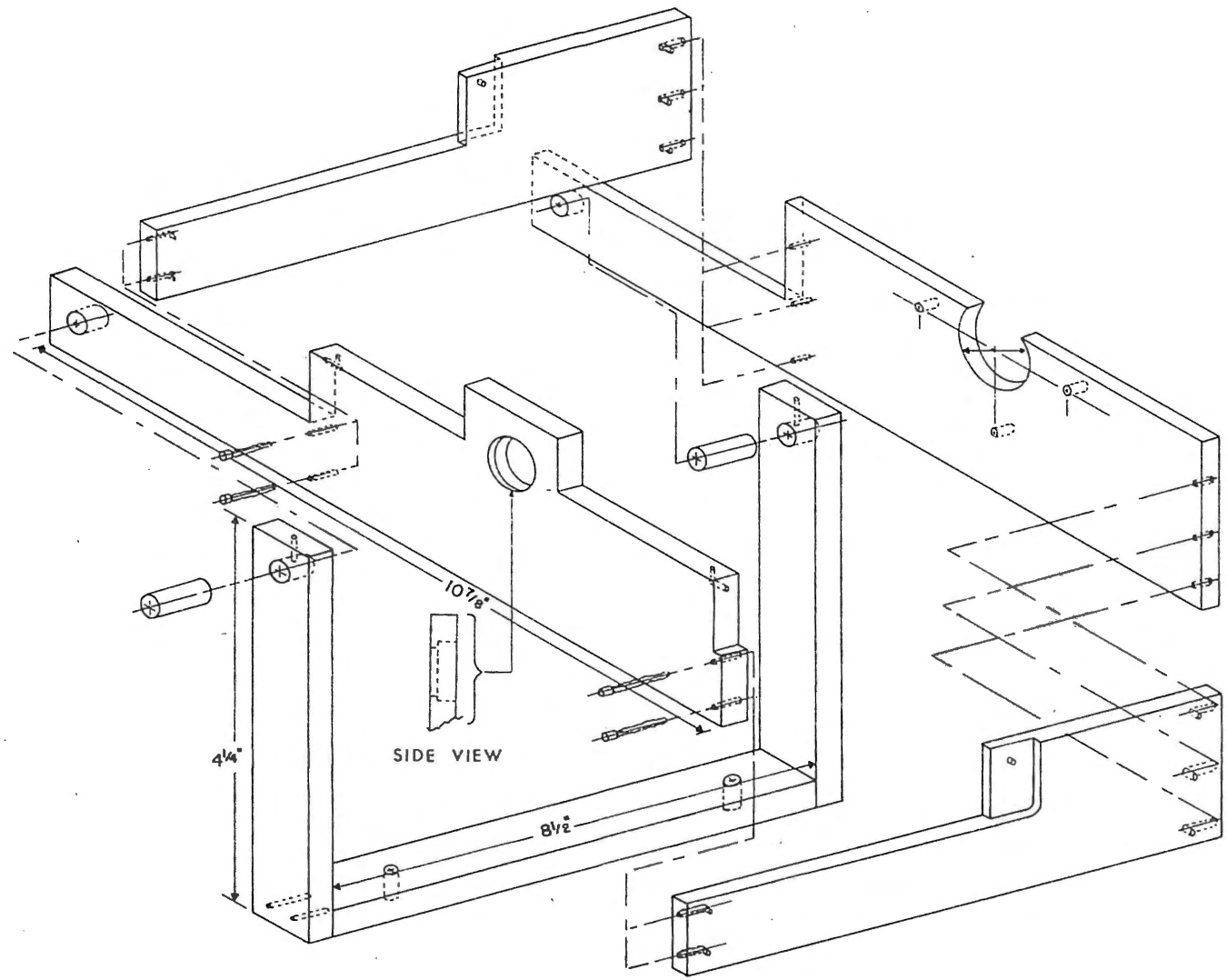

Figure 9. Exploded View of the Slotted-Disk Velocity Selector Frame

the present design and the deconvolution of its signal is included in the results section. The practical advantages of this design are discussed below.

HB's original design and the high-resolution channel of this design will measure velocity distributions up to a maximum of 1700 m/sec. corresponding to the maximum rotational speed of the drive motor, 400 Hz. Seventeen hundred meters per second just reaches the top of a room-temperature helium velocity distribution. The speeds of light particles arising from a nozzle source or ones which are accelerated by absorbing energy during a collision with a high-temperature surface might easily exceed this limit. Using the low-resolution channel, the rotor need rotate only about half as far in the same period to transmit a particle of equal linear velocity. Therefore, the transmission extends to 3380 meters/sec.

An SDVS having two open channels which operate under opposite rotation of the disks is inherently self-calibrating as to alignment. A speed distribution is measured using each channel. The maximum in each corresponds to the same particle speed. It is therefore possible to calculate the conversion factors relating rotational speed of the rotor to linear speed of the particles for each channel directly from the two measured maxima even though the particles may not be traveling parallel to the rotor axis.

The normal practice of lubricating the SDVS bearings with a small amount of diffusion pump oil is not practical at vacuum levels of 10^{-9} torr and below. The vapor pressure becomes too large as the bearings spin and warm up. For this reason, Barden Bar-Temp dry lubricated bearings are used. The advantage in using the low-resolution channel

for all measurements except calibration is that the lower rotational speeds greatly increase the useful lifetime of the bearings. Thirty distributions is about the useful lifetime since at these low pressures the balls within the bearings cannot sufficiently dissipate the heat. The balls pit and begin to vibrate generating noise in the signal through microphonics of the detector. Vibrations are minimized by dynamically balancing the rotor. A two-plane (dynamic) balancing technique must be employed rather than a one-plane (static) procedure because of the high rotational speed, the appreciable moment of inertia of the rotor, and the lack of a shock absorbing oil film in the bearings. The SDVS rotor was balanced with a tolerance of less than 5.0 microinches total vibrational runout in the center of the rotor shaft at 24,000 revolutions per minute.

The drive motor is a 400-Hz, 3-phase hysteresis synchronous motor. Common practice has been to use a variable oscillator, a capacitor-bank phase shifter, and a power amplifier to obtain reasonably pure 3-phase current to power the SDVS motor. With this arrangement, the power output at the amplifier is independent of operating frequency and may overheat the motor windings at the lower frequencies where I^2R losses are large. It also requires the manual tailoring of the capacitor bank for each desired frequency of operation since for a given capacitance the phase shift is frequency dependent. An alternative and considerably less expensive method is employed here. A simple motor-generator set (MGS), similar to that used in tachometer installations, is utilized. A Variac, rectifier, and LC filter section supply essentially ripple-free direct current to the d.c. motor portion of the MGS. The Variac alters the voltage supplied to the MGS and controls

the generated frequency. As the supplied frequency varies, the angular velocity of the SDVS varies. The total power output of the MGS is diminished when it operates at less than full speed and overheating of the SDVS motor is not a problem. However, vibration within the MGS limited its output to approximately 240 Hz and severely curtailed the present experiments.

A three-phase, variable-frequency power oscillator with automatic frequency control of the output power is currently being developed. Frequency Devices, Inc. manufactures a solid-state tunable oscillator with quadrature outputs. This series of quadrature oscillators provides two buffered outputs 90° ± 0.1° out of phase and independent of the frequency of operation. Model number 442 has a range of 0.5 to 500 Hz. The quadrature signals can be power amplified in a section where the gain is controlled by the signal frequency. The high-power, two-phase signal is converted to three phase by a transformer arrangement termed a Scott connection.[100] This power supply promises to be ideal for powering SDVS's. The phase shift of the outputs is independent of operating frequency, the power output decreases at low frequencies, and the output frequency is stable enough to permit holding the rotational speed of the SDVS constant (provided the SDVS bearings last) while very long-term signal averaging techniques are applied.

The Detector

A miniature ionization gauge detector is mounted 21.6 cm. from the target surface. A glass envelope 10 mm. in diameter and 25 mm. long is cemented with epoxy over each detector. In the side of each envelope is a tubulation 4 cm. long and 1 cm. in diameter.

Each detector is powered from a single supply outside the vacuum chamber. For maximum signal using an argon beam, a grid voltage of +160 volts is employed with a filament bias of +26 volts. The collector is held at 0 volts. An emission current of 5 ma was determined to give the greatest signal to noise ratio (S/N). The power supply consists of three independent, ripple-free, direct-current sources (Lambda Electronics Corporation) that are individually regulated. Figure 10 is the wiring schematic and Table II provides a list of the components and their specifications. The two high-voltage sources are internally regulated as constant-voltage supplies. The filament supply (PS3) is regulated by an external circuit which varies the filament power to regulate the emission current.

The emission current loop consists of electrons leaving the negative post of PS1 and traveling through R17, one of the emission pass resistors R13, R14, R15, or R16, and through point A to the filament. After being emitted at the filament and arriving at the grid, they return to the positive post of PS1 through M1. The emission current flows in the opposite direction to current normally supplied by PS2. R17 allows this "reverse" current to pass while diode D3 blocks it from entering the output stages of PS2. M1 and shunt resistors R18, R19, and R20 comprise a current multimeter circuit with full scale ranges of 1, 5, 10, and 25 ma for visual monitoring of the emission current. The emission current passing through one of the pass resistors R13 or R16 generates a voltage drop across that resistor. The differential amplifier IC1, R1, R2, R3, and R4 compares that voltage with the reference voltage generated in the voltage divider R9, R8, and P1 and amplifies the difference. The choice of R13, R14, R15,

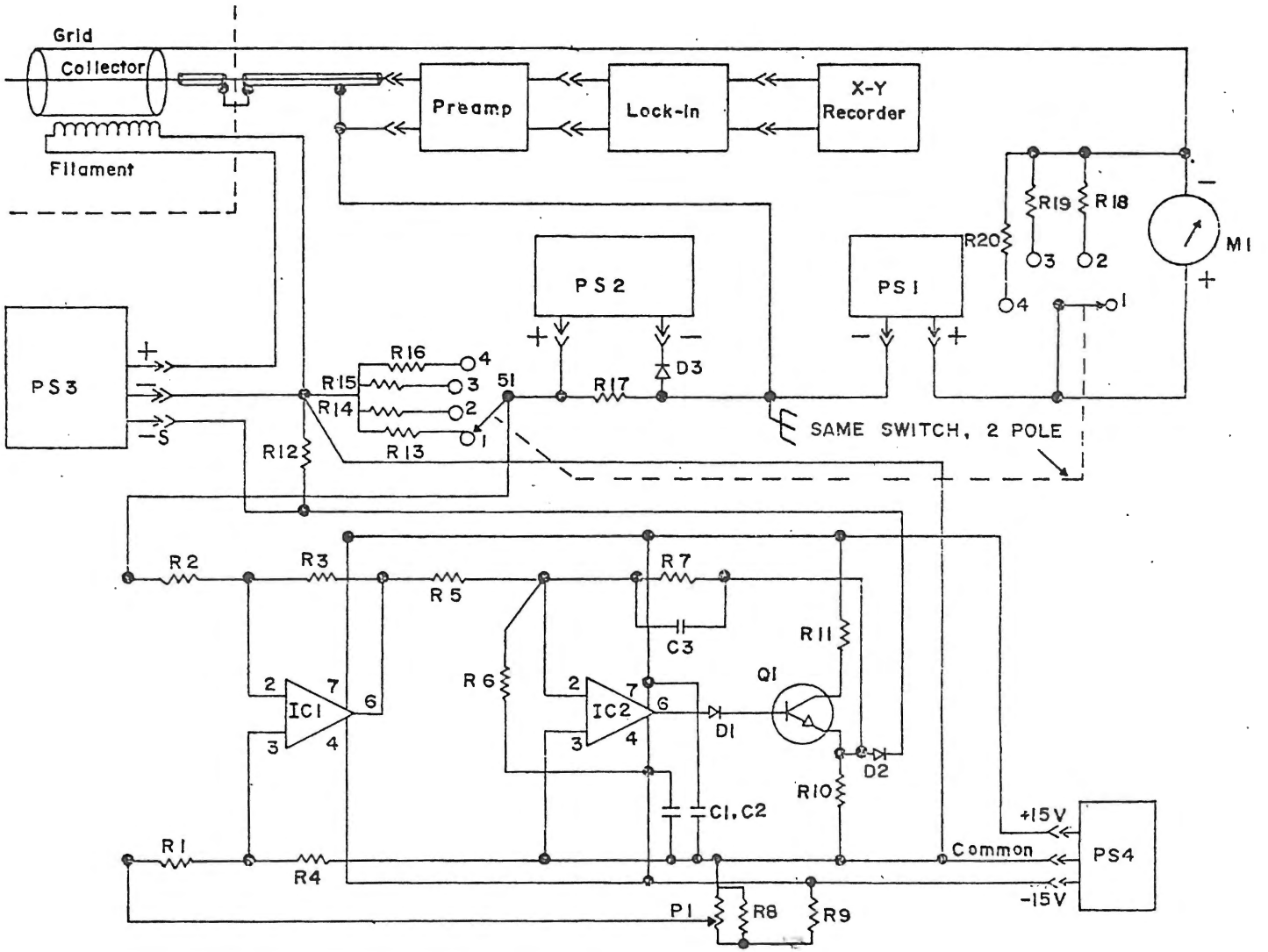

Figure 10. Detector Electronics

TABLE II

COMPONENT VALUES FOR DETECTOR ELECTRONICS

PS_1 - Power supply 1 - Lambda Electronics Corp., Model LR-616-FM

PS_2 - Power supply 2 - Lambda Electronics Corp., Model LR-413-FM

PS_3 - Power supply 3 - Lambda Electronics Corp., Model LP-520-FM

PS_4 - Power supply 4 - Burr Brown, Model 527

Resistors are all 0.5 watt carbon 10% unless otherwise specified

R_1 - 1.5K	R_{11} - 680
R_2 - 1.5K	R_{12} - 330
R_3 - 18K	R_{13} - 220, wire wound, 1%
R_4 - 18K	R_{14} - 39, wire wound, 1%
R_5 - 2.7K	R_{15} - 23, wire wound, 1%
R_6 - 270K	R_{16} - 5, wire wound, 1%
R_7 - 27K	R_{17} - 250, metal film, 25 watt
R_8 - 470	R_{18} - 25.6, wire wound, 1%
R_9 - 10K	R_{19} - 11.4, wire wound, 1%
R_{10} - 2K	R_{20} - 2.1, wire wound, 1%

P_1 - 400 Ohm potentiometer, 3 turn, 1/2 watt

C_1 & C_2 - 0.1 microfarad, 1KV capacitor

C_3 - 10 microfarad, 35 WVDC capacitor

D_1 & D_2 - Diode, silicon signal, IN645

D_3 - Diode, silicon signal, IN4004

Q_1 - Transistor, NPN, 2N2925, Si, General Purpose Amplifier

M_1 - 1 MA current meter (Rm = 1033 Ohm)

IC_1 & IC_2 - Operational amplifier, 741

S_1 - Switch, 2-pole, 4-position, shorting

or R16 sets the full scale emission amount at 1, 5, 10, or 25 ma, respectively. R5, R7, and IC2 provide a second stage of amplification. C3 in parallel with R7 limits the response time of the overall regulator. Q1 plus R11 and R10 amplifies the output current to a level sufficient to drive the negative sensing terminal of PS3. The output voltage between the plus and negative poles of PS3 is regulated within PS3 to match any voltage appearing between the negative pole and the minus sensing terminal. Two sources of voltage drop across R12 are present in the circuit. A constant current of 5 ma is generated by the internal regulator of PS3 and passes through the external circuitry between the minus sensing terminal and the negative terminal. Blocking diode D2 insures that this current does not flow into the output of the external regulator circuit. The 5 ma constant current was intended to provide a remote programming capability for PS3. A variation of R12 controls the output at a rate of 1 volt per 200 ohms. Consequently, R12 must be chosen 330 ohms or less so as not to drive the filament into emission. The second source of voltage appearing across R12 is the output of the external regulator circuit. The common reference point of the external regulator circuit is point A. The output of D2 is applied to the other end of R12 and begins to control PS3 as it exceeds the voltage generated by the 5 ma constant current passing through R12. R12 must, therefore, be large enough that the output current required from Q1 is not excessive.

S1 and S2 are two separate poles of the same four-position rotary shorting switch. To avoid ground loops, one and only one ground, point B, is provided for the entire power generating and signal measuring circuitry. The component modules PS1 through PS4 and the

signal recording components (preamp, lock-in amplifier, and x-y recorder) are all powered by 110 a.c. line voltage.

The signal generated by the beam at the detector consists of a small alternating current superimposed upon a much larger direct current coming from the background gas. The signal current is conducted from the detector collector via shielded cable to the input of a Keithley Instruments, Inc. Model 427 preamplifier located outside the vacuum wall. Good signal processing technique dictates that the impedance shift of the preamplifier be located as close as possible to the detector in order to minimize noise pickup by the signal lead. Actually, the antenna effect of the signal lead appears to be a negligible noise source for the present arrangement. Mechanical vibration is the main source, particularly when the SDVS rotor is spinning. In fact, a significant reduction in noise was made by replacing the original thin wire (0.10 mm.) collector of the detector with a much thicker (1.0 mm. diameter) tungsten wire. This conversion decreases the amplitude and increases the frequency of the collector's vibration within the electric field of the grid. The remaining major noise sources are: 1) vibration of the detector, 2) movement of the signal lead causing friction between the woven glass insulation of the shielded cable and the central conductor, and 3) random fluctuations of the gas stream entering the detector. Fluctuations arise from interactions of the beam with high-density background gases in the nozzle-skimmer vicinity and from varying conditions of the solid surface such as thermal motion of the surface atoms and desorption of adsorbed particles.

After passing the preamplifier stage, the a.c. voltage signal enters a lock-in amplifier, Model HR-8, purchased from Princeton Electronics Corporation. This device amplifies and filters the signal, then compares that signal with the reference generated at the mechanical beam chopper. The lock-in amplifier output is a ±10 volt signal proportional to that fraction of the input signal which has the same frequency as the reference. The output appears across a capacitor blank the size of which may be altered to modify the dynamic response (time constant) of the instrument.

The inherent electrical noise (beam off but detector electronics on) had a peak-to-peak value of 4×10^{-13} amps. Maximum recorded signals were 6×10^{-9} amps. The zero signal level may be suppressed by up to an order of magnitude to conveniently display very small changes in large signals.

The phase shift between the chopper reference signal and the beam was found to be approximately 15°. This lag in the beam signal arises from the finite length of time required by the gas particles in the beam to traverse the chamber and enter the detector after passing the beam chopper.

The output from the lock-in amplifier goes to the ordinate of a Model 520 x-y plotter manufactured by Electro Instruments. For the spatial scattering distribution measurements, the signal to the abscissa arises from a simple potentiometer circuit attached to the rotary feedthrough which drives the detector turntable around the target. When the velocity distribution of particles in the beam is measured, the abscissa is the analog output of a Hewlett-Packard Model 5300A digital frequency meter and a Model 5311A digital-to-analog converter.

Two sources of a signal proportional to the rotational speed of the SDVS exist in the apparatus. The most direct source is the motor of the SDVS. The frequency meter monitors the a.c. voltage generated by two of the three SDVS motor windings as the rotor slowly coasts to a stop. A higher-resolution measurement was made possible by placing a photodiode and a photosensitive resistor so that the points of the hexagonal nut which clamps the SDVS disks to the shaft interrupt the light path six times per rotation. The digital frequency meter monitors the resulting square wave.

The Target Heater

The target heater used in these experiments is similar in design to a vacuum tube diode. Electrons are emitted by a hot-wire filament and accelerated to the plate by a large, positive potential. In this case, the plate is the backside of the tungsten single crystal. A repeller electrode, maintained at a slightly negative potential, focuses the electron beam onto the crystal where the kinetic energy of the electrons is converted to heat. The opening of the repeller electrode is located 2 mm. from the back side of the target. The coiled filament is contained within the cup of the electrode. The filament is formed "in house" from a 2 cm. length of 0.152 mm. diameter tungsten-2% thorium filament wire. The annealed filament wire was purchased from the C. W. French Division of The EBTEC Corporation. It is usually considered necessary to work tungsten wire while hot and to use a heated mandrel. This thin wire, however, could be formed very nicely by simply wrapping it into 12 loops about a 1.3 mm. diameter rod. The filaments did become very brittle after prolonged heating.

The repeller electrode is 0.076 mm. thick tantalum formed into a parabola. Small tabs are bent around the sides leaving two holes for the filament to pass through and spot welded in place. This electrode is electronically isolated. A few of the electrons emitted by the filament strike the electrode and build up a negative charge. This charge then focuses the remaining electrons into a beam traveling towards the crystal. A positive 1500 volts d.c. is applied by the high-voltage section of the power supply (Figure 11) to the crystal. The emission current is controlled by regulating the filament temperature. The schematic of the low-voltage filament regulator is in Figure 12.

The high-voltage section of the power supply consists of a step-up transformer, full-wave rectifier, and an RC filter. No regulation is provided. R2 and R3 provide a path by which the charge stored on capacitors C1, C2, and C3 may dissipate when the supply is turned off. R5 will limit the current surge if the high-voltage lead is shorted to ground. The emission current flowing through R6 generates a voltage which may be monitored with M2 and the associated range-selecting shunt resistors, R7 through R14, or by monitoring the voltage at J1. The neon bulb connected in parallel with R6 acts as a spark gap protection device which begins to conduct at 70 volts. As built, either the positive or negative lead of this circuit may be grounded through R6 provided M1 is connected to that lead and R5 is wired into the other lead. The low-voltage filament section cannot float off ground potential.

The low-voltage regulator circuit illustrated in Figure 12 is an adaptation of a circuit designed to control the filaments of electron microscopes.[101] Two major changes have been made. The power supply

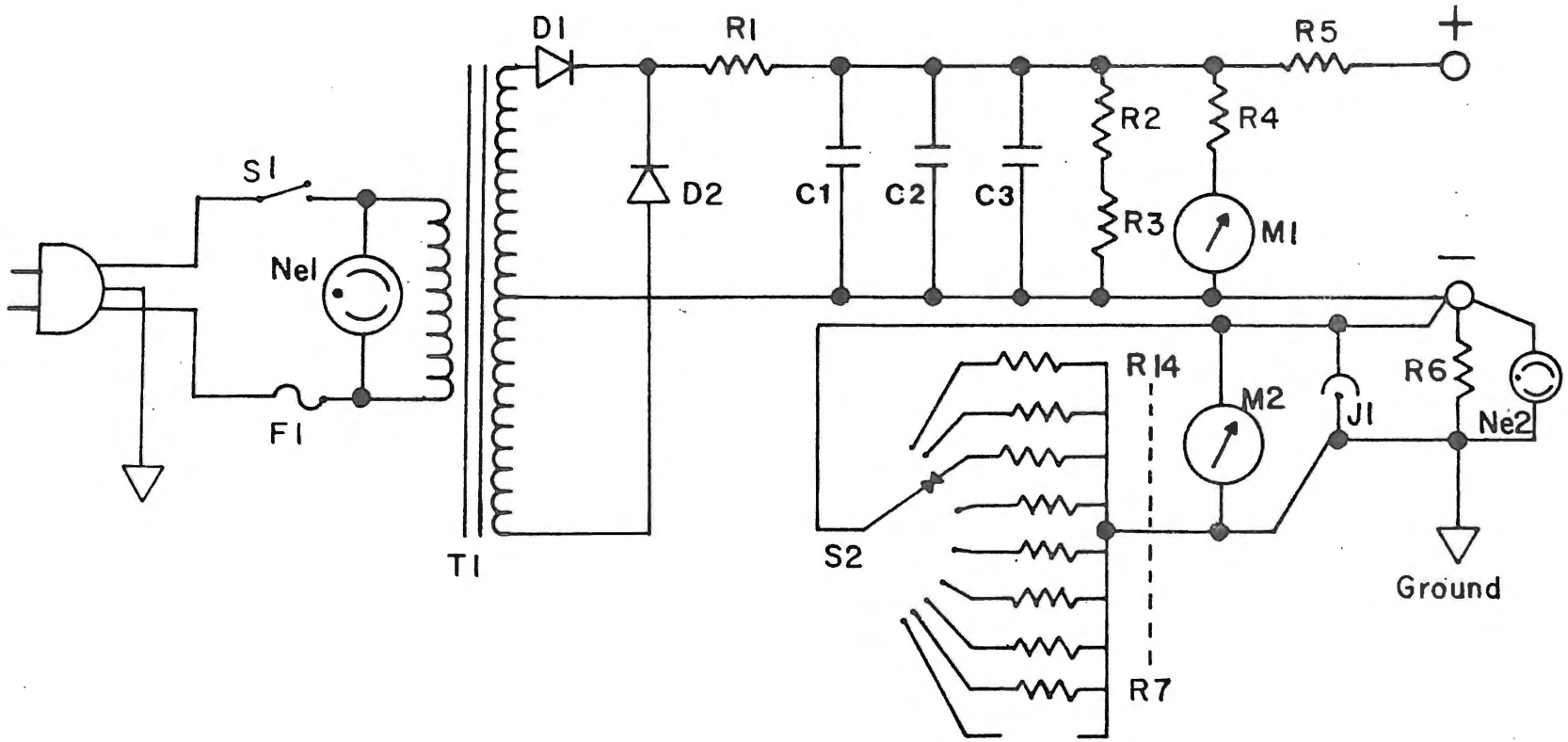

Figure 11. High-Voltage Section of the Target Heater Power Supply

TABLE III

COMPONENT VALUES FOR THE HIGH-VOLTAGE SECTION
OF THE TARGET HEATER POWER SUPPLY

R_1	- 500 Ohms, wire wound, 250 watt
R_2	- 4.7 M Ohms, carbon, 0.5 watt
R_3	- 330K Ohms, carbon 0.5 watt
R_4	- 1.3M Ohms, carbon, 0.5 watt
R_5	- 250 Ohms, wire wound, 100 watt
R_6	- 1 Ohm, wire wound, 5 watt
R_{7-14}	- Meter shunt resistors (chosen to provide full scale ranges between 50 microamps and 500 milliamps in a 5,1 sequence)
C_{1-3}	- Capacitor, 4 microfarad, 3KV d.c., electrolytic
M_1	- Calectro No. D1-921 meter, 0-120V d.c. remarked 0→1500 V d.c.
M_2	- Calectro No. D1-910 meter, 0-50 microamps
NE_1	- Pilot lamp, 110V a.c.
NE_2	- Neon bulb, 70 volts
S_1	- Switch, 250 volts, 15 amps, DPDT
S_2	- Switch, rotary, 1P9T, shorting
D_{1-2}	- Power diodes, Varo No. VC60, 6K PIV, 10 amps
J_1	- BNC connector, male
F_1	- Fuse assembly, fuse, 3 amp slo-blow
T_1	- Transformer, isolation, step-up, 110 primary, 2 KV center-tap secondary, 1 KVA

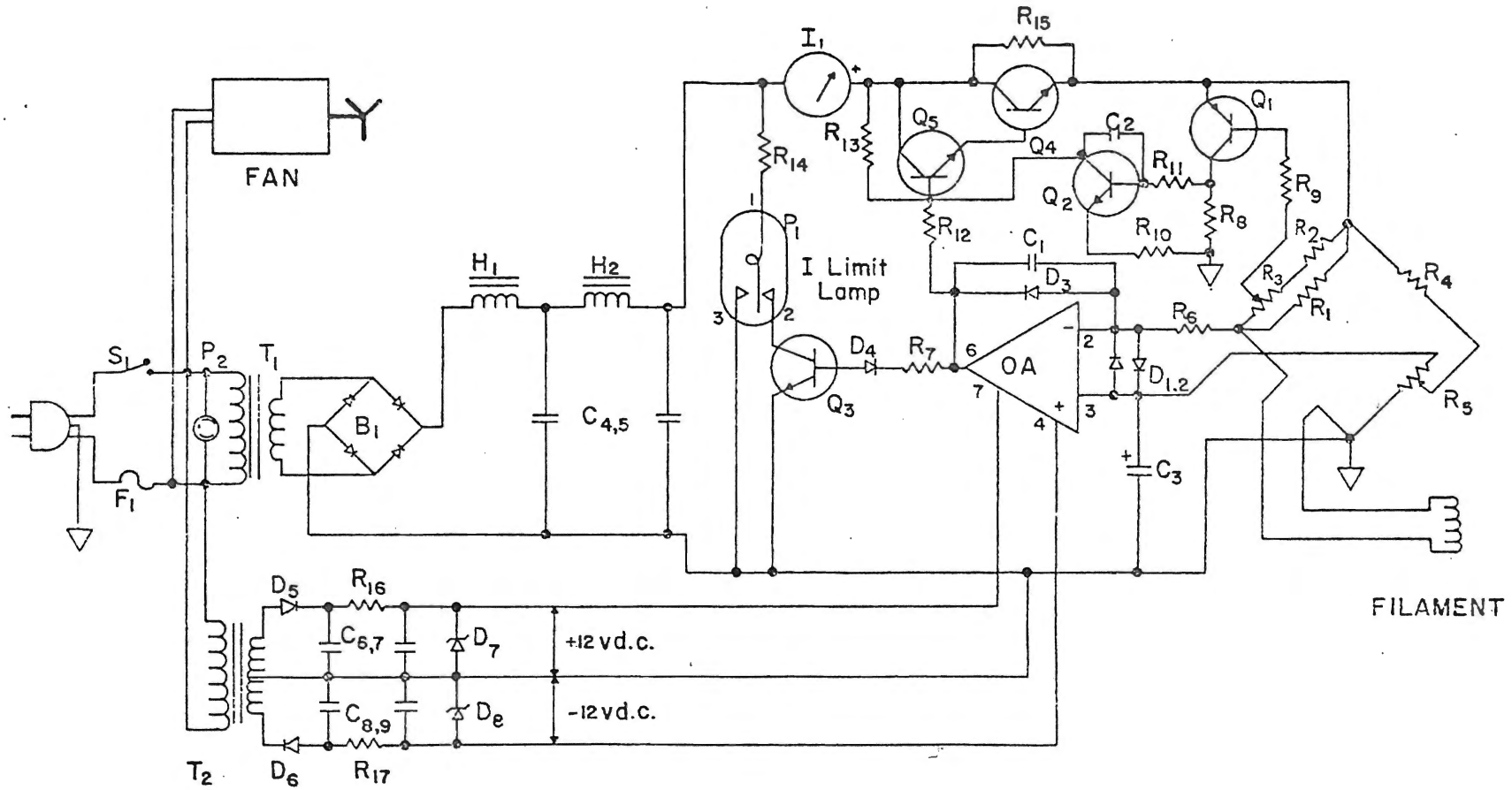

Figure 12. Element Temperature Regulator

TABLE IV

COMPONENT VALUES FOR FILAMENT
TEMPERATURE REGULATOR

R_1	- 0.5 Ohms, wire wound, 5 watt
R_2	- 15 Ohms, carbon, 0.5 watt
R_3	- 25 Ohms, wire wound, single turn potentiometer, 5 watt
R_4	- 1K Ohms, carbon, 0.5 watt
R_5	- 10K Ohms, 10 turn, wire wound, potentiometer
R_6	- 4.7K Ohms, carbon, 0.5 watt
R_7	- 1K Ohms, carbon, 0.5 watt
R_8	- 12K Ohms, carbon, 0.5 watt
R_9	- 3.3K Ohms, carbon, 0.5 watt
$R_{10,11}$	- 270 Ohms, carbon, 0.5 watt
R_{12}	- 3.3K Ohms, carbon, 0.5 watt
R_{13}	- 68K Ohms, carbon, 0.5 watt
R_{14}	- 56 Ohms, carbon, 0.5 watt
R_{15}	- 100 Ohms, carbon, 12 watt
$R_{16,17}$	- 310 Ohms, carbon, 0.5 watt
$D_{1,2,3}$	- Diode, silicon signal
D_4	- Zener diode, 10Vz, 400 mw, IN5240
$D_{5,6}$	- Diode, silicon signal
$D_{7,8}$	- Zener diode, 12Vz, 1.0 watt, IN4742
C_1	- 0,0022 microfarad capacitor, mylar
C_2	- 0.0033 microfarad capacitor, mylar
C_3	- 60 microfarad capacitor, tantalum
C_4	- 2000 microfarad capacitor, electrolytic

TABLE IV (Continued)

C_5	- 4000 microfarad capacitor, electrolytic
$C_{6,7,8,9}$	- 47 microfarad capacitor, electrolytic
Q_1	- Transistor, PNP, 2N5087, small signal type
Q_2	- Transistor, NPN, 2N3405, small signal type
$Q_{3,5}$	- Transistor, NPN, 2N3569, switching type
Q_4	- Transistor, NPN, 2N5192, power type
OA	- Operational Amplifier, 741
B_1	- Full wave bridge rectifier, silicon 200 PIV, 6 amp
T_1	- Transformer, 110V primary, 20V secondary at 3 amps
T_2	- Transformer, 110V primary, 25V secondary with center tap
$H_{1,2}$	- Choke, 0.025 Hys, 4 amps d.c., 0.425 Ohms d.c. resistance, 1500 V r.m.s. insulation test
I_1	- Meter, Calectro No. D1-918, 3 amps d.c. full scale
P_1	- Pilot lamp assembly, press to test, lamp-328: 200 ma, 6V
P_2	- Pilot lamp, neon, 110V a.c.
F_1	- Fuse assembly, Fuse-3 amp, instrument type
S_1	- Switch, toggle, DPST
Fan	- Cooling, 60 CFM
Filament	- Tungsten - 2% thorium, 2.9 Ohms

now operates from a.c. line voltage instead of batteries and the emission current range has been increased by three orders of magnitude. Direct current is derived from that portion of the circuit which consists of stepdown transformer T2, the full-wave bridge rectifier B1, and the two LC filter sections H1, C1 and H2, C2. A subsection, comprised of transformer T3, diodes D1 and D2, two π-section filters, and zener diodes D3 and D4 provides regulated plus and minus 12 V d.c. to power the operational amplifier.

One method of regulating an electron beam current is to control the filament temperature. Neglecting long-term changes of the filament due to sputtering and crystallization, the resistance of the filament is defined only by the temperature. Hence, if the resistance of the filament is kept constant, the temperature will remain constant.

The circuitry illustrated in Figure 12 performs two separate functions, the first of which is to maintain the resistance of the gun filament constant. The resistance of the metal wire filament (which has a positive temperature coefficient) is compared with that of the TEMP. ADJ. potentiometer. Any bridge unbalance voltage is amplified by the 741 operational amplifier and transformed, via transistors Q4 and Q5, into a compensating change in filament current. The second circuit function is to prevent the filament current from exceeding safe limits. The current-limit adjust control, (R3), is used to limit the cold filament inrush current to a preselected value within a range of one to three amps. That portion of the circuit, including transistors Q1 and Q2, takes over control of series-pass transistors Q4 and Q5 when the preset limit is exceeded. In addition to indicating a shift to current-limiting operation, the current-mode lamp will turn on to

indicate a burned-out filament or a filament overvoltage resulting from a shorted series-pass transistor.

Initial warm up of the crystal required a few minutes since much of the electron beam power was heating the crystal holder. After the crystal and its holder equilibrated and stabilized at the final temperature (10-15 minutes), the surface temperature of the target remained constant within the measurement precision of the optical pyrometer. A maximum temperature gradient of thirty degrees could be observed across the target face at the highest surface temperature used, 2200 K. All temperature measurements reported herein were taken from the hotter, central portion of the target. The only instance of faulty regulator operation during these experiments resulted from poor connections at the tungsten feedthroughs.

Alignment and Evacuation Procedure

Alignment

The alignment of the apparatus was performed in the following manner. The equipment was assembled but the rear wall of the nozzle chamber, the nozzle, and nozzle holder were not installed. Alignment of SK1, SK2, the target, SDVS, and the detector was then checked using a small laser and a cathetometer precise to ±0.001 mm. Alignment of the nozzle using the laser is not possible since the glass or quartz wall of the barrel reflects and diffracts the laser light.

The alignment of the nozzle with the first beam-defining skimmer is very critical if the maximum useful beam signal is to be achieved. The nozzle tip and SK1 are very close. Any misalignment would result

in the majority of the beam not passing into the main scattering chamber through SK2. It is, therefore, necessary that the final alignment be performed by using the beam intensity at the detector as the criterion.

After disassembly of the buffer chamber, the initial rough alignment of the nozzle was performed by viewing the nozzle tip from the downstream side of SK1 with a small, 5-power telescope designed for reading thermometers. The nozzle holder has a window at its rear end and a powerful lamp is located just behind the window. The light from the lamp travels through the settling chamber of the holder and along the nozzle barrel, illuminating the tip for viewing.

After the apparatus had been reassembled without SK2 and evacuated to 10^{-8} torr, the beam was turned on and the signal at the detector maximized by scanning the nozzle tip back and forth past SK1. After SK2 was reinstalled, the process was repeated insuring the final alignment. The angular alignment of the target surface may be tested during the course of experiments by observing the image of SK2 reflected from the polished target surface.

Evacuation of the System

A gate valve is normally incorporated in high-vacuum systems between the diffusion pump and the liquid nitrogen trap. This allows the trap to be isolated during the start-up of the diffusion pump when backstreaming of the boiler fluid is heavy. The disadvantages of including such a valve in the present system are: 1) gate valves capable of operating down to or beyond 10^{-10} torr are extremely expensive, and 2) the added distance required between the diffusion

pump inlet and the chamber would limit the pumping speed of the stack. An alternative pump-down procedure has been developed that gives equivalent results but does not require the use of a gate valve. Much of the success of this procedure is attributable to the use of a diffusion pump oil of extremely low vapor pressure. Convalex-10, a polyphenol ether, purchased from Consolidated Vacuum Corporation, has an advertised vapor pressure specification of 10^{-13} torr at 25°C.

The initial pump-down proceeds as usual. The mechanical pumps are started. The rough pumping is accelerated by starting the blower as the pressure falls below 5 torr. As the pressure passes 100 microns the four-inch diffusion pumps on the nozzle and buffer chamber are started and liquid nitrogen is added to the trap between the six-inch pump and the main scattering chamber. After the trap is full, the heater of the six-inch pump is turned on. About one-half hour is required for the boiler to come up to operating temperature. During this period of time a number of different species are removed by the cold surface of the liquid nitrogen trap. Solvents, water, carbon dioxide, oxygen, etc., as well as mechanical pump oil and diffusion pump oil, are frozen onto the cold surface. Unfortunately, many of these have appreciable vapor pressures even at liquid nitrogen temperatures and would limit the base pressure of the system if they are not removed. Therefore, after the pressure has reached 10^{-8} torr and the operation of the six-inch diffusion pump has stabilized (usually about 2 hours), the trap is allowed to warm up to room temperature. The pressure in the main chamber quickly rises to 10^{-5} torr. As the pressure begins to fall into the 10^{-6} range, bakeout is begun. The temperature of the chamber wall is slowly increased, the pressure being

kept in the 10^{-5} torr range until a temperature of 150°C is reached. This temperature is maintained while the materials of higher vapor pressure and the gas leaching from the metal of the system are pumped out. When the pressure enters the 10^{-8} torr range, the heating tapes are turned off and liquid nitrogen is reintroduced to the trap. The pressure quickly falls to the low 10^{-9} range. The pressure then slowly drops over the course of the next 2 or 3 days until the lowest attained pressure, 2×10^{-10} torr, is reached.

In order to decrease the costs of these experiments, an attempt was made to conduct them without reintroducing liquid nitrogen into the trap. A base pressure of 2×10^{-9} torr was achieved. Unfortunately, the very interesting results reported in the next chapter cannot be observed at that "high" pressure. The character of the surface does not remain constant long enough to permit completing an observation.

The first time this system was evacuated into the 10^{-10} torr range, a bakeout period of 10 weeks at 150°C was required. A pressure of 5×10^{-10} torr was obtained. It currently requires just over one week to reach 2×10^{-10} torr. This initially long pump-down was almost certainly due to oil leaching from the metal. This oil enters the metal during the machining processes. Metal being cut by a bit is locally heated to a very high temperature allowing oil and water to enter expanded cracks in the surface. The relatively mild bakeout temperatures which have been employed could not have removed all the oil and water. It might be possible to reach even lower pressures with the present apparatus if it were assembled without the electronics inside and baked at a much higher temperature (300°C to 400°C). A very dry

inert gas is used to bring the system back up to atmospheric pressure. Nitrogen gas from above the liquid nitrogen in the supply tank is normally used.

CHAPTER III

RESULTS AND DISCUSSION

Characterization of the Incident Atomic Beams

All the tests reported here were conducted using an inert gas beam generated via a glass nozzle. The beam was extracted from a body of gas in thermal equilibrium at 290 K. The detector employed for all the tests was sensitive to the total particle flux entering the detector envelope. However, the presence of the slotted disk velocity selector, interposed in the path of the beam before the detector opening, allowed the evaluation of the number density distribution of particle speeds in the incident beams. Figure 13 is a measurement of beam width at the detector for the experimental dimensions listed in Table I. This width at the detector implies a beam width of 2.6 mm. at the target.

The relative spread in the flux and number density distributions is indicated by the "speed distribution",[91] SD, where

$$(SD) = \frac{1}{\bar{v}} \left(\int P_n(v)(v-\bar{v})^2 dv / \int P_n(v) dv \right)^{\frac{1}{2}} \quad . \tag{10}$$

This is the root-mean-square deviation in particle speed divided by the mean speed of all particles in the beam. For an ensemble of particles in thermal equilibrium (Maxwellian speed distribution), SD is 0.363. The factor $P_n(v)$ contains the distribution per unit volume and $\bar{v}$ is the mean speed of particle flux in a differential solid angle of the beam.

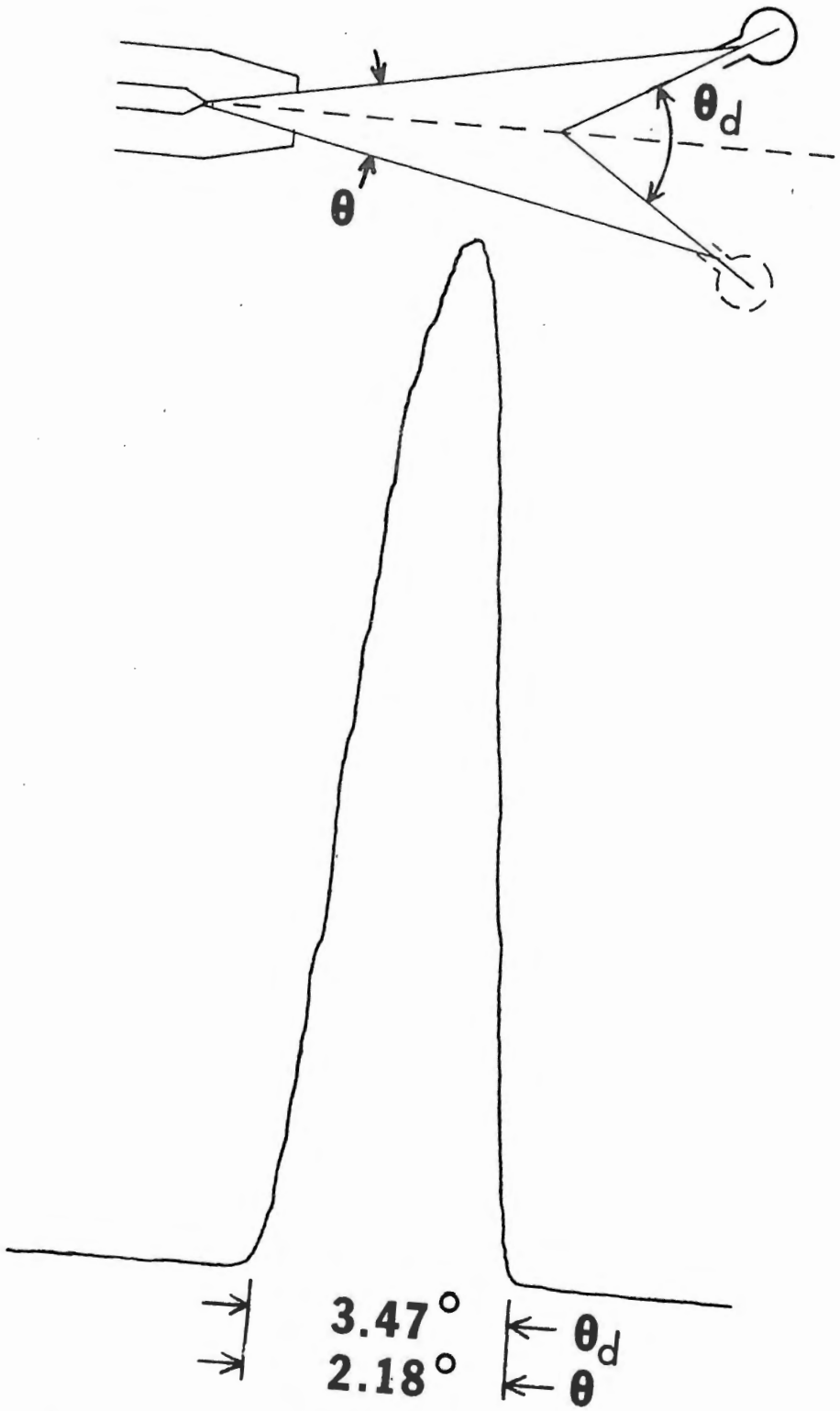

Figure 13. Measured Incident Beam Width

Most tabulations of gas properties in flow situations are in terms of Mach number, even though it is literally a meaningless concept in connection with molecular beam experiments. Clearly there can be no compression waves and, therefore, no speed of sound in a collisionless gas. The usage is purely one of convenience. Because the local speed of sound is a measure of temperature, Mach number becomes equivalent to a measure of ordered motion (mean gas stream velocity) relative to random thermal motion. It is shown by Moran[91] that the speed distribution is related to the jet Mach number at the transition to free molecular flow, if one assumes that the transition does not affect the velocity distribution, by:

$$M_t^{-1} = (SD)(\gamma)^{\frac{1}{2}} \tag{11}$$

where γ is the ratio of specific heats of the gas and M_t is the Mach number. The measured argon velocity distribution presented in Figure 14 results from the supersonic nozzle of Figure 4 when operated at a pressure differential of 80 torr and a temperature of 298 K. This distribution is characterized by a SD = 0.155 and a jet Mach number of 5.0. Changing to a "cone"-type first skimmer and greatly increasing the pumping speed of the nozzle chamber should allow operation at a Mach number in the range of 15 to 20 with a corresponding tenfold increase in beam intensity. For contrast, a theoretical velocity distribution of an argon beam resulting from an effusive source is included in Figure 14. The areas under the two curves are normalized to unity. The expected shift towards higher velocity and the narrowing of the distribution for the supersonic beam is clearly apparent. The abscissa of Figure 14 is marked in two scales. The bottom is marked in

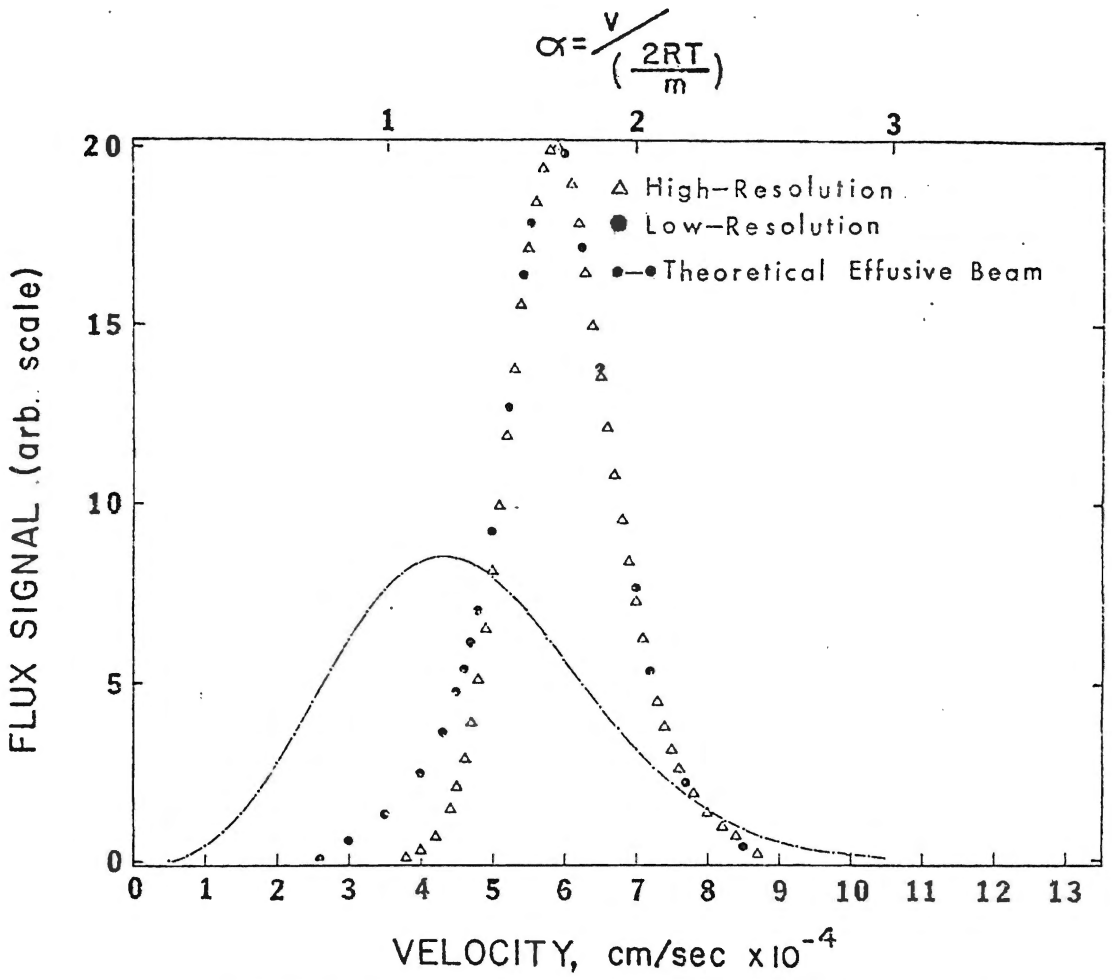

Figure 14. Measured Argon Velocity Distribution Generated by the Nozzle of This Work (Δ and O) and a Theoretical Argon Velocity Distribution Resulting From an Effusive Source (∘—∘). The Areas Under the Curves are Equal

units of centimeters per second while across the top are units of reduced velocity defined as: the velocity divided by the most-probable velocity of a gas in thermal equilibrium with its surroundings (a Maxwellian gas).

The raw high-resolution and low-resolution data from which the experimental supersonic curves of Figure 14 are derived are shown in Figure 15 and 16, respectively. Clearly, the ratio of signal to noise is not a problem for incident beam velocity distributions. However, when attempting to measure velocity distributions of particles reflected from the solid surface where gas stream intensities are a factor of 500 to 1000 times smaller, the best signal-to-noise ratio obtained was equal to one. Modifications of the apparatus to increase the beam intensity have already been discussed and should allow this type measurement to be made.

A listing of the dimensions of the rotor and definitions of the terms used throughout this discussion are in Table V and Figures 17 and 18. These drawings show the "unrolled" surface of the rotor disks. In this representation trajectories of particles are straight lines. The tangent of the angle of inclination of the line relative to the beam direction is proportional to the molecular speed. Molecules of the desired velocity are transmitted by passing through those slits of the end disks which are displaced (rotated) through the angle Φ_i. Figure 18 is a representation similar to Figure 17, showing only the two end disks and the relationships among v_o, v, $v_{max.}$ and $v_{min.}$

Figures 17 and 18 are drawn for the condition where the slit width, l_1, and the tooth width, l_2, are equal. Since the slits are of finite length extending over a small range of the disk radius, the

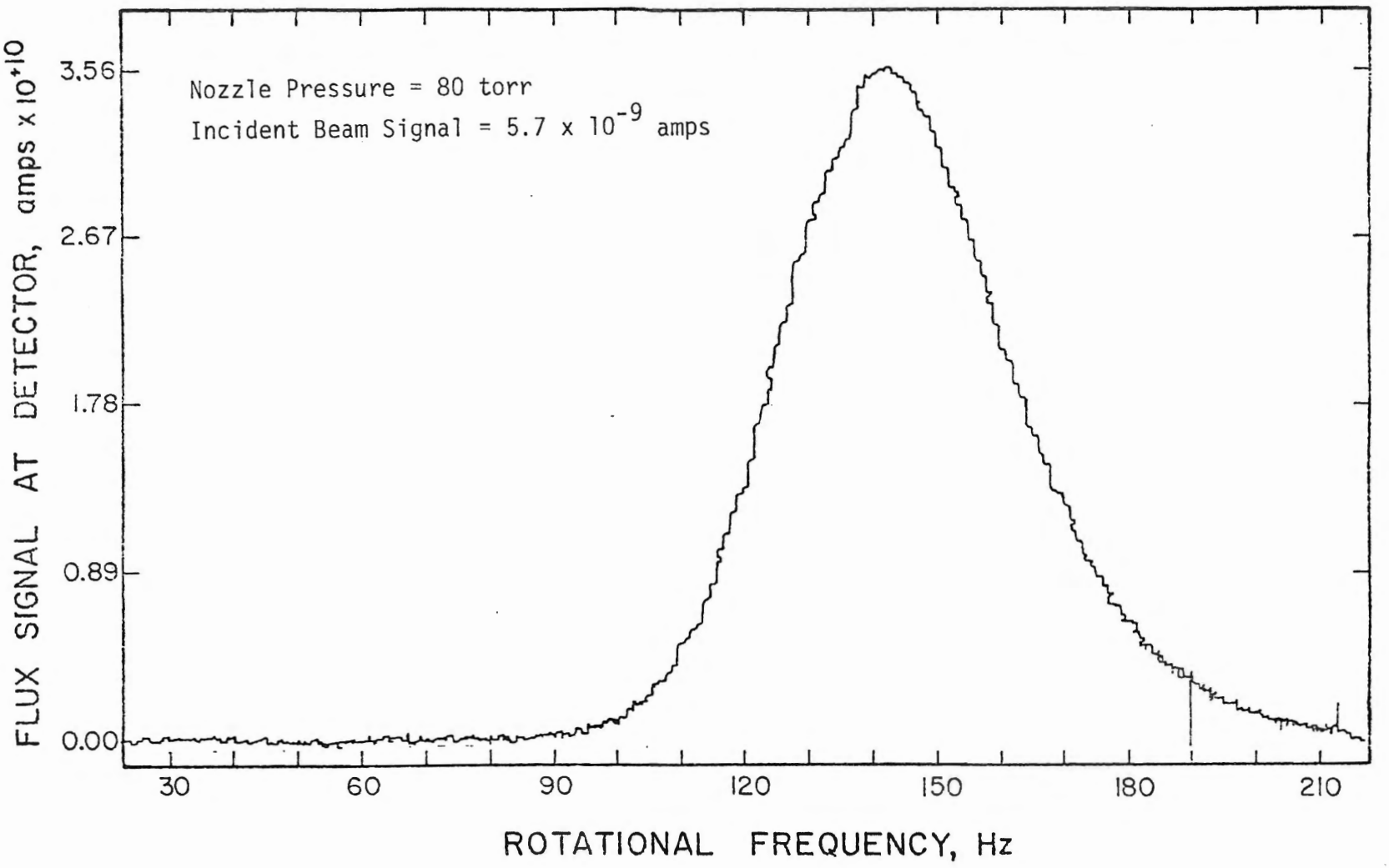

Figure 15. Argon High-Resolution Velocity Distribution; Raw Data

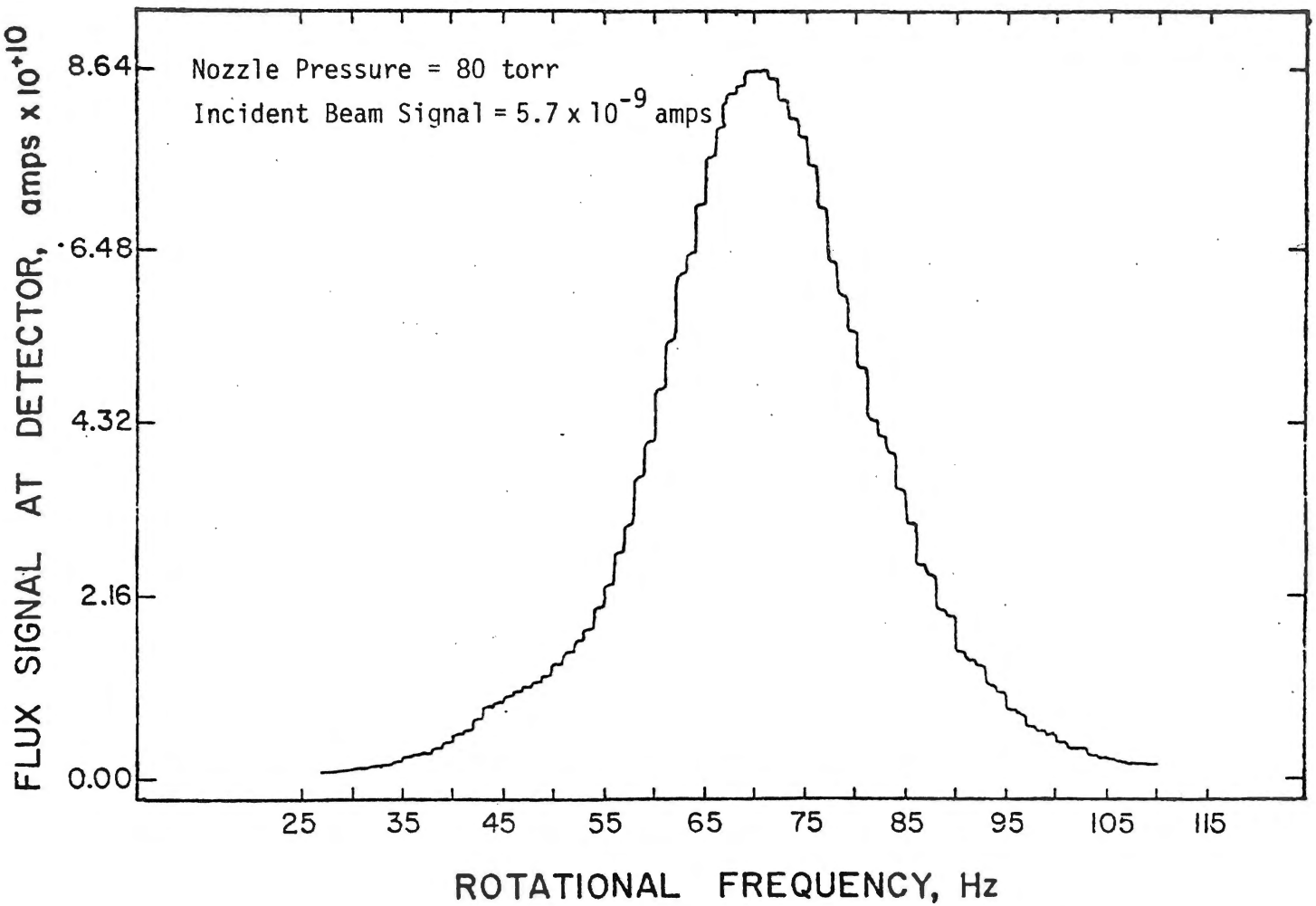

Figure 16. Argon Low-Resolution Velocity Distribution; Raw Data

TABLE V

THE DIMENSIONS AND PARAMETERS OF THE SLOTTED DISK VELOCITY SELECTOR

Number of disks = 5

Number of slots per disk = 280

Diameter of disk = 15.99 cm.

Length of slot = 0.795 cm.

Slot width = ℓ_1 = 0.0795 cm.

Tooth width = ℓ_2

At base of slot = 0.0823 cm.

At top of slot = 0.1000 cm.

Average value = ℓ_2 = 0.0912 cm.

Radius to one-half the slot length = r = 7.598 cm.

Disk thickness = d = 0.1588 cm.

Overall length = L + d = 10.16 cm.

L = 10.00 cm.

$\beta = d/L = 0.01587$

$$N = \frac{\ell_1}{\ell_1 + \ell_2} = 0.4658$$

The numerical values of the following variables depend upon the particular channel and upon the beam direction relative to the axis of rotation. The subscript i indicates the particular channel as defined in Figure 18.

ϕ_i = depends upon beam direction

$\gamma_i = \ell_1/(r\phi_i)$

$N_i' = N(1 - \beta/\gamma_i)$ = effective open time

$R = \gamma_i - \beta$ = resolution

$\nu_{i,max.} = \nu_o(\frac{1-\beta}{1-\gamma_i})$ (illustrated in Figure 18)

$\nu_{i,min.} = \nu_o(\frac{1+\beta}{1+\gamma_i})$ (illustrated in Figure 18)

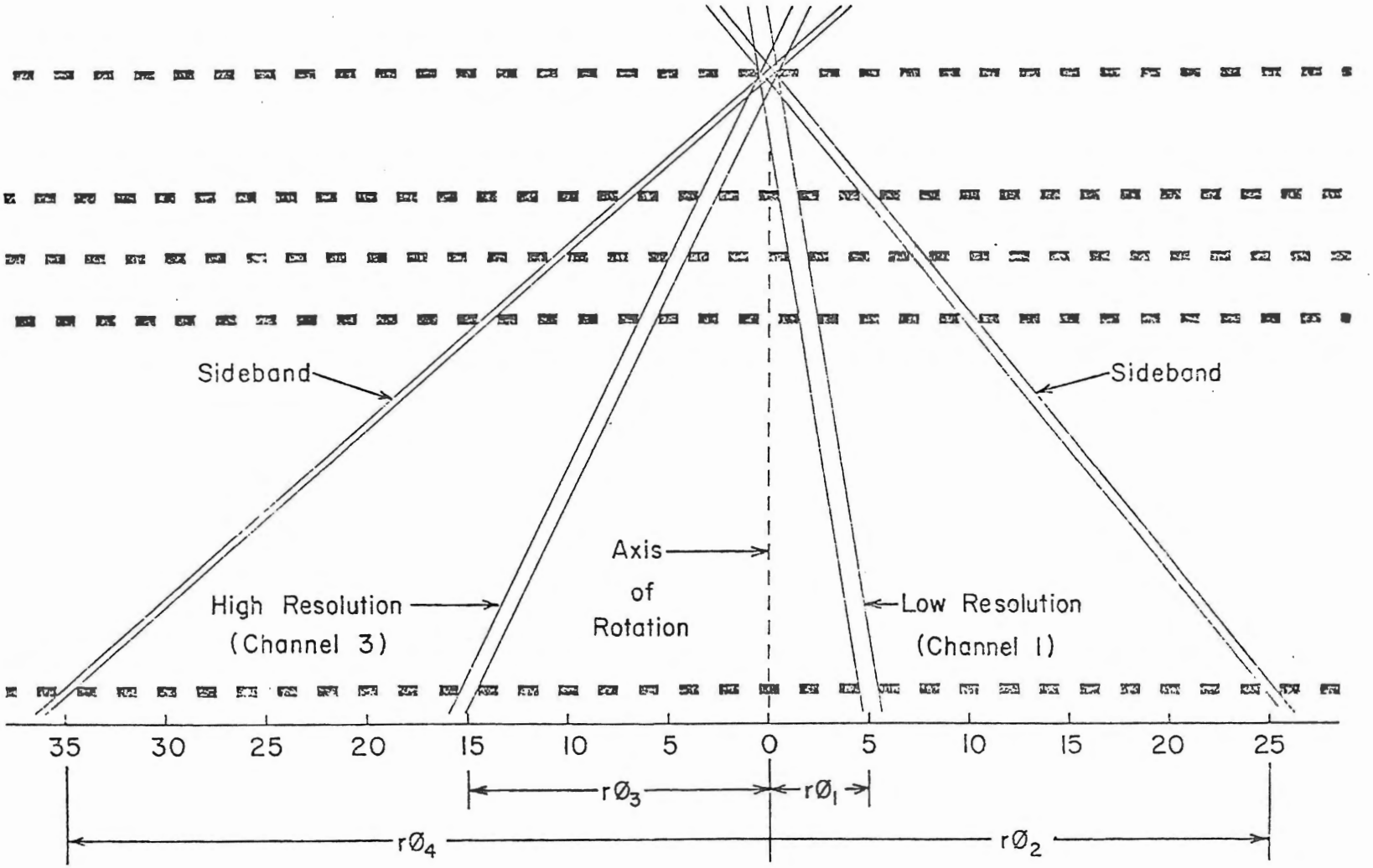

Figure 17. "Unrolled" Representation of Slotted-Disk Velocity Sector Disks

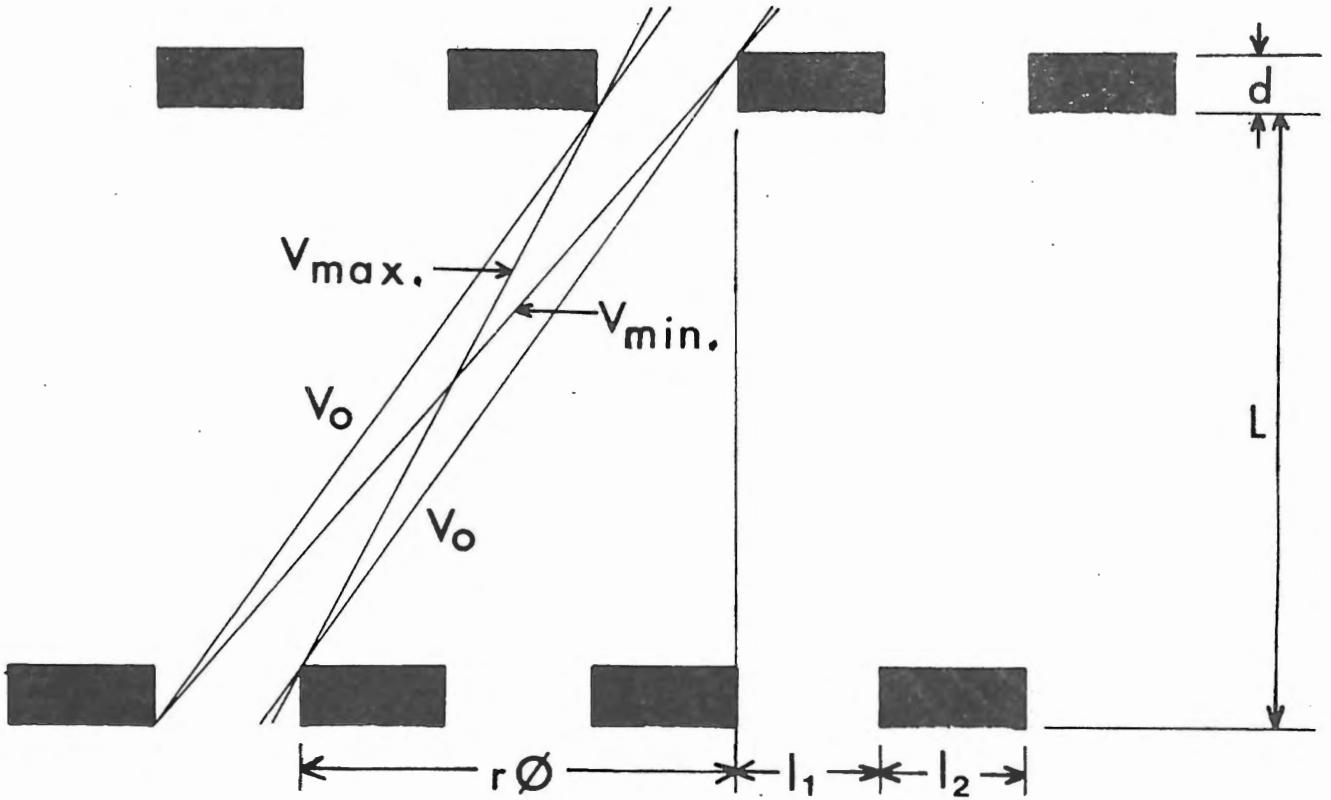

Figure 18. Representation of V_{max}, V_{min}, and V_o Which Pass the First and Last Disk

tooth width varies slightly from one end of the slit to the other. For the actual disks, ℓ_2 is slightly larger than ℓ_1 even at the base of the slit. However, in connection with the problem of sideband elimination, this is the least favorable case and has been chosen for the figures. For the calculations of transmission and resolution of a channel, the slightly larger average value of ℓ_2 is used.

The equations defining the effective slit width (admittance) for different velocities and the transmission of a channel through the rotor teeth of an SDVS of this type are derived and discussed by HB.[99] The admittance, $B_{(v)}$, is defined as:

$$B(v) = n\{1-[(1+B)v_o/v-1]/Y\} \text{ for } v_o>v>v_{min} \tag{12a}$$

and

$$B(v) = n\{1+[(1-B)v_o/v-1]/Y\} \text{ for } v_{max}>v>v_o \tag{12b}$$

The transmission, T, is given by

$$T = \int_{v_{min}}^{v_{max}} I(v)B(v)dv \tag{13}$$

where I(v) is the velocity distribution of the particles incident upon the rotor.

Calibration of the SDVS axle alignment relative to the beam direction and deconvolution of the raw data curves proceeds as follows. Approximately 30 points from each of the experimental curves of Figures 15 and 16 are read into a computer where 800 intermediate points (at each half Hz) are generated using a 1-Dimensional Spline

interpolation routine. Since Figures 15 and 16 are velocity distribution measurements of the same beam, the maxima must correspond to the same linear velocity. This leads to the equation:

$$(\omega_1)(CF_1) = (\omega_3)(CF_3) \tag{14}$$

where ω_i corresponds to the maximum in the respective experimental data, CF_i is the conversion factor relating ω to linear velocity, and the subscripts 1 and 3 refer to the low- and high-resolution channels of Figure 17. The second condition necessary to solve for two unknowns comes from the geometry of the rotor. If the beam direction lies anywhere between the two channel entrances, the condition

$$r\Phi_1 + r\Phi_2 = 10(\ell_1 + \ell_2) \tag{15}$$

holds and Φ_i is related to CF_i by the geometry of the rotor.

The high-resolution data of Figure 15 are used to illustrate the deconvolution procedure. The data are scaled to an arbitrary value of 20 and plotted in Figure 19 as curve B. The quantitative effect that the transmission function for a particular channel has on the incident velocity distribution is unknown since it depends upon the form of that distribution. As a first approximation the assumption is made that the transmission of the channel has no effect. To check this assumption curve B is set equal to I(v) and substituted in numerical form into equation 13. Performing the indicated operations and scaling the results to 20 produces curve A of Figure 19. A better assumed incident distribution may now be calculated by taking a fraction of the difference of the value of curve B minus the value of curve A at each rotational frequency and adding it to the value of curve B. Iterating

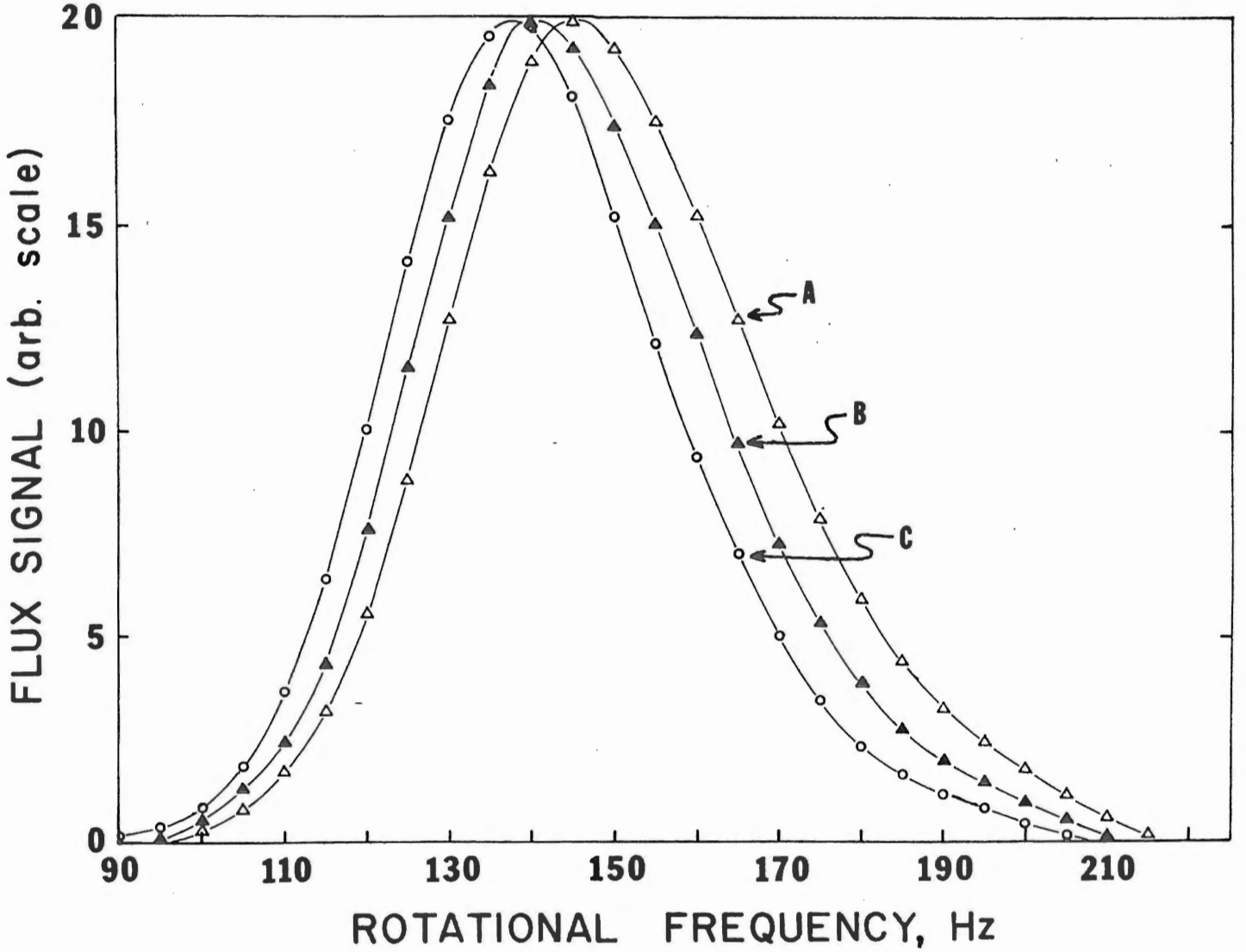

Figure 19. Curves Illustrating the Iterative Deconvolution of the SDVS Signal

through the process five times results in convergence of the incident distribution, I(v), to the values of curve C provided the above fraction is taken as one-fourth during the first iteration and three-fourths for the remainder. If equation 13 accurately describes the transmission of the rotor, then curve C is the actual velocity distribution of the particles in the beam. The calculated transmission used in the above procedure should include both the contribution of equation 13 for channel 3 plus the values of equation 13 for the sideband, channel 4. For this example, the two transmission curves do not overlap in the interval of Figure 19 and the contribution of the second term is zero.

Repeating the deconvolution for the low-resolution measurement allows the final, correct values for the two conversion factors to be calculated using equations 14 and 15. These values will be correct only as long as the detector table is not rotated. Recalculation of CF_1 and CF_2 is necessary since the deconvolution process shifts both curves towards lower velocity but the low-resolution curve shifts more than the high-resolution curve. The second effect of deconvoluting the curves is to decrease the spread of the distributions. The magnitude of the two effects are: 1) a decrease of 1.9 percent in the most probable velocity and 2) a 6.7 percent narrowing of the spread (measured as the full width at half the maximum, FWHM).

The curves resulting from the deconvolution of the distributions of Figures 15 and 16 are the two experimental curves of Figure 14. Note the excess intensity of the low-resolution curve at the low-velocity end. Since the deconvolution procedure has been performed independently on each curve, any deviation in the resulting curves is

indicative of an error in the transmission function. The most likely source of error is a small misalignment of the teeth such that a very small sideband at position three on the low-resolution side is present. A correction could be applied in the deconvolution procedure by including a third term to the total transmission if the width of that channel were measured. In any event the deviation is very small and does not affect the value of the most probable velocity at all and affects the FWHM value only slightly.

The deconvoluted velocity distributions for 298 K beams of argon at 80 torr (open circles), a "seeded" beam of 10% neon in 90% helium at 90 torr (solid triangles), and helium at 50 torr (open squares) are presented in Figure 20 scaled to an arbitrary value of 20. The actual signal levels at the maximum of each curve as measured at the detector output are: Argon = 8.64×10^{-10} amps, 10% neon - 90% helium 7.48×10^{-11} amps, and helium 3.87×10^{-11} amps. The corresponding direct incident beam strengths, measured by the flux detector with the SDVS lowered out of the beam path, are respectively 5.7×10^{-9} amps, not measured, and 7.22×10^{-10} amps.

Characterization of the Scattering Surface

The target sample consisted of a 99.9996% pure tungsten single crystal disk, 8 mm. in diameter and 3 mm. thick. After being treated according to the methods of references 98 and 75, the target was annealed at about 1300 K and a residual gas pressure of 2×10^{-8} torr, with periodic flashes to 2100 K, to remove any surface strain caused by the mechanical polishing.

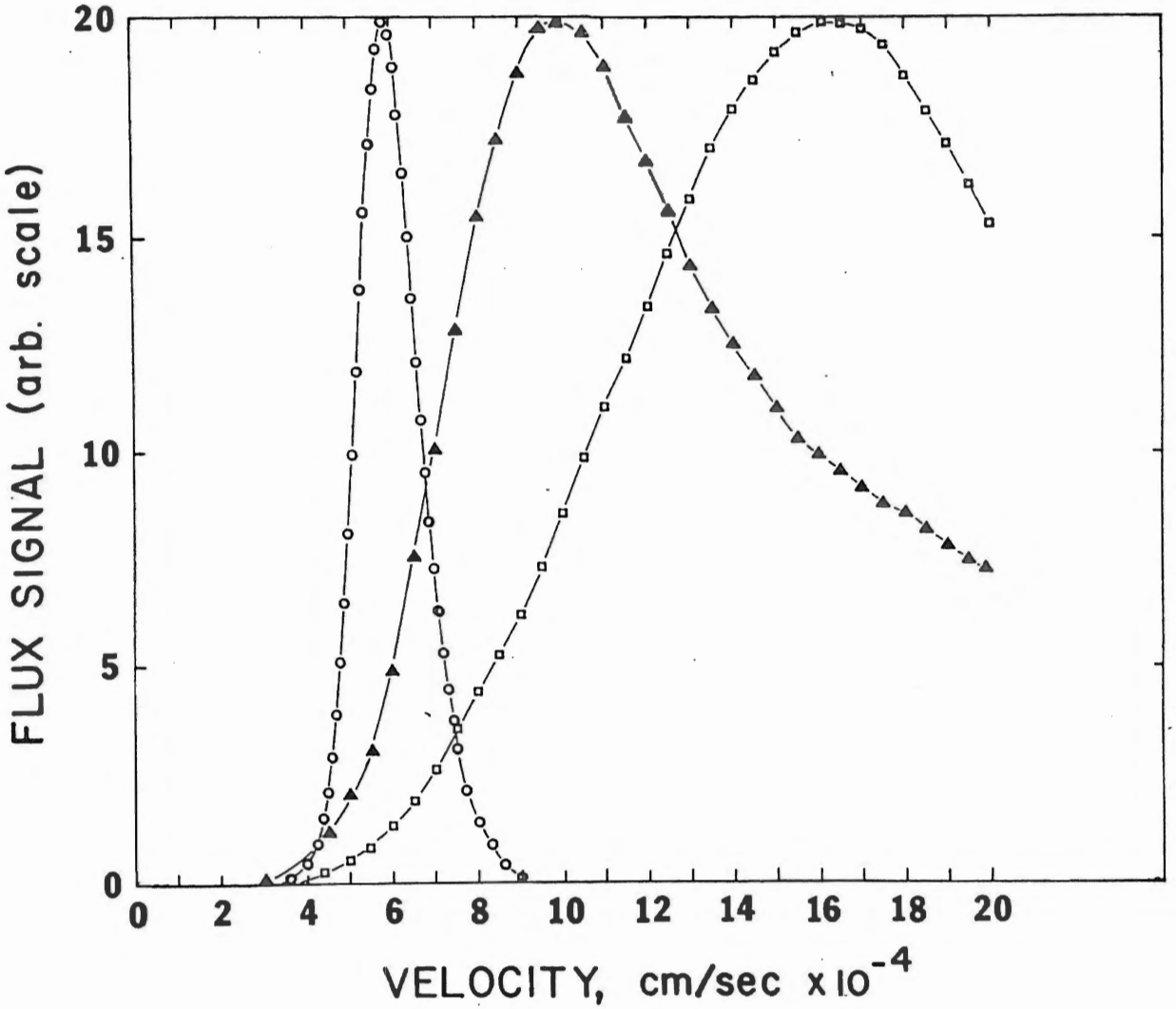

Figure 20. The Experimental Argon (o), "Seeded" 10% Neon-90% Helium (▲) and Helium (□) Beam Belocity Distributions Used in This Study to Sample the Surface

The physical character of the surface is indicated by Figures 21a, b, and c, which are photographs of the surface taken with a scanning electron microscope. The magnification is indicated by the label in the lower left-hand corner which corresponds to the width of the solid black rectangle in the lower right-hand corner. Figure 21 is a picture of the sample as obtained from the manufacturer. Figure 21b is the same tungsten sample as 21a but taken at the completion of the scattering studies reported herein and at 10 times the magnification of 21a and c. This sample has only been flashed as high as 2150 K three times and never higher. This practice of unusually mild heat treatments results in an annealing of the surface such that the scratches and surface strains of the manufactured surface grow back into the single crystal.

Part c is a different sample surface at the same magnification as part a after being heat treated at 2500 K for 27 hours. This has been a common treatment for tungsten samples being prepared for molecular beam studies. Evaporation of material from the surface and the formation of "ravines" is evident. The formation of such ravines has little effect on the shape of resulting spatial scattering distributions since the remaining flat portions of the surface are still huge on an atomic scale. Their presence may, however, appreciably attenuate the beam. Any particle entering a raving would suffer multiple collisions before emerging and no longer be a coherent part of the original beam packet. It should be noted that there is a highly preferred direction as to the formation of the ravines. Those formed horizontally (these are in the plane defined by the nozzle, surface, and detector) are much longer than the vertical ravines.

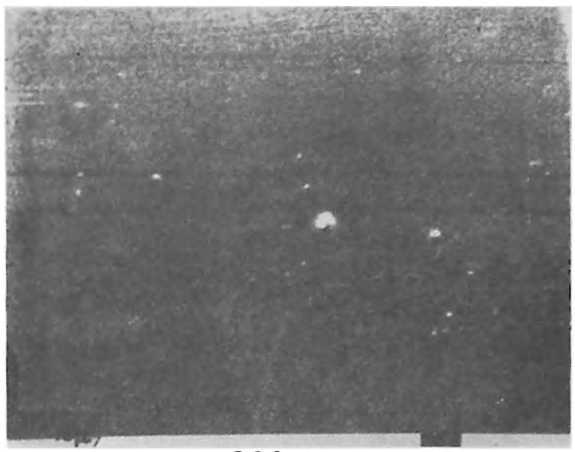

800 X

a) W(110) Surface as Purchased. Arrow Indicates the Atomic Beam Direction Used in this Work.

Atomic Beam Direction

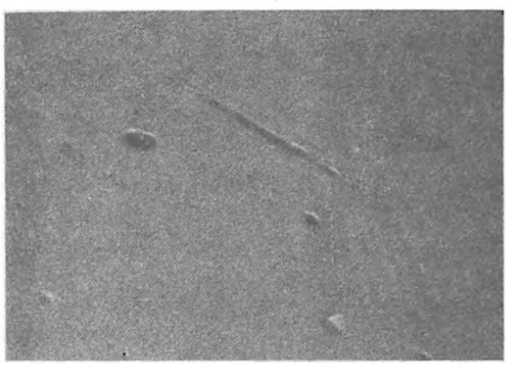

8200 X

b) W(110) Surface of Part a but at the Conclusion of this Work. Subjected Only Briefly to Surface Temperatures Up to 2150°K.

Preferred Direction of Ravine Formation

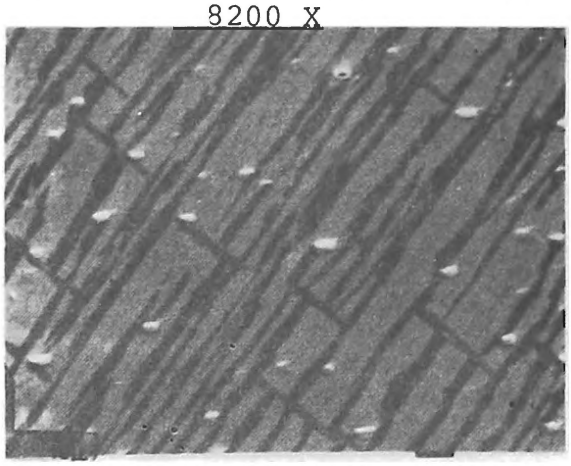

800 X

c) W(110) Surface (not the same sample as parts a and b) After Being Annealed at 2500°K for 27 Hours.

Figure 21. Scanning Electron Micrographs of the W(110) Single Crystal Surface

The scattering surface has been characterized on an atomic scale by low energy electron diffraction (LEED) and Auger electron spectroscopy (AES). The observed LEED pattern indicates a (3 x 5) structure rotated 35° with respect to the tungsten (110) surface and is shown in Figure 22. The four brightest spots, two of which are partially hidden behind the crystal holder silhouette, result from the tungsten unit mesh. The small rectangular pattern is produced by the carbide. The superposition of the LEED pattern and the crystal holder silhouette allows an accurate determination to be made of the atomic beam path relative to the superstructure orientation. For all the results of this work, the beam is traveling parallel to the long (5) side of the superstructure as indicated by the arrows in Figures 21, 22, and 23.

A (3 x 5) LEED pattern on a tungsten (110) surface has previously been reported by Stern,[102] by Bauer,[103] and by Weinberg and Merrill.[58] Stern interpreted the pattern as a dilute tungsten carbide whose chemical formula can be represented by $W_{15n}C$ where n is of the order of 2 or 4. The pattern has been interpreted as a coincidence lattice of a surface di-tungsten carbide, W_2C, by Bauer,[103] but this appears to result in a (3 x 6) LEED pattern rather than a (3 x 5).

In Figure 23a the (3 x 5) unit mesh of Stern's superstructure superimposed upon the (110) lattice is schematically illustrated. Note that one side of the tungsten unit mesh (small rhombs) is rotated 35° relative to the unit mesh of the superstructure (large rectangle of solid lines). An alternate but nonequivalent possible arrangement of a (3 x 5) structure on the (110) face is illustrated by the rectangle of dashed lines. A reasonable expectation would be that some combination of the two structures would coexist on the surface, possibly in

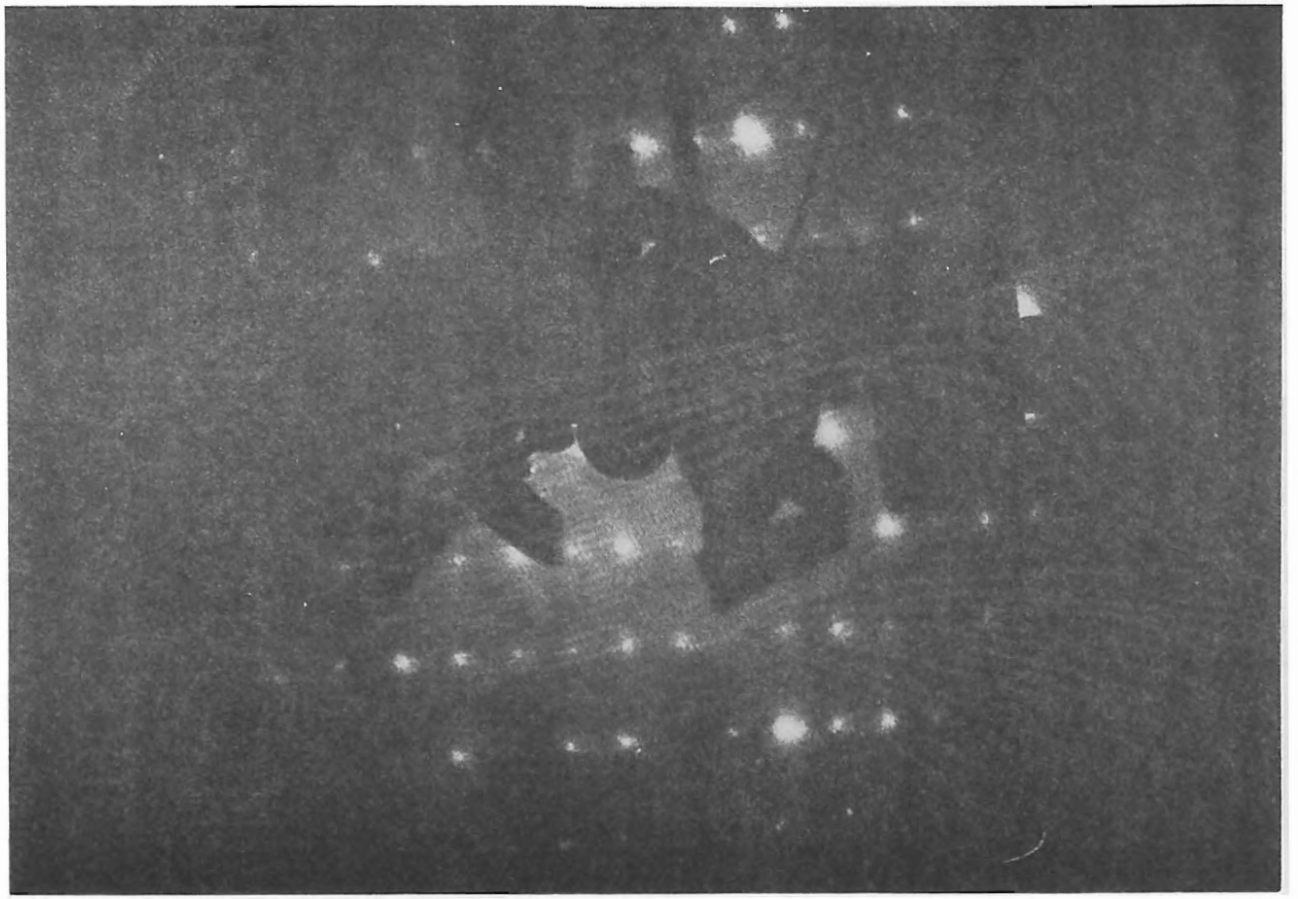

Figure 22. Low Energy Electron Diffraction Pattern From the (3 x 5) Tungsten Carbide Superstructure on the W(110) Surface Taken at 98 V

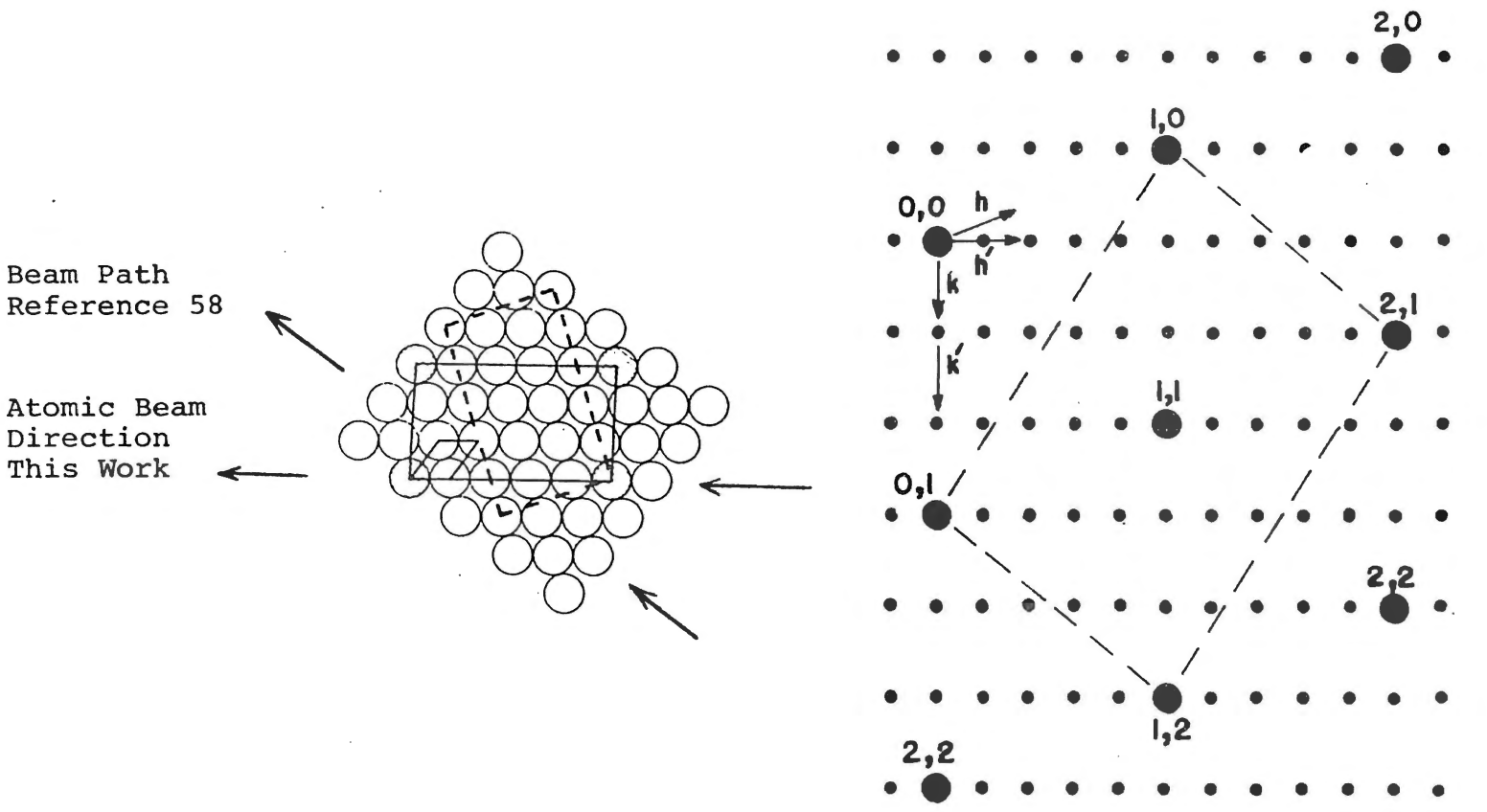

a) Schematic of the W(110) plane with the (3 x 5) carbide superstructure superimposed. The dotted line rectangle illustrates an alternate possible arrangement of a (3 x 5) superstructure.

b) Reciprocal lattices of the (3 x 5) carbide structure, h and k give the directions of the unit vectors in the tungsten reciprocal lattice and h' and k' give the directions of the unit vectors in the reciprocal lattice of the superstructure.

Figure 23. Schematic of the W(110) R-35° Carbide in a) Real Space and b) Reciprocal Lattice Space

separate small islands. In fact, the LEED results for this sample show this not to be the case. Having scanned the entire surface with LEED, only the original (solid line) (3 x 5) structure is observed except at the extreme edges where only the alternate form is seen. In the observations by Stern,[102] each of the two possible orientations were observed and a LEED pattern indicative of a superposition of the two was seen under various experimental conditions.

It is interesting to speculate as to the reason for the apparent very strong preference for one of what are, crystallographically, two identically packed rows of tungsten atoms. This same preference is shown on a microscopic level by the orientation of the (3 x 5) carbide structure and on a macroscopic level by the preferred direction of ravine formation upon evaporation. The very small inaccuracy made in cutting the (110) face, about 0.1°, produced a very shallow cut down through the surface and perpendicular to the five side of the carbide. A cut such as this probably does not produce a thermally stable end to the tungsten atom row. This same cut through the alternate row of closest tungsten atoms still enters the surface at a very shallow angle but crosses that row at an engle of 55° rather than 90°. This allows the formation of a stable "end" to the row thus limiting the ravine in that direction. It would also provide a discontinuity which might prohibit the (3 x 5) structure from forming in that direction. In any event, the atomic scattering results reported herein result from the same (3 x 5) carbide structure observed by Weinberg and Merrill[58] and may be directly compared with theirs.

Part b of Figure 23 is a reproduction of the LEED points of Figure 22. It shows several points in the reciprocal lattice of the

substrate mesh (unit vectors have the directions indicated by h and k) and nine rows of reciprocal lattice points of the superstructure (unit vectors have the directions shown by h' and k'). Since this is a reciprocal space, the short side of the small rectangular pattern corresponds to the long side of the large (3 x 5) carbide in the real space representative to 23a. The large rhombs (dotted lines) in the reciprocal space of 23b correspond
the real space of 23a. The direction of the atomic beam employed in this work is within 1° of the minus h' direction, while the plane defined by the nozzle, surface, and detector lies perpendicular to the W(110) plane. The results of Weinberg and Merrill[58] correspond to a beam path through the (0,0) and (1,1) points of the tungsten reciprocal space and with the surface tipped so that the (1,0) and (2,0) points of the reciprocal lattice of the superstructure fall within the detector path.

Auger electron spectroscopy (AES) has been used in this study in an attempt to shed some light on the chemical nature of the tungsten carbide structure. The internal structure of the carbide is not known. Stern's view[102] of the (3 x 5) R-35° surface is that of a very dilute carbide ($W_{15n}C$ where n is the number of atomic planes contained in the unit cell and may be of the order of 2 or 4) while Bauer[103] suggests W_2C and Weinberg and Merrill postulate a "WC with periodic "holes" with a periodicity of (3 x 5) which might represent stacking faults, bare tungsten atoms, or the like". Their argument for this carbon-rich structure is based on the extremely high ratio of scattered signal intensity relative to incident beam signal, in most cases in the 40 to 55 percent range; their argument is that the

stiffer carbon surface results in a much more intense in-plane scattering intensity. While this is certainly a plausible argument, it is not clear why the intensity ratios reported herein are about two orders of magnitude lower, even though it is undoubtedly the same (3 x 5) carbide structure. Alternative explanations may be proposed in terms of the obtainable base pressures of the two systems (less than 7×10^{-11} torr for theirs and 3×10^{-10} torr for ours), in terms of the detectors (d.c. mass spectrometer and a.c. ionization gauge, respectively), or in terms of the direction with which the beams pass across the structure as illustrated in Figures 22 and 23.

The conclusion of Weinberg and Merrill (WM) that the carbide exists as a carbon-rich surface is substantiated by the AES of this work. The surface plasmon peak shape indicates that the structure exists as a tungsten carbide molecule and not as loose graphite sitting on the (110) surface. A measured empirical formula of $WC_{3.2}$ represents the average over more than one atomic layer. As the layers probably progress from pure tungsten at the crystal face through layers increasingly rich in carbon, the actual surface layer may have a ratio as high as WC_{14}. This ratio would represent a (3 x 5) carbide consisting of a carbon surface with tungsten atoms at the corners of the rectangle of Figure 23a, one of the suggestions of WM. The alternative suggestions that the corners could be holes or stacking faults would lead to an atom ratio approaching one to one but with tungsten atoms in a very slight excess. If anything, the AES measurements should underestimate the number of carbon atoms. The electron beam of the Auger gun is intense enough to cause very high local surface heating at the point of the measurement and,

consequently, desorbtion of some fraction of the carbon atoms. The fact that it still measures an excess of carbon over tungsten atoms indicates a very high carbon-to-tungsten ratio for the original (3 x 5) R-35° carbide surface.

No oxides were found by the AES, probably due to the presence of the carbon. Any oxygen located on the surface combines with the carbon and produces CO and CO_2 which have appreciable vapor pressures and desorb.

The LEED and AES studies were not performed in the same apparatus as the atomic scattering experiments. They were made with the crystal undisturbed in the holder so that any material having migrated from the support to the target would have been observed. Even though these measurements were not performed in situ, there is no doubt that the surface is the same. During the course of these scattering experiments, the diffusion pump heater failed once and the pressure in the main chamber rose to the foreline pressure. Upon reevacuating the system, the helium spatial scattering distributions were the same. At one point, the crystal and its holder were removed from the system while x-ray measurements were made on the crystal. The sample and support were reintroduced to the molecular beam system after being out for one month. Evacuating the chamber to 3×10^{-10} torr and heating the target above 1200 K to remove adsorbed organic layers resulted in the same helium spatial scattering. Consequently, it is known that removing the sample from the system does not alter the carbide surface structure once it has formed. The spatial scattering experiments reported in the next section provide sufficient information to establish that the surface was in fact a carbide structure. The LEED

measurements provide the additional direct information that it is a (3 x 5) R-35° carbide and establishes which of the two possible arrangements is actually present. The LEED also establishes the direction of atomic beam travel relative to the carbide rectangle and the spacing of the two diffraction grating.

The Helium, Neon and Argon Spatial Scattering Distributions

Since it is clear that both WM and this study examined the same (3 x 5) R-35° carbide structure but with a different beam direction (azimuthal angle), the spatial scattering distributions of WM are reproduced in Figure 24 for comparison with the results of this work. The extremely high relative intensities of Figure 24 have already been discussed previously in this chapter. The variable θ corresponds to θ_r, the angle of reflection, as defined in Figure 1 of this work and the arrow at $\theta = 45°$ indicates the specular angle. The spacing of the diffraction grating, c, and the wavelength, λ, associated with the most probable velocity of the incident beam, which are used to calculate the position of the (0,0), (1,0), and (2,0) diffraction peaks, are at the top of Figure 24a. Note should be taken that the distribution indicated by solid circles corresponds to the relative intensity scale on the left side and the open squares are associated with the scale on the right side of 24a. Reservations have been expressed by Goodman[104] as to whether the three peaks of 24a are actually due to diffraction. The widths of the reflected peaks are about one-half of the incident beam width. This, plus the fact that the incident beam is derived from an effusive source with a correspondingly wide

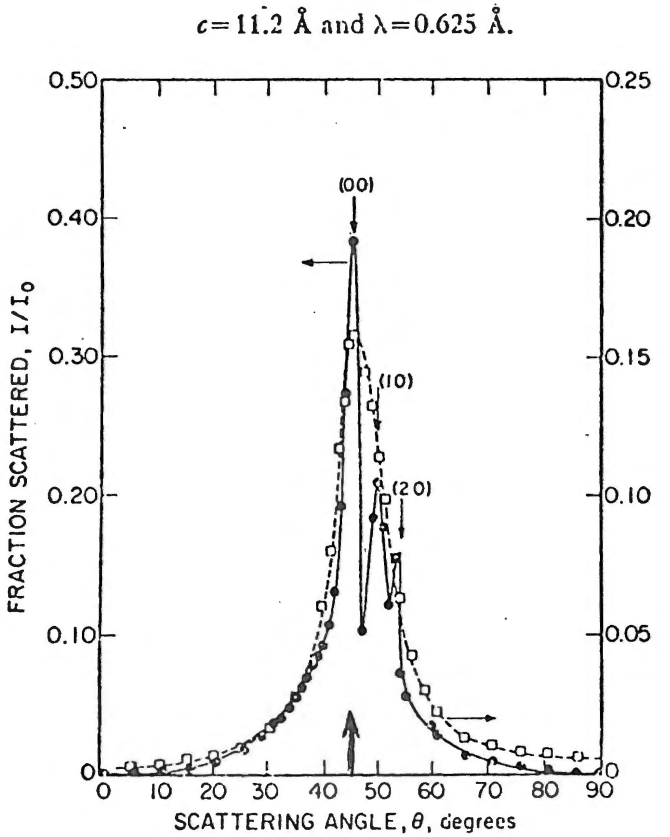

FIG. 3. He scattering from a W(110) surface. ○, He diffraction pattern from $R(3\times5)$ carbide surface with $T_s=375°K$, $T_g=295°K$, and $\theta_i=45°$. □, He scattering from clean W(110) surface with $T_s=375°K$, $T_g=295°K$, and $\theta_i=45°$.

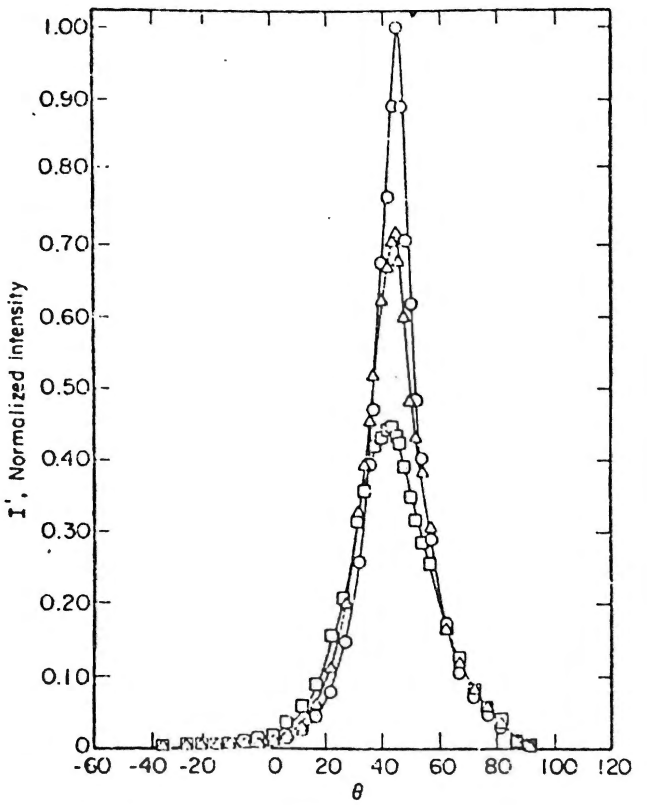

FIG. 10. Ne scattering from W(110) $R(3\times5)$ carbide surface with $T_g=295°K$ and $\theta_i=45°$. ○, $T_s=375°K$. △, $T_s=775°K$. □, $T_s=1300°K$.

Figure 24. Spatial Scattering Distributions of Weinberg and Merrill (Reference 58)

distribution of wave length, makes the resulting narrow peaks unexpected. The neon distribution of Figure 24b shows only a single peak located at or slightly below the specular angle.

The results of this study are very different from those of Figures 24a and b. Much of the difference is probably due to the different azimuthal angle. Figure 25 is the helium spatial scattering typically seen after the target had been at room temperature and a pressure of 3×10^{-10} torr overnight. Diffuse scattering of low intensity such as this is commonly observed for "dirty" surfaces where the interaction between the gas atom and surface is large. Plotted for contrast is the measured incident helium beam profile. The actual beam width is much smaller than indicated since the detector opening had an acceptance of two degrees. The sudden drop in signal intensity at 59° is an artifact of the system caused by the target-to-detector path being interrupted by the ceramic insulator supporting the target gimbal. The scale of the ordinate is the relative percent signal intensity, the signal at the detector divided by the incident beam strength times 100. The maximum of the beam profile, 1.3×10^{-9} amps at 90 torr nozzle pressure, is not plotted on the same scale. The arrow at $\theta_r = 50°$ indicates the specular angle.

The effect of heat treating the target in the range of 1200 K to 1845 K is shown in Figure 26. While the surface is maintained at 1845 K, the intense triangular distribution with a sharp specular component results. Upon cooling below the temperature at which light is emitted, the superimposed multi-lobular structure is observed. The interesting point is that the FWHM of the total distribution does not widen as the maximum intensity drops. This implies that those atoms

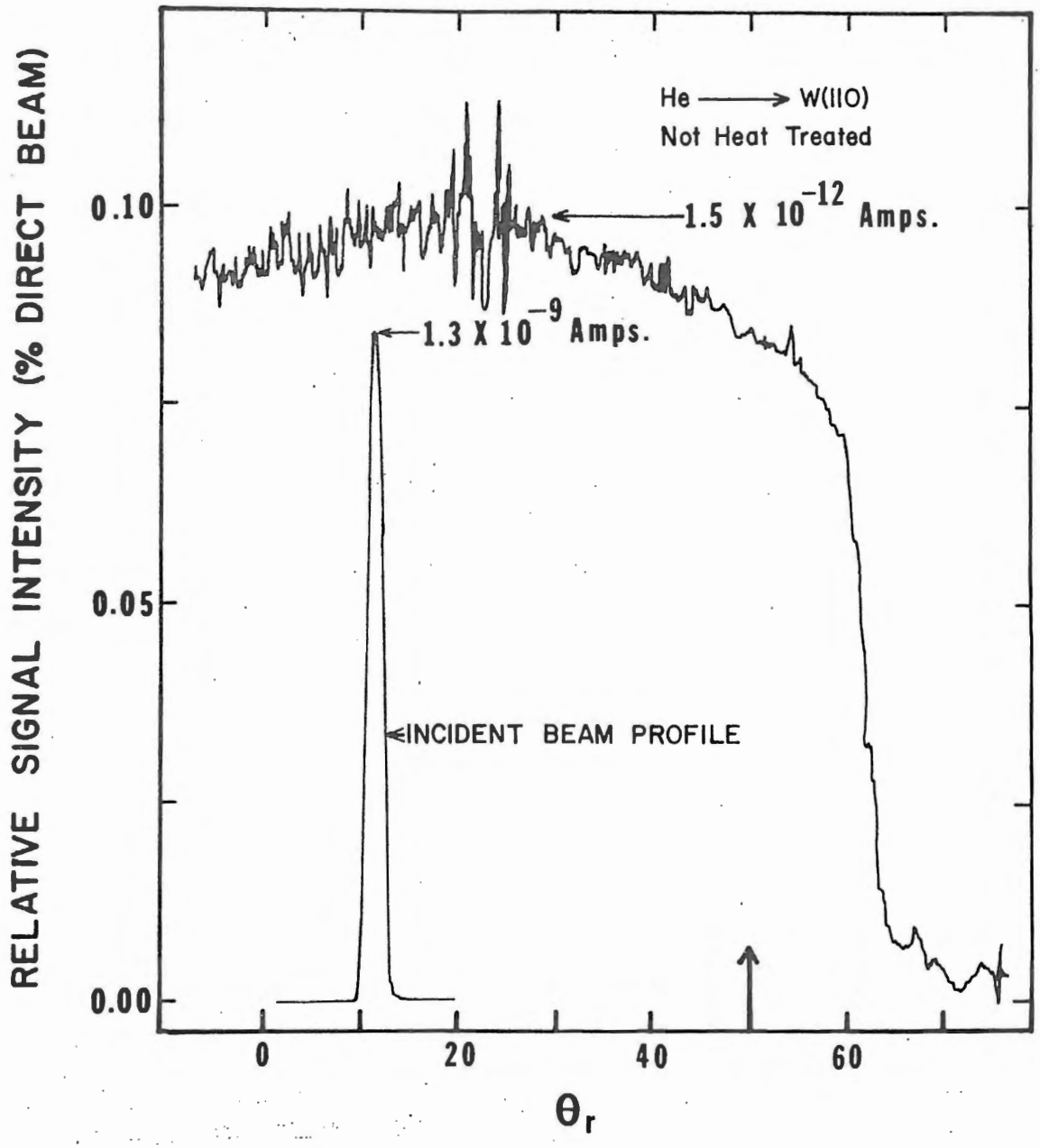

Figure 25. Incident Beam Profile (Intensity Not to Scale) and a Helium Spatial Scattering Distribution Characteristic of a "Dirty" Surface

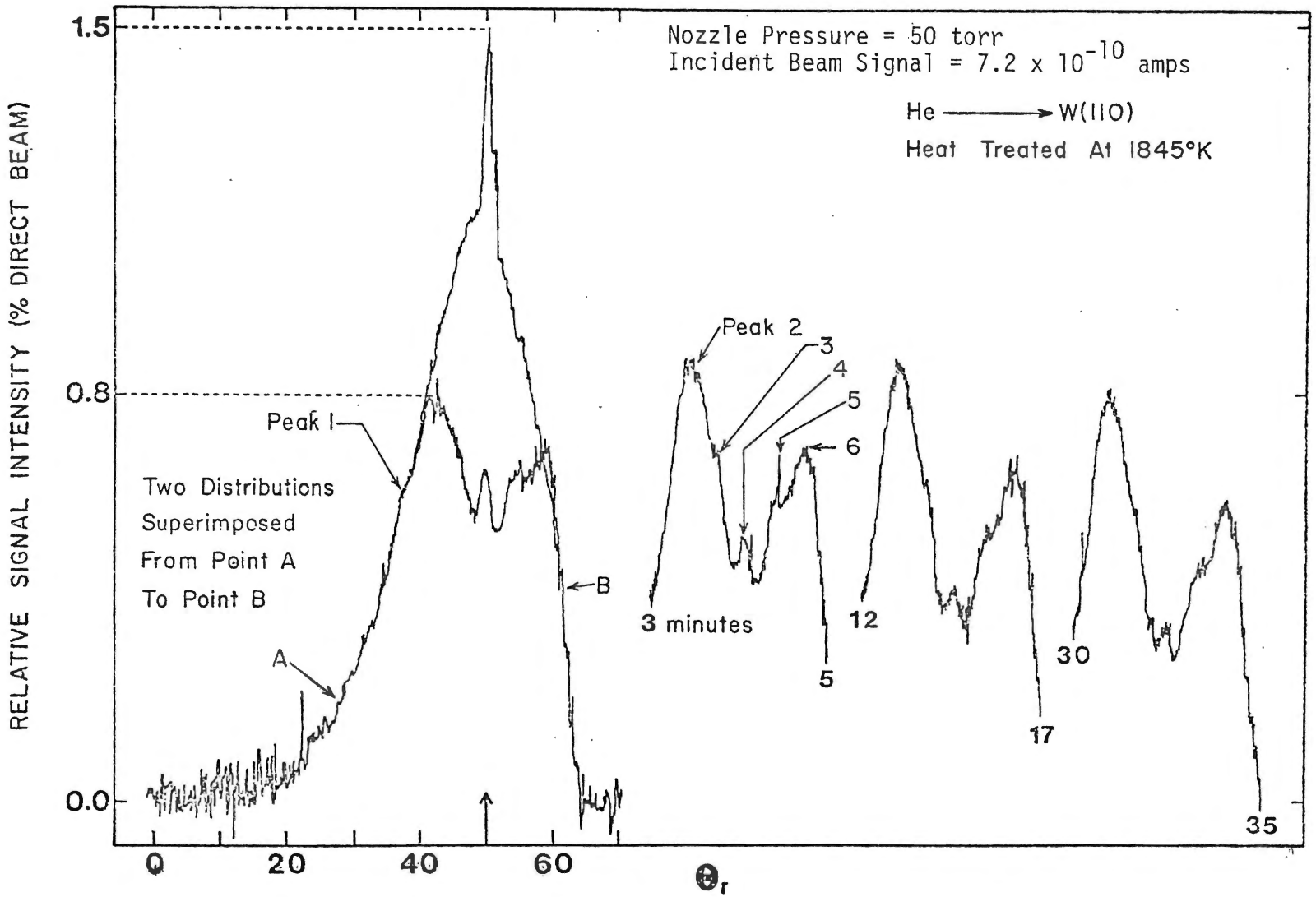

Figure 26. Superimposed Hot-Surface (T_S = 1845 K) and Room Temperature Helium Spatial Scattering Distributions

which generate the higher intensity of the hot surface scattering, are scattered out of the detector plane upon cooling. The remaining three plots in Figure 26 were taken at the time in minutes as indicated by the numbers at the ends of each plot, after the surface stopped emitting light. At least six separate peaks or shoulders are evident in one or more of the examples in Figure 26. The specular peak, number 4, remains clearly evident upon cooling, although it is sharply decreased in intensity. The two largest peaks, 2 and 6 with shoulders 3 and 5, respectively, are commonly termed "classical rainbows", Classical rainbow scattering is a classical mechanical result of the two-dimensional periodicity of the gas-solid interaction potential. A correct interpretation of the characteristic double lobes was first suggested by McClure.[105]

The formation of surface rainbows is illustrated in Figure 27. A two-dimensional scattering model with one-dimensional periodicity is used for simplicity. Figure 27 shows the trajectories of beam particles incident upon a unit cell of surface periodicity where the periodicity is represented by the wavy line. The unit cell is broken up for discussion purposes into four sections by the dotted lines. Within each section, the change in the slope of the potential curve is relatively constant. Those incident atoms which strike the potential in the first and third sections "see" a potential of quickly changing slope and, consequently, are scattered into a large solid angle. Those that strike in the second, however, meet a potential of relatively constant slope and all are scattered in a very narrow range of θ_r which is somewhat larger than the specular angle, θ_i. Since all those atoms are scattered to one detector location, a large signal intensity is

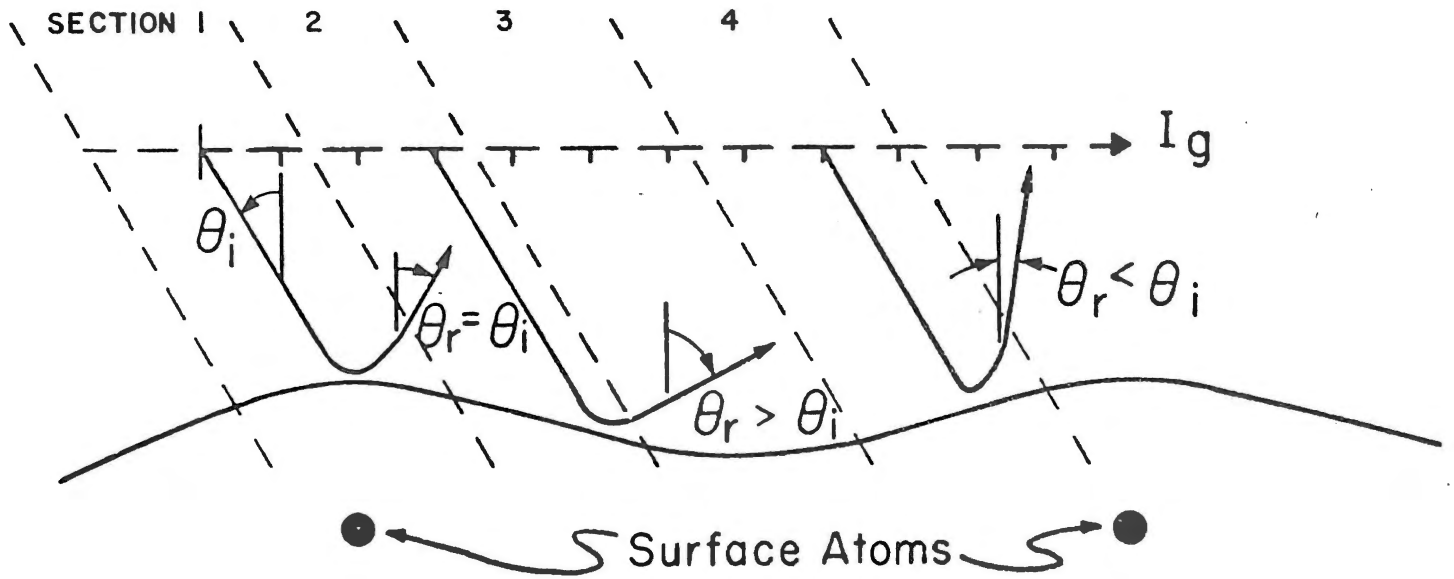

Figure 27. Illustration of the Formation of Surface Rainbows

observed. The same holds for those atoms striking in the fourth section except they all are scattered at an angle less than θ_i and produce a maximum intensity closer to the normal. On the basis of this illustration it is seen that the width of section two, as "viewed" by the incident beam is dependent upon the incidence angle. In fact, if θ_i becomes large, the incident atom cannot see the potential in section two and the scattering maximum at large θ_r should disappear. This is a somewhat oversimplified explanation. As it is now understood, classical rainbow scattering is the envelope of many quantum mechanically diffracted beams which are unresolved under the conditions that produce "classical rainbows".

The (3 x 5) R-35° W(110) carbide surface seems ideally suited for a detailed investigation of the causes and limitations of surface rainbows. The structure is extremely stable over a wide temperature range below 1850 K. It produces prominent rainbow peaks when viewed from one azimuthal angle and none when viewed from at least one other angle. The carbide surface has no overlying film which cannot be removed and would complicate the data interpretation. The majority of the systems used to date for the study of surface rainbows have been strongly ionic crystals such as lithium or sodium fluoride and each has had some water present on the surface during the molecular beam experiments. The tungsten (112) face exhibits rainbow effects,[107] but it is so active that the surface must be maintained at temperatures above 1170 K to avoid adsorption.

Figure 28 shows four helium scattering distributions from the carbide surface of this work which illustrate the time scale for the degradation of the surface by contaminants after a heat treatment.

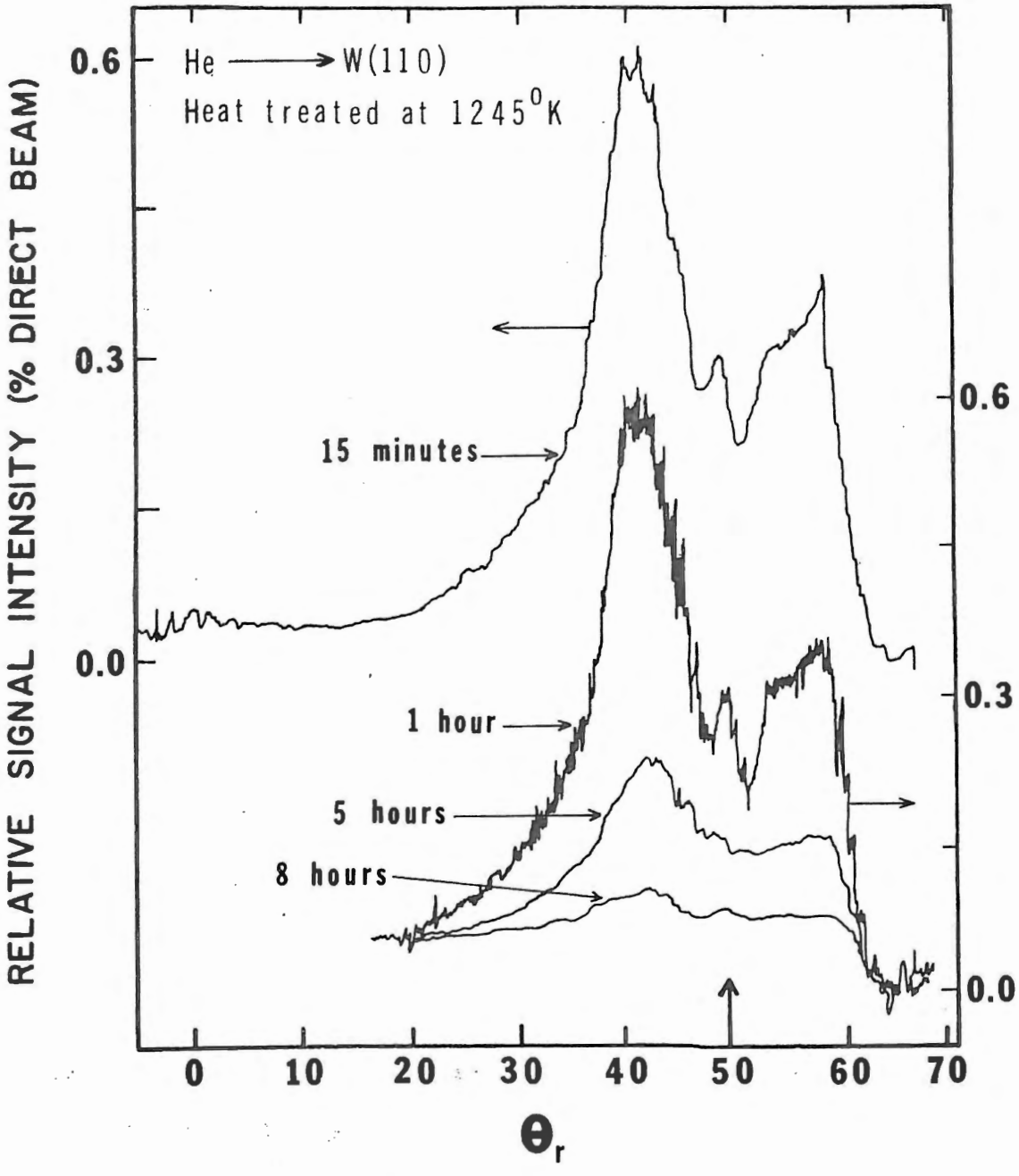

Figure 28. Time Study of Surface Degradation Due to Contaminant Adsorption

The surface was heated to 1245 K and maintained at that temperature for one hour. After cooling it to 295 K, the four plots (from top to bottom) were taken at 15 minutes, one hour, five hours, and eight hours, respectively. This time scale agrees nicely with the rule of thumb that one atomic layer of contaminant will adsorb in approximately ten hours at 1×10^{-10} torr.

Neon and argon have also been scattered from the (3 x 5) R-35° tungsten carbide surface. Figure 29 shows the neon scattering distribution for an angle of incidence of 40°. This scattering distribution was measured at T_s = 298 K after the surface had been annealed at 1600 K for one-half hour. In sharp contrast to the neon scattering results of Weinberg and Merrill[58] (Figure 24b), neon scattered in the azimuthal orientation of this work results in a very definite bimodal distribution. A relatively sharp and intense sub-specular peak is observed at 33° while a broad shoulder is located above the specular angle. No specular peak is resolved in Figure 29 although only a specular peak was observed by Weinberg and Merrill (Figure 24b). The relative percent signal intensities for the neon scattering distribution of Figure 29 and the helium scattering of Figure 26 are in close agreement (0.6% and 0.8%, respectively) indicating that approximately the same fractions for the two gases were scattered out-of-plane.

Argon scattering distributions from the (3 x 5) carbide surface were measured at angles of incidence of 30, 40, and 50 degrees and surface temperatures of 289 K, 1200 K, and then every 100 K up to 2150 K. Figure 30 shows typical results for argon. The top curve is the spatial scattering from a 298 K surface. It is emphasized again

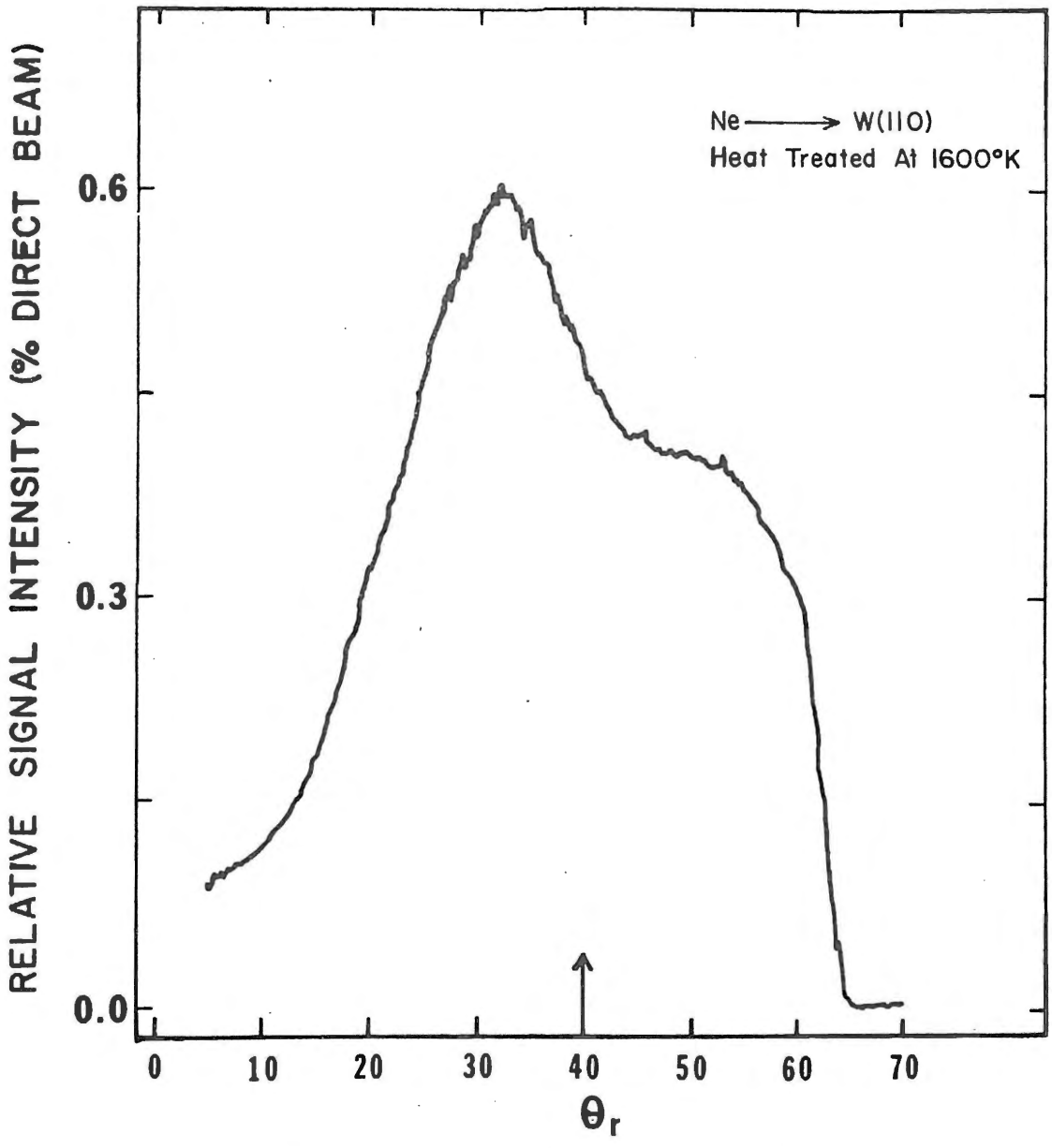

Figure 29. Neon Spatial Scattering Distribution With T_s = 298 K and T_{gas} = 298 K

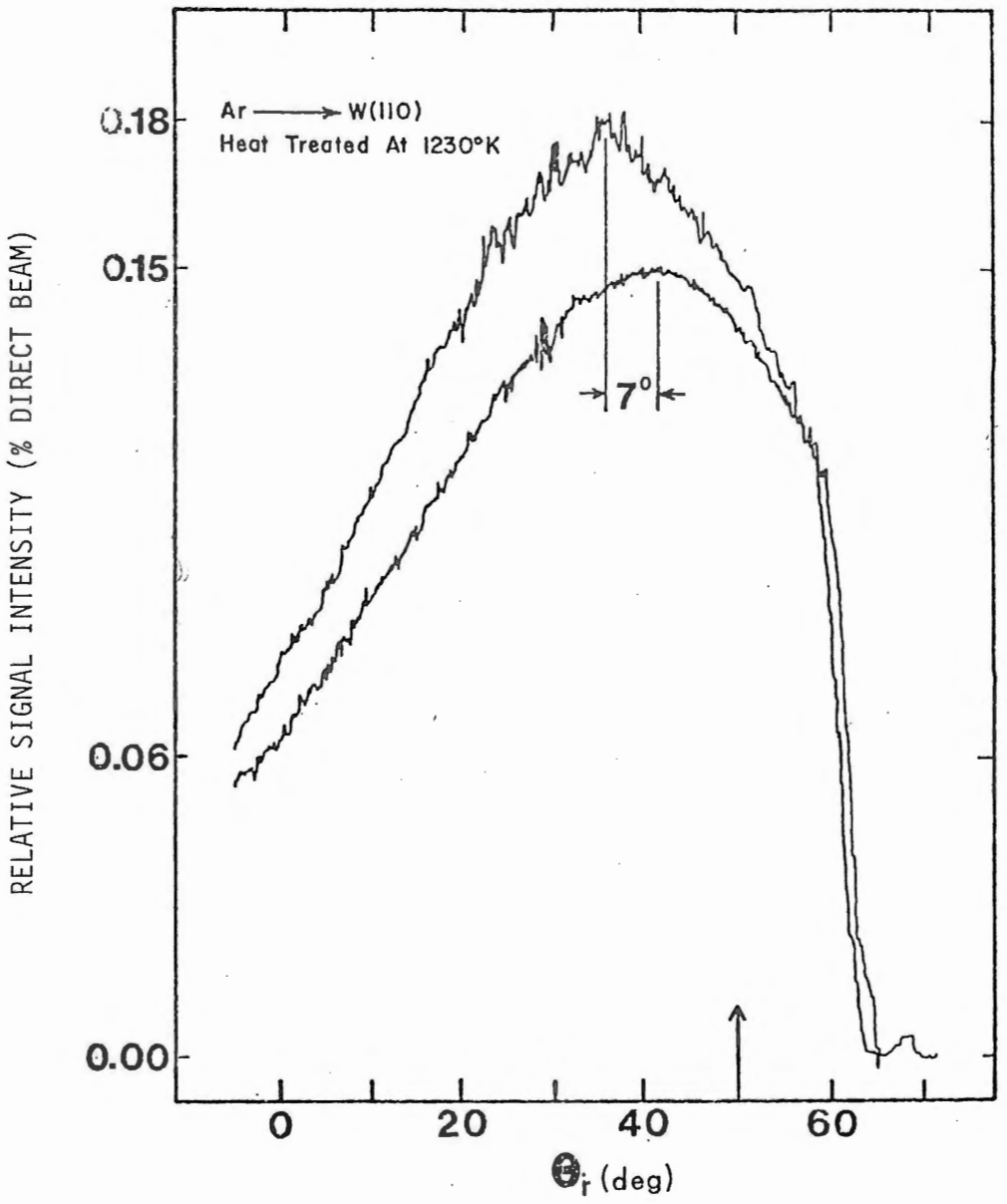

Figure 30. Argon Spatial Scattering for T_{gas} = 298 K and T_s = 1230 K (Upper Curve) and T_s = 298 K (Lower Curve)

that the drop in signal at 59° is an artifact of the crystal holder as previously explained. The maximum in each of the argon spatial scattering distributions lies below the specular angle and its separation from the specular angle is dependent upon surface temperature. For the examples of Figure 30, the lower, room temperature surface has its maximum at 8° below the specular direction while the upper curve, T_s = 1230 K, has its maximum at 15° below. As the surface temperature is increased, the thermal motion of the surface atoms increases, and the energy transmitted to the normal component of the gas atom momentum is increased, thereby resulting in a shift of the scattering distribution maxima towards the surface normal. The trend that the higher surface temperature distributions have higher intensities agrees with the argon scattering results from a clean W(110) surface.[56] This trend is commonly interpreted to mean that the argon scattering is inelastic and is in the regime dominated by trapping.[56] As the surface temperature increases, the trapping probability decreases. The opposite trend is usually observed[56] for helium and neon scattering. These two gases lie in the quasielastic as well as the inelastic regimes where trapping of the gas atoms at the surface is relatively unimportant. The explanation for this loss of specular intensity at higher surface temperatures is that the increased thermal roughening of the surface results in increased out-of-plane scattering.

The helium and neon spatial scattering distribution intensities reported in this work do not follow this commonly observed trend. They exhibit an increased specular intensity as the surface temperature increases. At least for the helium scattering this is certainly not

due to a trapping process as could be the case for argon. The most probable explanation is that helium and neon diffractive scattering of this work results from a definite two-dimensional surface structure. Many of the scattered atoms, therefore, end up in diffraction peaks which lie outside the plane of incidence. As the surface temperature is raised, the regular periodicity of the surface array is diminished and progressively less of the atoms are diffracted out-of-plane. Figure 26 best illustrates this effect. The upper hot surface scattering contains a more intense sharp specular component than the lower room temperature scattering curve. Since the two distributions are superimposed, it is seen that the added intensity near the specular angle must result from atoms which are diffracted out-of-plane when the surface is cold. The sharp specular component contains the elastically scattered atoms while the more diffuse triangular portion results from atoms which "see" the roughness of the hot surface carbide even though it is not uniform enough to produce resolved diffraction peaks. Helium scattering from a clean and smooth tungsten (110) surface contains the very sharp specular component with a very small diffuse base which results from thermal roughening.[56] This out-of-plane to in-plane intensity change is much more prevalent in scattering from this carbide surface than from either the LiF or the tungsten (112) surface. The diffraction grating spacing for the second of the two dimensions of the (3 x 5) carbide is 7.7 A° as compared to 2.84 A° for LiF and 2.74 for W(112). The carbide consequently has a stronger periodicity in the second dimension (the direction parallel to the three side of the (3 x 5) unit mesh illustrated in Figure 23a).

It has been suggested[107] that one could deduce the mean-square displacements of surface atoms directly and unambiguously from the thermal attenuation of atomic scattering using the standard Debye-Waller analysis. Studies of the thermal attenuation of elastically scattered electrons, x-rays, and neutrons have yielded valuable information about lattice dynamics. The unusual increase in specular intensity reported herein suggests that for a surface which is strongly periodic in two dimensions (where most of the elastically scattered atoms may appear as diffraction peaks out of the plane of incidence), the standard Debye-Waller analysis applied to only the specular portion of the elastically scattered atoms may yield false results. The analysis should be applied to all the elastically scattered atoms, both in- and out-of-plane, for a given incident angle and azimuthal orientation. This could most conveniently be measured by mounting the surface perpendicular to the beam (incident angles equal to zero, both in- and out-of-plane) and then rotating the surface in increments about the azimuth while scanning the detector from $\theta_r = 0°$ to $\theta_r = 90°$, at each increment. The detector movement would then be a one-quarter section through the hemisphere containing all of the diffraction peaks. The present apparatus, with minor modifications, is capable of this type measurement.

It is interesting to note the similarities between the helium and neon spatial scattering distributions which result for scattering from the tungsten (112) plane and those reported in this study for the (110) plane (Figures 26, 28, and 29). They are more similar than those observed by Weinberg and Merrill[58] from the same (3 x 5) carbide surface. Figure 31 represents the results for helium scattered from the

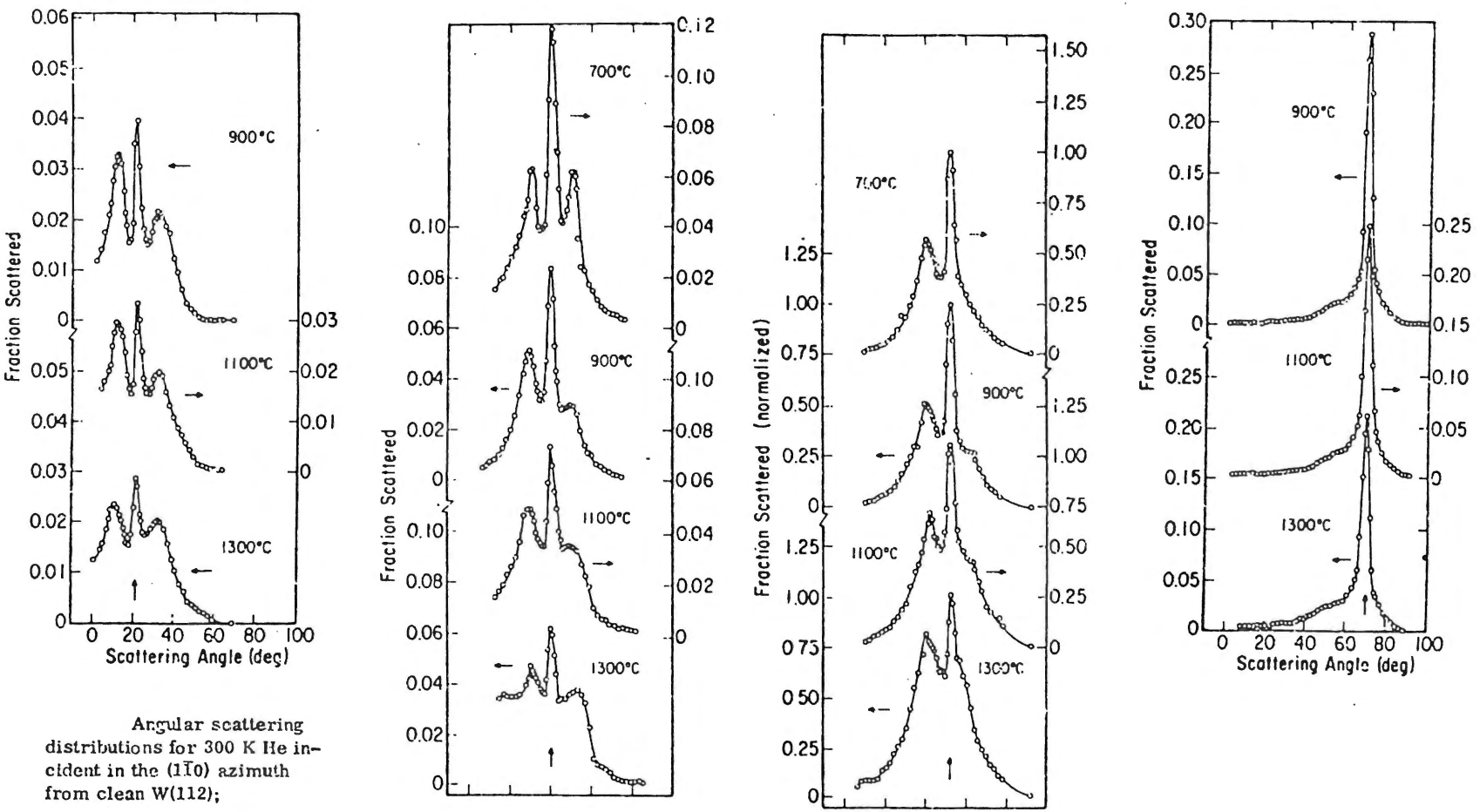

Angular scattering distributions for 300 K He incident in the $(1\bar{1}0)$ azimuth from clean W(112);

Figure 31. Helium Scattering from the W(112) Surface of Reference 107

W(112) plane.[107] A schematic diagram of the W(112) plane is shown in Figure 31e depicting the side view which illustrates the ridge-trough periodicity perpendicular to the $(1\bar{1}0)$ direction. The $W(11\bar{1})$ azimuthal direction comes out of the plane of the page. Helium spatial scattering distributions for a 300 K beam incident in the $(1\bar{1}0)$ azimuth from clean W(112) are shown in Figure 31a, b, c, and d for incident angles of 21.5°, 40°, 52.5°, and 70°, respectively. All of the scattering curves show a prominent specular peak with a peak width (FWHM) of 5° or less and with intensity increasing as the incidence angle is increased toward more grazing angles. What were originally labelled first-order diffraction features, but which are more correctly termed classical rainbow peaks, are clearly evident. They are strongest for the near-normal incidence angles, and the back-scattered peak has a greater intensity than the forward scattered (supraspecular) peak. The decrease and/or disappearance of the rainbow peaks at high incidence angle is commented upon by Stoll et al.[107] but not explained. The explanation is clearly apparent from McClure's theory[105] and has already been pointed out here. In essence, at high incidence angle, the incoming atom cannot "see" the flat "back side" (labelled section 2 in Figure 27) of a periodic bump and the supraspecular peak is diminished. At very high incidence angle, it may not encounter either of the flat portions of the periodic interaction potential (labelled sections 2 and 4 of Figure 27).

The qualitative features of the helium scattering from the W(112) surface agree with the features reported herein for scattering from the (3 x 5) R-35° tungsten carbide surface. The quantitative differences may be explained in terms of the differences in the two surfaces and

are as follows. The relative intensities are higher (one order of magnitude) for the W(112) surface. Since this surface is essentially a one-dimensional grating when viewed in the $(1\bar{1}0)$ azimuth, very little out-of-plane, diffractive scattering is to be expected. The increased specular intensity relative to the rainbow peak intensities is a result of the smaller spacing of the grating. Since the rows are closer together, a larger fraction of the surface is covered by the "tops" and "bottoms" of the periodic undulations. The larger separation of the two rainbow peaks (25° for W(112) and $\theta_i = 40°$ as compared to 18° for the carbide scattering at $\theta_i = 40°$) correlates with the smaller spacing of the W(112) grating. From Figure 27, it is seen that for a given potential contour and as the surface atoms which produce the periodicity are moved closer together, the slopes of the flat portions of the contour increase. For steeper slopes, the separation of the rainbow peaks is larger. The last difference is the retention of the three-peak curve at higher surface temperatures for the (112) surface. This is interpreted as meaning the atoms producing the periodic potential are more tightly bound in the W(112) surface. These remarkably good correlations illustrate that the features observed in this work for scattering from the carbide superstructure are a result of the periodic nature of the structure and not related to the chemical nature of the surface.

The neon scattering from the $(1\bar{1}0)$ azimuth of the W(112) surface shown in Figure 32 is also in remarkable agreement. As the beam temperature, and therefore, the incident atom energy is increased, the superspecular shoulder of the 300 K distribution is resolved into the second rainbow peak. This illustrates the possibility of a detailed

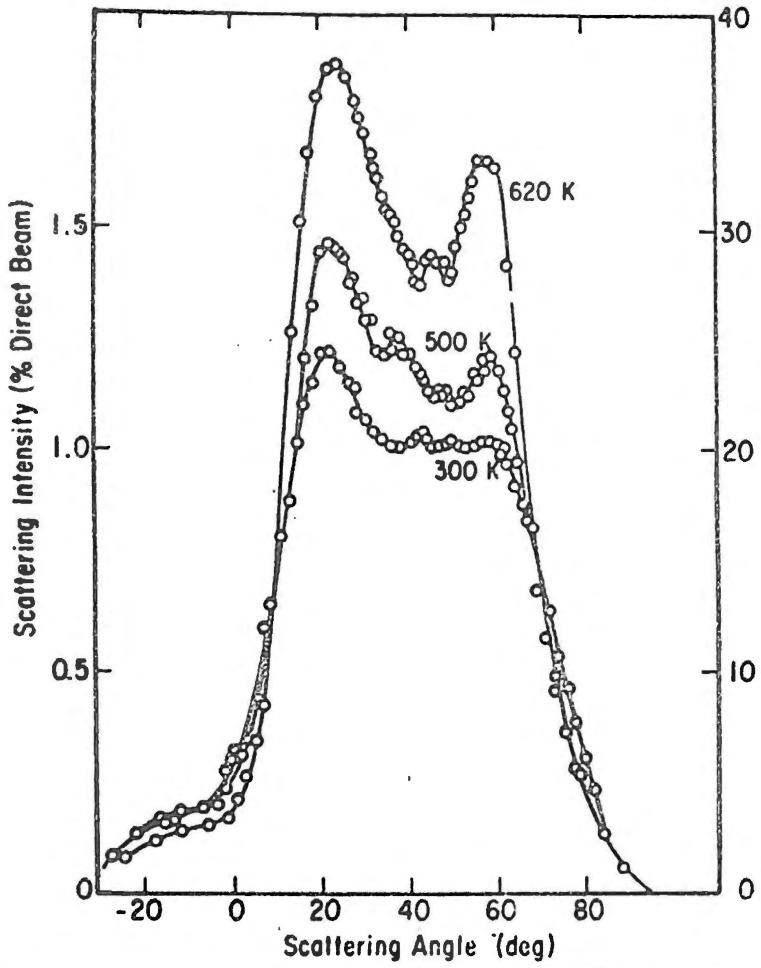

FIG. 6. Angular scattering distribution, Ne on W(112) at a temperature of 900 °C, incidence angle of 45°, and beam temperatures, ○, 20 °C; □, 230 °C; △, 350 °C.

Figure 32. Neon Scattering Results for a W(112) Surface From Reference 109

"mapping" of a contour line of the interaction potential, provided the periodicity is the correct size and the incident energy can be adequately controlled. Figure 33 shows the same effect for the neon scattering of this study where the beam is directed along the five side of the (3 x 5) R-35° (W(110) carbide superstructure. In this work a neon beam "seeded" with helium is employed for the higher-energy studies of Figures 33b and c. The average velocity and energy of a neon beam produced from a mixture of a light-atom gas and neon is greater than when the beam results from pure neon. The lighter and faster helium atoms strike the slow, heavy neon atoms and accelerate them. The average degree of acceleration depends upon the ratio of the mixture. The light atoms scatter out of the beam and do not pass through the skimmers and into the main scattering chamber. Figure 33b corresponds to a mixture ratio of 50% neon and 50% helium while 33c is a result of a 10% neon and 90% helium beam. The velocity distribution of the 10% neon beam has been reported as the solid triangles of Figure 20. The arrows in Figure 33 indicate the specular location. A partial resolution of both the specular peak and the second rainbow peak is evident. The angular separation of rainbow features of 33c is 18° while the W(112) rainbow peak separation of Figure 32 is about 37°. This trend is in agreement with helium rainbow peak separations for the two surfaces.

At annealing temperatures in excess of 1850 K, the surface atoms of the (3 x 5) carbide superstructure contain sufficient energy to cause migration and disordering of the structure. Figure 34 shows the helium scattering for a surface temperature (T_s) of 298 K, but after annealing the surface for one hour at 1875 K enough disorder has

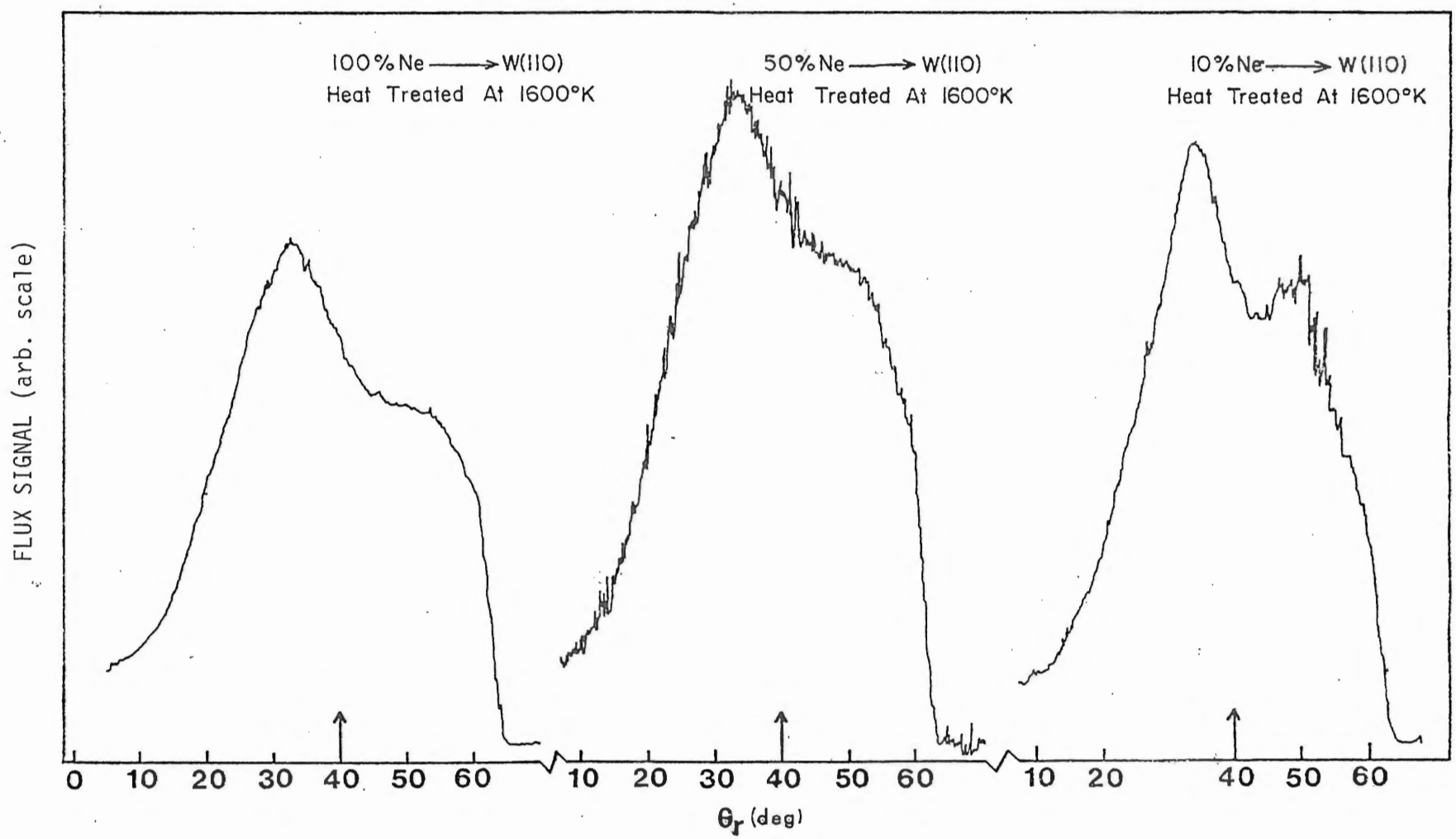

Figure 33. Neon Scattering From the (3 x 5) R-35° W(110) Carbide Surface of This Work

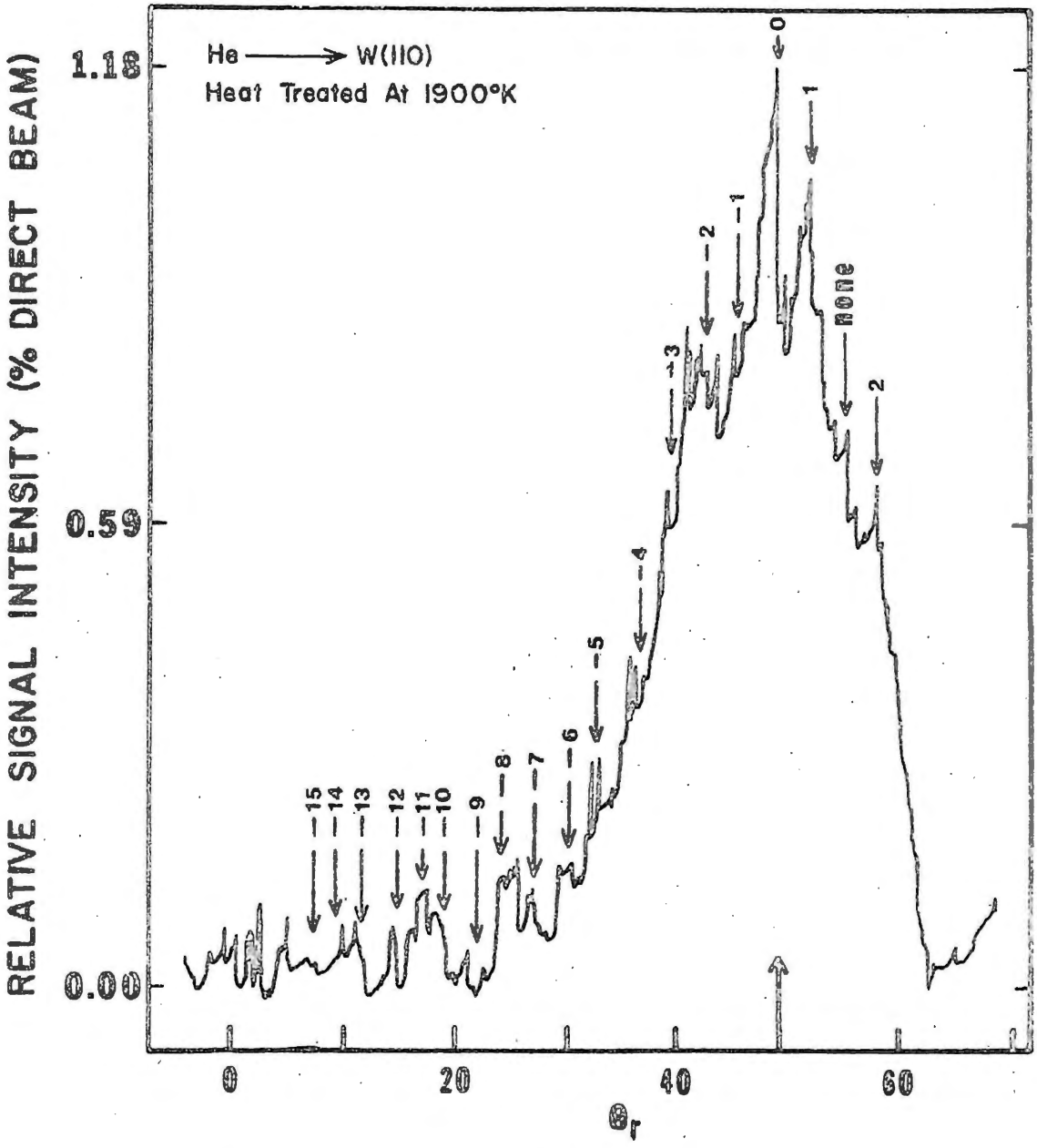

Figure 34. Helium Scattering From the Slightly Disordered (3 x 5) Carbide Superstructure

occurred to remove the bimodal rainbow character from the distribution while the individual diffraction peaks remain prevalent. The Bragg equation for diffraction from a two-dimensional array was used to correlate the diffraction results:

$$c[\sin(\theta_i + \delta) - \sin\theta_i] = n\lambda \ , \tag{16}$$

where c is the lattice constant for the diffraction grating, θ_i is the angle of incidence of the atomic beam, δ is the angular difference between the zeroth order diffraction (specular scattering maximum) and the n^{th} order maximum and λ is the wavelength of the incident beam. The wavelength is given by

$$\lambda = \frac{h}{p} = \frac{h}{mv} = 0.608 \text{ Å} \tag{17}$$

where h is Planck's constant, m is the helium gas atom mass, and v is the most probable velocity as determined from the helium velocity distribution of Figure 20. It is pointed out that while the beam source is a nozzle source operating at a Mach number of 5 with a correspondingly narrow velocity distribution, the velocity distribution is far from monoenergetic. The width of the velocity distribution results in a considerable spread in the distribution of helium wavelength. Calculating wavelengths for the velocities at the half-maximum intensities of the helium velocity distribution of Figure 20 results in $\lambda = 0.978$ Å and $\lambda = 0.416$ Å. Goodman[104] has recently examined the effect upon diffraction studies of a spread in wavelength. Diffraction orders from n = +2 to n = -15 are indicated by arrows in Figure 34. It is interesting that the relative intensities of the $(\bar{2}0)$ and (20) peaks which are the maxima of the rainbow distribution remain

at the same level as when rainbow scattering is observed. The diffuse portion which underlies the (10), (00), and ($\bar{1}$0) diffraction peaks has increased, thereby filling the valley of the rainbow curve. The measurement of Figure 34 illustrates that a somewhat greater long-range periodicity is required for rainbow scattering than is required for simple diffraction. Small and sharp fine structure is observable immediately adjacent to many of the indicated diffraction peaks. This type fine structure is caused by presently known mechanisms such as "bound-state resonances" or "surface resonances".[108] Some caution is necessary in applying much faith in the peaks labelled n = -3 through -15. While it is evident that for each position for which a diffraction peak is predicted by equation 16 some feature exists, it is not true that each such feature is stable and completely reproducible. If the detector is positioned on one angle, θ_r, and the signal level recorded, that level will change by an amount roughly equivalent to the feature height. One would normally term this a signal-to-noise ratio of one, but in this case the term noise does not refer to background electronic noise. The variation is actually a fluctuation in scattered signal flux caused by the thermal motion of the surface atoms. Cooling the surface would decrease the thermal motion and allow a much better resolution of these features. Note should be taken that one peak is observed both in Figure 34 and sometimes in the rainbow scattering which is not labelled by the Bragg equation. It lies between the (20) and (10) peaks and may be the result of a process such as "surface resonance". Quickly flashing (~30 seconds) the slightly disordered surface of Figure 34 to 1310 K results in a regeneration of the bimodal rainbow scattering

distribution in Figure 35. The main diffraction peaks labelled (20), (10), (00), $(\bar{1}0)$, and $(\bar{2}0)$ and indicated by arrows remain clearly evident.

To further demonstrate that the results reported in this work are a direct result of scattering from the carbide superstructure and not from features of the underlying tungsten surface, the surface was chemically cleaned of carbon in situ. The target was annealed at a surface temperature of 1255 K for 1.5 hours while a partial pressure of 3×10^{-8} torr of oxygen was maintained in the scattering chamber. At this elevated temperature, any carbon present on the surface reacts with the oxygen and then desorbs as CO and/or CO_2. After cooling the surface to 298 K and reevacuating the scattering chamber to 6×10^{-10} torr, the helium spatial scattering distribution of Figure 36 was recorded. The only structure present in the distribution is a very sharp specular peak characteristic of helium scattering from a clean and smooth tungsten (110) surface. Quickly flashing the target to 1300 K does not regenerate the bimodal or diffraction features. Annealing it at T_s = 1600 K for one hour does regenerate the rainbow distribution pictured in Figure 35. This indicates that the carbon had been removed by the oxygen, and it then requires an appreciable length of time for additional carbon atoms to migrate from the bulk to the surface. The rainbow peaks reappear as the (3 x 5) R-35° tungsten carbide superstructure is recreated.

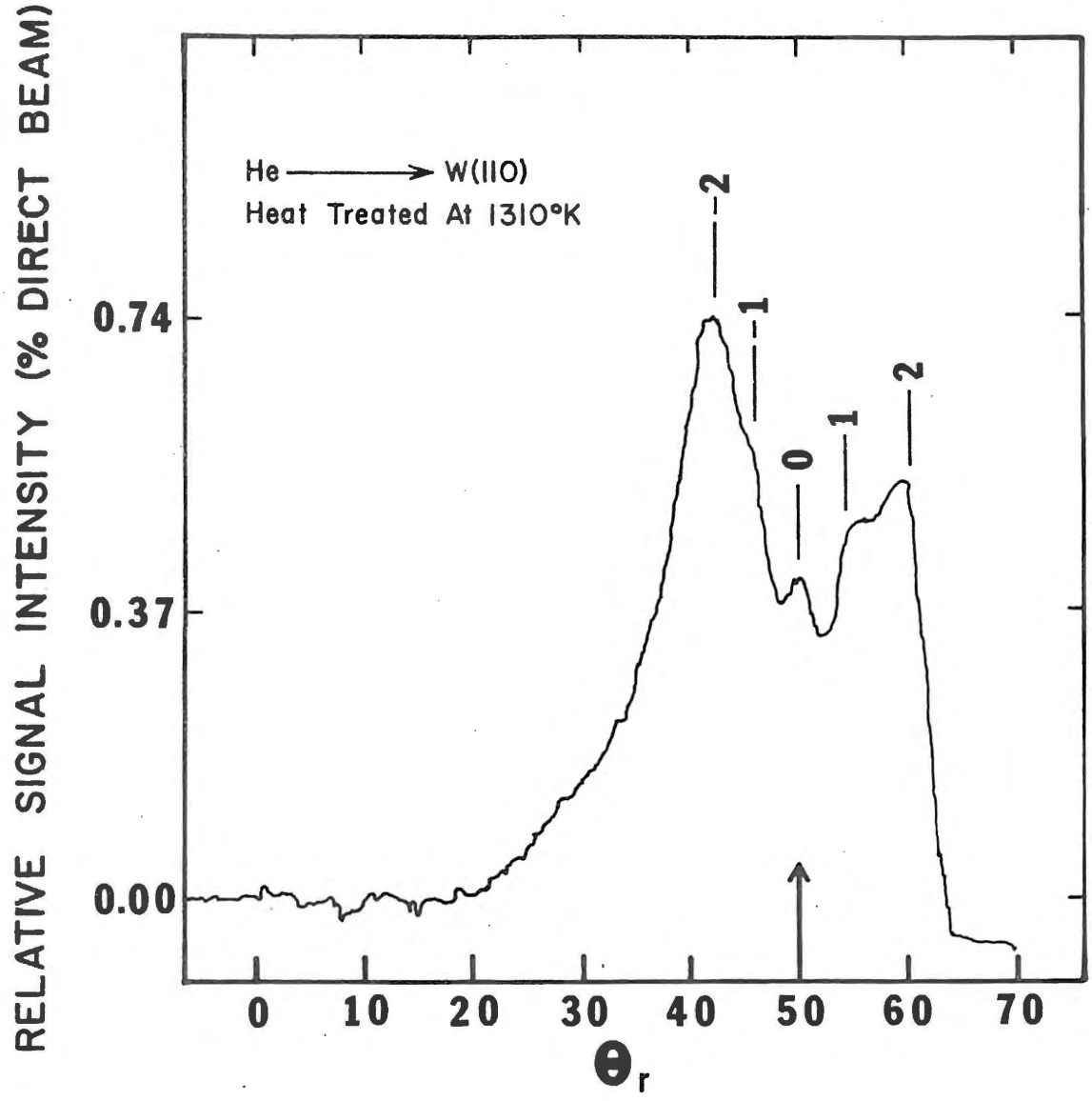

Figure 35. Helium Spatial Scattering From the Carbide Superstructure

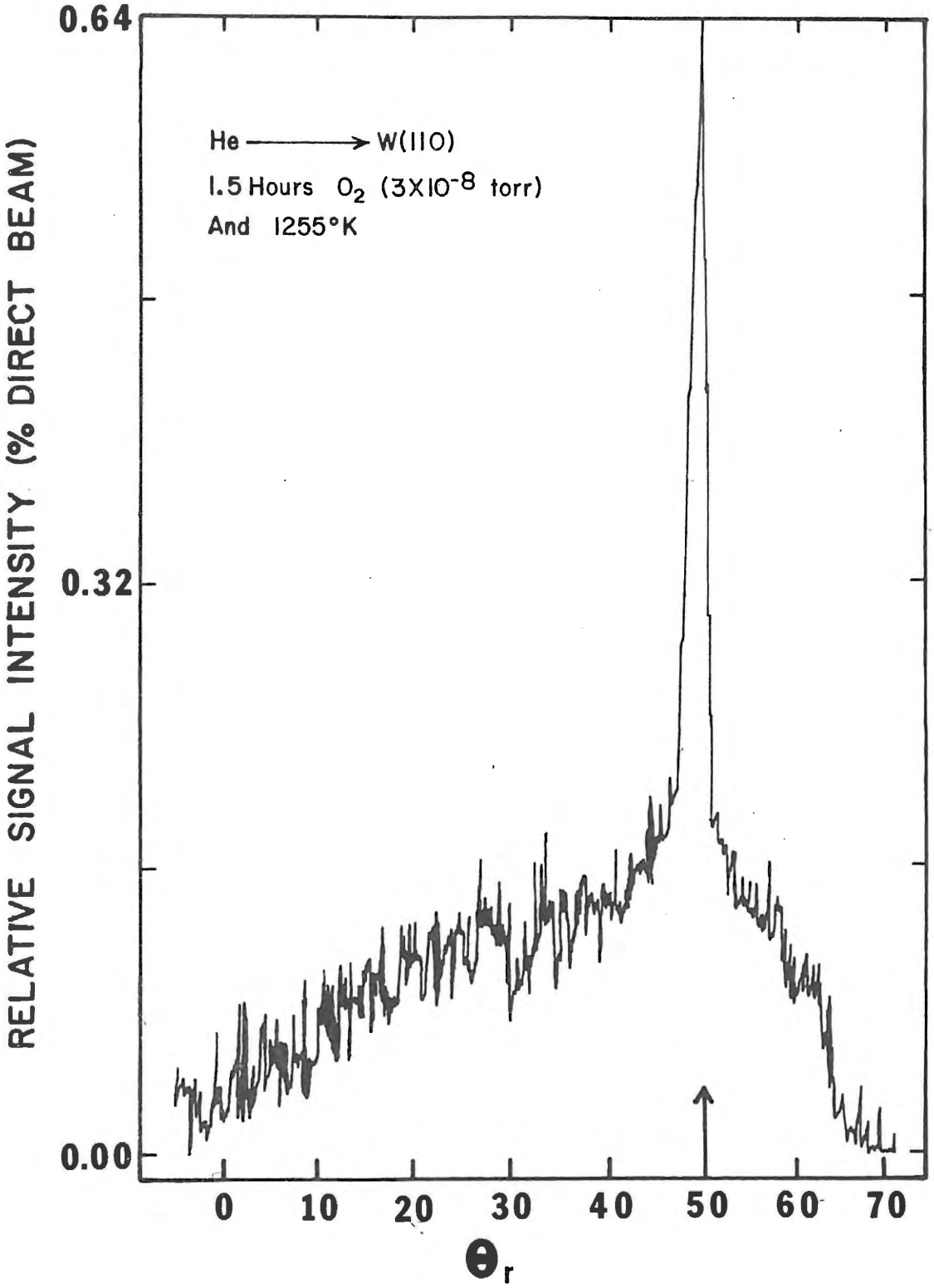

Figure 36. Helium Scattering From the Oxygen Cleaned W(110) Surface

SELECTED BIBLIOGRAPHY

1. Kundt, A. and Warburg, E., Pogg. Ann. Phys., 155, 337 (1875).

2. Maxwell, J. C., The Scientific Papers of James Clark Maxwell, ed. W. D. Niven, Cambridge Press, 1890, Vol. 1, p. 391.

3. Kennard, E. H., Kinetic Theory of Gases, McGraw-Hill, N. Y., 1938, p. 311.

4. Maxwell, J. C., The Scientific Papers of James Clark Maxwell, ed. W. D. Niven, Cambridge Press, 1890, Vol. 2, p. 706.

5. Smoluchowski, M. S., Phil. Mag., 46, 192 (1898).

6. Smoluchowski, M. S., Sber. Akad. Wiss. Wien, 107, 304 (1898); 108 5 (1899).

7. Knudsen, M., Ann. Physik, 34, 593 (1911).

8. Blodgett, K. B. and Langmuir, I., Phys. Rev., 40, 78 (1932).

9. Raff, L. M., Lorenzen, J., and McCoy, B. C., J. Chem. Phys., 46, 4265 (1967).

10. Jackson, J. M., Proc. Camb. Phil. Soc., 28, 136 (1932).

11. Hurlburt, F. C., Phys. Fluids, 7, 904 (1964).

12. Wachman, H. Y., J. Chem. Phys., 42, 1850 (1965).

13. Thomas, L. B., Fundamentals of Gas-Surface Interactions, ed. H. Saltsburg, J. N. Smith, Jr., and M. Rogers, Academic Press, N. Y., 1967, p. 346.

14. Kouptsidis, J. and Menzel, D., Ber. Bunsenges. Phys. Chem., 71, 720 (1967); 74, 512 (1970).

15. Thomas, L. B. and Golike, R. C., J. Chem. Phys., 22, 300 (1954).

16. Lees, L. and Liu, C., Phys. Fluids, 5, 1137 (1962).

17. Harris, R. E., J. Chem. Phys., 46, 3217 (1967).

18. Willis, D. R., Phys. Fluids, 8, 1908 (1965).

19. Su, C. L. and Willis, D. R., Phys. Fluids, 11, 2131 (1968).

20. Smoluchowski, M. S., Sber. Akad. Wiss. Wien, 107, 304 (1898); ibid., 108, 5 (1899); Kennard, E. H., Kinetic Theory of Gases, McGraw-Hill, N. Y., 1938.

21. Bybbs, A. and Springer, G. S., Phys. Fluids, 8, 1946 (1965).

22. Sheldon, D. B. and Springer, G. S., Phys. Fluids, 11, 1312 (1968).

23. Thomas, L. B. and Schofield, E. B., J. Chem. Phys., 23, 861 (1955).

24. Roach, D. V. and Thomas, L. B., J. Chem. Phys., 59, 3395 (1973).

25. Thomas, L. B., Proc. Intern. Symp. Rarefied Gas Dyn., Academic Press, Suppl. 4, 1, 155 (1967).

26. Hurlburt, F. C., Proc. Intern. Symp. Rarefied Gas Dyn., Adademic Press, Suppl. 4, 1, 1 (1967).

27. Thomas, L. B., Krueger, C. L., and Harris, R. E., Proc. Intern. Symp. Rarefied Gas Dyn., Academic Press, Suppl. 5, 2, 1015 (1969).

28. Wachman, H. Y., J. Chem. Phys., 45, 1532 (1966).

29. Roberts, J. K., Proc. Roy. Soc., A129, 146 (1930); A142, 518 (1933).

30. Jackson, J. M. and Mott, N. F., Proc. Roy. Soc., A137, 703 (1932).

31. Jackson, J. M. and Howarth, A., Proc. Roy. Soc., A142, 447 (1933).

32. Devonshire, A. F., Proc. Roy. Soc., A158, 269 (1937).

33. Landau, L., Phys. Zeit. der Sowjetunion, 5, 489 (1935).

34. Goodman, F. O., J. Phys. Chem. Solids, 24, 1451 (1963).

35. Caberera, N., Disc. Faraday Soc., 28, 16 (1959).

36. Zwanzig, R. W., J. Chem. Phys., 32, 1173 (1960).

37. Goodman, F. O., J. Phys. Chem. Solids, 23, 1269 (1962).

38. Leonas, V. B., Zh. Prikl. Mekhan. i Tekhn. Fiz., 6, 124 (1963) (English Transl.: NASA TT f-265).

39. McCarroll, B. and Ehrlich, G., J. Chem. Phys., 38, 523 (1963).

40. Trilling, L., Proc. Intern. Symp. Rarefied Gas Dyn., Academic Press, Suppl. 4, 1, 139 (1967).

41. Chambers, C. M. and Kinzer, E. T., Surface Sci., 4, 33 (1966).

42. Knauer, F. and Stern, O., Z. Physik, 53, 779 (1929).

43. Ellett, A., Olson, H. F., and Zahl, H. A., Phys. Rev., 34, 493 (1929).

44. Estermann, I. and Stern, O., Z. Physik, 61, 95 (1930).

45. Estermann, I., Frisch, R., and Stern, O., Z. Phys., 73, 348 (1931).

46. Crews, J. C., J. Chem. Phys., 37, 2004 (1962); Fundamentals of Gas-Surface Interactions, ed. H. Saltsburg, J. N. Smith, Jr., and M. Rogers, Academic Press, N. Y., 1967, p. 480.

47. Fisher, S. and Bledsoe, J. R., J. Vac. Sci. Tech., 9, 814 (1972).

48. Williams, B. R., J. Chem. Phys., 55, 3220 (1971).

49. O'Keefe, D. R., Palmer, R. L., Saltsburg, H., and Smith, J. N., Jr., J. Chem. Phys., 49, 5194 (1968); J. Chem. Phys., 52, 4447 (1970); Surface Sci., 20, 27 (1970).

50. Bayh, W. and Pflung, H., Z. Angew. Phys., 25, 358 (1968).

51. Beder, E. C., Advances in Atomic and Molecular Physics, 3, 205 (1967).

52. Oman, R. A., J. Chem. Phys., 48, 3919 (1968).

53. McClure, J. D., J. Chem. Phys., 51, 1687 (1969); 52, 2712 (1970).

54. Stoll, A. G., Smith, D. L., and Merrill, R. P., J. Chem. Phys., 54, 163 (1971).

55. Palmer, R. L., O'Keefe, D. R., Saltsburg, H., and Smith, J. N., Jr., J. Vac. Sci. Tech., 7, 91 (1970).

56. Weinberg, W. H. and Merrill, R. P., J. Chem. Phys., 56, 2881 (1972).

57. Weinberg, W. H. and Merrill, R. P., Phys. Rev. Lett., 25, 1198 (1972).

58. Weinberg, W. H. and Merrill, R. P., J. Chem. Phys., 56, 2893 (1972).

59. Tendulkar, D. V. and Stickney, R. E., Surface Sci., 27, 516 (1971).

60. Smith, J. N., Jr., Surface Sci., 34, 613 (1973).

61. Roberts, R. W., Brit. J. App. Phys., 14, 537 (1963).

62. Smith, J. N., Jr. and Saltsburg, H., J. Chem. Phys., 40, 3585 (1964).

63. Smith, J. N., Jr. and Saltsburg, H., J. Chem. Phys., 45, 2175 (1966).

64. Smith, J. N., Jr. and Saltsburg, H., Proc. Intern. Symp. Rarefied Gas Dyn., Academic Press, Suppl. 3, 2, 491 (1966).

65. Smith, J. N., Jr. and Saltsburg, H., Fundamentals of Gas-Surface Interactions, ed. H. Saltsburg, J. N. Smith, Jr., and M. Rogers, Academic Press, N. Y., 1967, p. 370.

66. Saltsburg, H., Smith, J. N., Jr., and Palmer, R. L., Proc. Intern. Symp. Rarefied Gas Dyn., Academic Press, Suppl. 4, 1, 223 (1967).

67. Saltsburg, H., Smith, J. N., Jr., and Palmer, R. L., J. Chem. Phys., 49, 1287 (1968).

68. Saltsburg, H., Smith, J. N., Jr., and Palmer, R. L., Bull. Am. Phys. Soc., Series II, 13, 906 (1968).

69. Saltsburg, H., Smith, J. N., Jr., and Palmer, R. L., Proc. Intern. Symp. Rarefied Gas Dyn., Academic Press, Suppl. 5, 2, 1141 (1969).

70. Palmer, R. L., Saltsburg, H., and Smith, J. N., Jr., J. Chem. Phys., 50, 4661 (1969).

71. Palmer, R. L., O'Keefe, D. R., Saltsburg, H., and Smith, J. N., Jr., J. Chem. Phys., 53, 1666 (1970).

72. Belous, M. V. and Wayman, C. M., J. Appl. Phys., 38, 5119 (1967).

73. Sau, R. and Merrill, R. P., Surface Sci., 34, 268 (1973).

74. Bishara, M. N. and Fisher, S. S., J. Chem. Phys., 52, 5661 (1970).

75. Yamamato, S. and Stickney, R. E., J. Chem. Phys., 53, 1594 (1970).

76. Sasaki, N., Taku, K., and Mitani, K., Mem. Coll. Sci. Univ. Kyoto, A25, 75 (1949).

77. Stickney, R. E. and Hurlburt, F. C., Proc. Intern. Symp. Rarefied Gas Dyn., Academic Press, Suppl. 2, 1, 454 (1963).

78. Kostoff, R. N., Anderson, J. B., and Fenn, J. B., Fundamentals of Gas-Surface Interactions, ed. H. Saltsburg, J. N. Smith, Jr., and M. Rogers, Academic Press, N. Y., 1967, p. 512.

79. Ramsey, N. F., Molecular Beams, Oxford University Press, London, 1956, Chapter 14.

80. Zahl, H. A., Phys. Rev., 36, 893 (1930).

81. Ellett, A. and Cohen, V. W., Phys. Rev., 52, 509 (1937).

82. Marcus, P. M. and McFee, J. H., Recent Research in Molecular Beams, ed. I. Estermann, Academic Press, N. Y., 1959, p. 43.

83. Taylor, J. B., Z. Physik, 57, 242 (1929).

84. Langmuir, E. and Kingdon, K. H., Proc. Roy. Soc., A107, 61 (1925).

85. Hinchen, J. J. and Foley, W. N., Proc. Intern. Symp. Rarefied Gas Dyn., Academic Press, Suppl. 3, 2, 505 (1966).

86. Fite, W. L. and Brackman, R. T., Phys. Rev., 112, 1141 (1958).

87. Yamamoto, S. and Stickney, R. E., J. Chem. Phys., 47, 1091 (1967).

88. Smith, J. N., Jr., J. Chem. Phys., 40, 2050 (1965).

89. Smith, J. N., Jr. General Atomics Report. No. GA-4665 (Nov. 5, 1963).

90. Smith, J. N., Jr. and Fite, W. L., Proc. Intern. Symp. Rarefied Gas Dyn., Academic Press, Suppl. 1, 2, 430 (1963).

91. Moran, J. P., "Experiments on Scattering of Monoenergetic Argon Beams by Heated Platinum", Ph.D. Thesis, Massachusetts Institute of Technology, 1967.

92. Coryell, J. W. and Raff, L. M., unpublished results.

93. Batzer, T. H. and Ryan, J. F., 1963 Vacuum Symposium Transactions, The Macmillan Company, New York, 1963, p. 166.

94. Coryell, J. W., "An Experimental Investigation of Gas-Solid Interaction Phenomena", Ph.D. Thesis, Oklahoma State University, 1972.

95. Moran, J. P., AIAA Journal, 8, 539 (1970).

96. Dike, P. H., Gray, W. T., and Schroyer, F. K., Technical Publication A1.4000, Leeds and Northrup Co., 1966.

97. DeVos, J. C., Physica, 20, 690 (1954).

98. Germer, L. H. and May, J. W., Surface Sci., 4, 452 (1966).

99. Hostettler, S. O. and Bernstein, R. B., Rev. Sci. Instr., 31, 872 (1960).

100. See for example: Gibbs, J. B., Transformer Principles and Practice, McGraw-Hill, New York, 1937.

101. Wellenstein, H. F. and Ensman, R. E., Rev. Sci. Instr., 44, 922 (1973).

102. Stern, R. M., Appl. Phys. Lett., 5, 218 (1964).

103. Bauer, E., Surface Sci., 7, 351 (1967).

104. Goodman, F. O., J. Chem. Phys., 64, 1051 (1976).

105. McClure, J. Doyle, J. Chem. Phys., 52, 2712 (1970).

106. Garibaldi, U., Levi, A. C., Spadacini, R., and Rommei, G. E., Surface Sci., 48, 649 (1975).

107. Stoll, G. A., Jr., Ehrhardt, J., and Merrill, R. P., J. Chem. Phys., 64, 34 (1976).

108. Cabera, N., Celli, V., Goodman, F. O., and Manson, R., Surface Sci., 19, 67 (1970).

109. White, R. E., Ehrhardt, J., and Merrill, R. P., J. Chem. Phys., 64, 41 (1976).

VITA[2]

Philip Steven Bush

Candidate for the Degree of

Doctor of Philosophy

Thesis: HELIUM, NEON, AND ARGON DIFFRACTION AND SCATTERING FROM A (3 x 5) R-35° W(110) CARBIDE SURFACE CHARACTERIZED BY LEED AND AUGER

Major Field: Chemistry

Biographical:

Personal Data: Born in New London, Connecticut, February 6, 1946, the son of William and Rhea Bush.

Education: Graduated from Williamsville Central High School, Williamsville, New York, in May, 1965; received Bachelor of Science degree with a major in Chemistry from The College of Emporia, Emporia, Kansas, in May, 1970; completed requirements for the Doctor of Philosophy degree at Oklahoma State University in December, 1977.

Professional Experience: Graduate Teaching Assistant, 1970-1971, 1974, 1977; Graduate Research Assistant, 1971-1977; Research Scientist, Chrysler Corporation, 1977.